



Silesian University of Technology  
Faculty of Materials Engineering

**DOCTORAL DISSERTATION**

**Effect of selected reactive elements on high temperature  
oxidation behavior of  $\gamma$ - $\gamma'$  Co-based superalloys**

**(Efekt wybranych pierwiastków reaktywnych na wysokotemperaturowe  
utlenianie nadstopów kobaltu typu  $\gamma$ - $\gamma'$ )**

Damian Migas

Supervisor: dr hab. inż. Grzegorz Moskał, prof. PŚ.

Assistant supervisor: dr inż. Agnieszka Tomaszewska

Katowice, 2023

## **Acknowledgements**

The author would like to thank Prof. Grzegorz Moskal for his supervision, encouragement, and support.

The author would also like to thank members of the Department of Materials Technologies of Silesian University of Technology for a cooperation and valuable comments. The research has been partially supported by the National Science Centre, Poland, grant no. 2018/29/N/ST8/02062, and by the Ministry of Education and Science, grant no. 0069/DIA/2018/47.

## Contributions related to this work

### Publications

D. Migas, P. Gradoń, T. Mikuszewski, G. Moskal, Crystallization behavior of ternary  $\gamma$ - $\gamma'$  Co-Al-W alloy, *Journal of Thermal Analysis and Calorimetry* 142 (2020), 1739-1747.

D. Migas, G. Moskal, H. Myalska, T. Mikuszewski, The effect of alloying elements on oxide scale spallation of multicomponent Co-based superalloys, *Corrosion Science*, 192 (2021), 109787.

D. Migas, T. Liptakova, G. Moskal, Effect of rare earth cerium addition on oxidation behavior of Co-Al-W alloys at 800°C, *Archives of Metallurgy and Materials*, 67 (2022), 203-208.

D. Migas, S. Roskosz, G. Moskal, T. Mikuszewski, P. Gradoń, Effect of Cooling Rate on Microstructure, Microporosity, and Segregation Behavior of Co-Al-W Alloys Prepared by Vacuum Induction Melting, *JOM*, 74 (2022), 2951-2963.

D. Migas, H. Myalska-Głowacka, B. Chmiela, T. Maciąg, T. Mikuszewski, G. Moskal, K. Matus, M. Godzierz, Microstructural characterization of cerium rich phases in new polycrystalline Co-Al-W-xCe superalloys, *Journal of Materials Research and Technology*, 20 (2022), 1665-1676.

D. Migas, B. Chmiela, H. Myalska-Głowacka, G. Moskal, K. Matus, R. Swadźba, The effect of yttrium on oxide scale growth on Co-Al-W-based superalloys, *Corrosion Science*, 208 (2022), 110674.

### Papers presented at international conferences

D. Migas, G. Moskal, Effect of rare earth elements on microstructure and oxidation resistance of  $\gamma$ - $\gamma'$  Co-based superalloys, *Junior Euromat 2022*, 19.-22.07.2022, Coimbra, Portugal

D. Migas, G. Moskal, The role of Y in high temperature oxidation behavior of Co-Ni-Al-W alloys, *Eurosuperalloys 2022*, 18.-22.09.2022, Bamberg, Germany

D. Migas, P. Gradoń, H. Myalska, B. Chmiela, T. Maciąg, T. Mikuszewski, Thermal analysis of intermetallic phases formed in Co-Al and Ni-Al based superalloys doped with Y, 6th Central and Eastern European Conference on Thermal Analysis and Calorimetry, 20-24.07.2021, Split, Croatia

D. Migas, G. Moskal, H. Myalska, T. Mikuszewski, Microstructure of polycrystalline  $\gamma'$  strengthened Co-based alloys doped with rare earth elements, *The XVIIth International Conference on Electron Microscopy*, 30.11-02.12.2020, Katowice, Poland.

## **Nomenclature**

RE – Reactive Elements

$k_p$  – parabolic rate constant

OOL – outer oxide layer

IOL – inner oxide layer

IPR – internal precipitation region

IOZ – internal oxidation zone

TEM – Transmission Electron Microscopy

SEM – Scanning Electron Microscopy

DSC – Differential Scanning Calorimetry

XRD – X-ray Diffraction

HAADF – High Angular Dark Field

FIB – Focused Ion Beam

LM – Light Microscopy

HRTEM – High Resolution TEM

Q – Energy of activation

VIM – Vacuum Induction Melting

BF – Bright Field

EDS – Energy Dispersive Spectrometry

EBSD – Electron Backscatter Diffraction

MAD – Mean Angular Deviation – the angular deviation between the observed and simulated lattice plane orientations

GB – grain boundary

fcc – face-centered cubic

hcp – hexagonal close packed

IOF – internal oxidation front

SOF – second oxidation front

# Table of Contents

<b>Abstract</b>	<b>7</b>
<b>Streszczenie</b>	<b>8</b>
<b>Introduction</b>	<b>9</b>
<b>2. Theoretical background</b>	<b>11</b>
2.1 Superalloys .....	11
2.1.1 Nickel-based superalloys.....	11
2.1.2 Conventional cobalt-based superalloys .....	12
2.1.3 New $\gamma$ - $\gamma'$ cobalt-based superalloys .....	14
2.2 Fundamentals of high temperature oxidation.....	18
2.2.1 Thermodynamics of oxidation .....	18
2.2.2 Oxidation kinetics and transport mechanisms.....	19
2.2.3. Oxide scale formation in multicomponent alloys .....	22
2.3 Oxidation of $\gamma$ - $\gamma'$ cobalt-based superalloys.....	24
2.4 Reactive elements effect.....	31
2.4.1 Reduction in scale growth rate .....	31
2.4.2 Improvement of scale adherence.....	33
2.4.3 Reactive elements in cobalt-based alloys.....	34
2.5 Summary .....	37
<b>3. Experimental</b>	<b>38</b>
3.1 Selection of materials and research programme.....	38
3.2 Alloys processing .....	39
3.3 High temperature oxidation.....	41
3.3.1 Isothermal oxidation tests.....	41
3.3.2 Cyclic oxidation tests .....	41
3.4 Characterization techniques .....	42
3.4.1 Scanning Electron Microscopy (SEM) .....	42
3.4.2. Scanning Transmission Electron Microscopy (STEM).....	42
3.4.3. Differential Scanning Calorimetry (DSC).....	42
3.4.4. Light Microscopy (LM) .....	42
3.4.5 Hardness .....	42

3.4.6 X-ray diffraction (XRD).....	43
3.4.7 Analysis of chemical composition .....	43
3.5. Preparation of samples .....	44
3.6 CALPHAD modelling.....	45
<b>4. Results</b>	<b>46</b>
4.1 Microstructural and thermal analysis of alloys .....	46
4.1.1. Characterization of as-cast microstructure .....	46
4.1.2. Characterization of as-aged microstructure.....	50
4.1.3 Thermal analysis .....	53
4.3 High temperature isothermal oxidation behavior of alloys .....	59
4.4 High temperature cyclic oxidation behavior of alloys .....	65
4.5 Microstructural characterization of oxide scales.....	69
<b>5. Discussion</b>	<b>84</b>
5.1 Microstructure and thermal analysis of alloys .....	84
5.2 High temperature oxidation behavior of alloys .....	90
5.3 The obtained results in view of the current state of the art .....	99
<b>6. Summary and outlook</b>	<b>101</b>
<b>7. Conclusions</b>	<b>102</b>
<b>References</b>	<b>104</b>

## Abstract

The new  $\gamma$ - $\gamma'$  cobalt-based alloys are an attempt to address the limitations of commercially used nickel alloys, which no longer allow for an increase in the maximum operating temperature of gas turbines in the aircraft and power industries. The new group of alloys attracts the attention of an increasing number of scientists worldwide and is still in the research phase. Despite numerous advantages, these new materials exhibit low resistance to high temperature oxidation. One approach to improve this property is the introduction of reactive elements (RE) into the alloys, which was the subject of the research presented in the thesis.

The experimental work included the manufacturing of the Co-9Al-9W (at%) alloy and four RE-modified alloys with a composition of Co-9Al-9W-0.1RE (RE=La, Nd, Dy, Y). The microstructure, thermal properties, and resistance to high temperature oxidation under isothermal and cyclic conditions were investigated for these alloys. The oxidation mechanism of all the alloys was studied, and the oxidation kinetics were determined at 700, 800, and 900 °C. The oxidized layers were also characterized in detail by means of electron microscopy. Special attention was given to the modifications in the microstructure and the oxidation mechanism resulting from the presence of RE.

The results showed that the introduction of small amounts of RE has a significant impact on the microstructure and properties of new Co-based alloys. The increase of both isothermal and cyclic oxidation resistance was achieved, particularly at 900 °C. However, the improvement was not efficient due to the lack of formation of a protective  $\text{Al}_2\text{O}_3$  layer. The RE such as La, Nd, Dy, and Y exhibit very low solubility in both  $\gamma$ -Co<sub>ss</sub> and  $\gamma'$ -Co<sub>3</sub>(Al, W) phases, but form intermetallic phases, primarily at grain boundaries. These phases undergo selective internal oxidation. During the oxidation process, it was observed that the RE-modified alloys develop substantially thicker internal oxidation zones compared to that of the reference alloy. In addition, the increased concentration of Al-rich oxides can be observed near the scale-substrate interface. Such phenomenon is likely associated with a reduced oxidation rate and a thinner oxide scale in the modified alloys. Numerous RE-rich oxides located at or near the substrate-oxide boundary may contribute to the improved oxide scale adherence, as reflected in the enhanced cyclic oxidation resistance.

## Streszczenie

Nowe nadstopy typu  $\gamma$ - $\gamma'$  na bazie kobaltu są próbą odpowiedzi na ograniczenia komercyjnie stosowanych nadstopów niklu, które nie dają już możliwości zwiększania maksymalnej temperatury pracy turbin gazowych w przemyśle lotniczym oraz w energetyce. Nowa grupa nadstopów wykazuje pewne korzyści względem obecnie stosowanych nadstopów niklu, dlatego przyciąga uwagę coraz większej liczby naukowców na całym świecie i jest wciąż w fazie badań. Pomimo licznych zalet, nowe materiały wykazują niską odporność na wysokotemperaturowe utlenianie. Jednym ze sposobów jej poprawy jest dodawanie do stopów pierwiastków reaktywnych, co było przedmiotem prac zawartych w rozprawie.

Prace eksperymentalne objęły wytworzenie stopu Co-9Al-9W (at%) oraz czterech stopów modyfikowanych pierwiastkami reaktywnymi (RE) o składzie Co-9Al-9W-0.1RE (RE=La, Nd, Dy, Y). Przebadano mikrostrukturę wytworzonych stopów, ich właściwości termiczne oraz odporność materiałów na utlenianie wysokotemperaturowe w warunkach izotermicznych oraz cyklicznych. Zbadano mechanizm utleniania wszystkich stopów oraz wyznaczono kinetykę utleniania w 700, 800 oraz 900 °C. Dokonano szczegółowej charakteryzacji warstw utlenionych metodami mikroskopii elektronowej. Szczególną uwagę poświęcono zmianom w mikrostrukturze oraz mechanizmie utleniania związanym z obecnością pierwiastków reaktywnych.

Wykazano, iż wprowadzenie pierwiastków reaktywnych przyczynia się do poprawy odporności na utlenianie izotermiczne stopów Co-Al-W, zwłaszcza w 900 °C. Mimo obniżenia prędkości utleniania, poprawa jest niewystarczająca ze względu na brak tworzenia się ochronnej warstwy Al<sub>2</sub>O<sub>3</sub>. Pierwiastki takie jak La, Nd, Dy oraz Y praktycznie nie rozpuszczają się w roztworze  $\gamma$ -Co ani w fazie  $\gamma'$ -Co<sub>3</sub>(Al, W). Tworzą natomiast fazy międzymetaliczne, głównie na granicach ziarn. Fazy te ulegają selektywnemu, wewnętrznemu utlenianiu. W trakcie utleniania, stopy domieszkowane pierwiastkami reaktywnymi charakteryzują się dużo szerszą strefą utleniania wewnętrznego w stosunku do materiału referencyjnego, a w pobliżu granicy metal-zgorzelina obserwuje się zwiększoną koncentrację tlenków bogatych w glin. Może to przekładać się na niższą prędkość utleniania i grubość warstw tlenkowych w modyfikowanych stopach. Liczne tlenki zawierające pierwiastki reaktywne, lokujące się przy granicy podłoże-zgorzelina, mogą mieć wpływ na wzrost przyczepności zgorzeliny, objawiający się wzrostem odporności na utlenianie cykliczne.

## Introduction

The improvement of heat-resistant superalloys is crucial for the aircraft and power industries. Enhancing the service temperature of gas turbines is of great significance as it directly influences their efficiency and, therefore, cost, and environmental impact. The efficiency increases due to the development of materials providing high temperature thermal stability of turbine components. Ni-based superalloys have been the primary materials utilized in such applications owing to their capacity to operate at 90% of their melting temperature and their ability to endure high mechanical stresses under corrosive environments. The unique properties of Ni-based superalloys arise from the formation of a  $\gamma$ - $\gamma'$  microstructure that contain cuboidal  $L1_2$  precipitates in a face-centred cubic (fcc) matrix. The further development is hampered by the limitations that Ni-base superalloys face, primarily related to temperature capability.

Recently, it has been discovered that Co-based alloys can be designed to possess the same  $\gamma$ - $\gamma'$  microstructure as the commonly used Ni-based superalloys. The discovery marks a new era in the development of high-temperature alloys. The introduction of these alloys offers several potential benefits, including higher temperature capability, positive lattice misfit, and the ability to produce large single crystals without solidification defects on their surface (known as freckles). Although the mechanical properties of the new Co-based superalloys are currently inferior to those of the latest generations of single-crystal Ni-based alloys, efforts are underway to optimize these alloys. The advantage of commercially used Ni-based alloys over new Co-based alloys lies in their lower cost and extensive research and optimization conducted over decades. Therefore, a better understanding of the effect of alloying elements on the properties of newly developed alloys is desirable. Particularly, further knowledge is needed in the area of high temperature oxidation resistance, which represents a critical weakness.

The thesis focuses on examination of ternary Co-Al-W alloys, which are susceptible to high temperature oxidation above 700 °C. These alloys do not form a continuous alumina layer that provides a barrier against oxidation. Various alloying strategies, including the addition of Cr, B, Si, or Ni, have been successfully employed to enhance the oxidation resistance of Co-Al-W-based alloys. Literature data reveal an additional method to enhance the oxidation resistance of an alloy, which involves adding reactive elements (RE). However, the complete data on this effect on oxidation behavior of the new  $\gamma$ - $\gamma'$  Co-based superalloys is missing.

The RE addition may exhibit a beneficial effect on the oxidation behavior of superalloys, particularly alumina- or chromia-formers. Although Co-Al-W-based alloys do not belong to these groups, it was possible to achieve a continuous inner layer of  $\text{Al}_2\text{O}_3$  after oxidation at 800 °C by incorporating a small amount of boron (0.12 at%) to the alloys. Therefore, the attempt of introduction of RE to Co-based superalloys is worth considering. The study was motivated by the potential positive impact of doping with RE on the oxidation resistance of new Co-based alloys and the limited availability of literature data regarding the RE effect on these alloys.

The goal of the present PhD study was to systematically investigate the effect of various reactive elements (La, Nd, Dy, Y) on microstructure and properties of new Co-Al-W-based superalloys, with a particular focus on their high temperature oxidation behavior. Special attention was given to evaluating the isothermal and cyclic oxidation resistance of the alloys at 700-900 °C, as well as analyzing the microstructure of the oxide scale.

For this purpose, different minor alloying elements (La, Nd, Dy, Y) were added to the Co-Al-W ternary alloy in an approximate amount of 0.1 at%. Such additions have been known to enhance the high temperature oxidation resistance of various Ni- and Fe-based superalloys. Several analytical methods, including scanning electron microscopy (SEM), transmission electron microscopy (TEM), energy-dispersive X-ray spectroscopy (EDS), light microscopy (LM), differential scanning calorimetry (DSC), and X-ray diffraction (XRD), were employed to characterize the oxidation process, thermal properties, microstructure of the alloys, and oxide layers. The analysis of the results was also supported by the CALPHAD method.

The mechanisms of interaction between RE and microstructure formation, as well as the formation of oxide scales in new Co-based alloys, were determined. Predictions were also made regarding the development of these properties upon the introduction of RE into other types of Co-based alloys. The comprehensive analysis of the effect of RE on new Co-based alloys serves as a guide for further research on these materials, with a specific focus on RE-doping.

## **2. Theoretical background**

### **2.1 Superalloys**

Superalloys have played a central role in the development of jet engine technology. The term “superalloys” does not have a precise definition, although they are typically alloys composed of Fe, Ni or Co, and are commonly used for applications that involve high temperatures. In the work “Superalloys II”, Sims offered a definition that describes superalloys as alloys intended for use in high temperature environments, typically comprised of group VIIIA elements, withstanding considerable mechanical stress, and requiring a high degree of surface stability [1]. Since the advent of jet-powered civil aviation and rocketry in the 1950s, superalloys have been instrumental in the development of high thrust engines. This is because many materials are unable to withstand the extreme conditions in the hottest sections of engines, where temperatures can reach around 1300 °C. In contrast, superalloys possess a range of properties that make them ideal for use in jet engines, including high strength, resistance to fatigue and fracture, creep resistance, and stress-rupture resistance at high temperatures. Additionally, superalloys are highly resistant to corrosion and oxidation under these conditions [2].

Superalloys are able to withstand high temperatures and remain stable due to the combination of their face-centered cubic (fcc) structure and strengthening phases. They are capable of operating successfully at temperatures greater than 0.6 times their melting point [3]. Ni is able to retain its fcc structure from room temperature up to its melting point of 1455 °C. On the other hand, Co and Fe undergo phase transformations at temperatures below their melting points. Specifically, Co transforms from hexagonal closed packed (hcp) to fcc at 417 °C, and Fe transforms from body-centered cubic (bcc) to fcc at 912 °C. To stabilize Co and Fe in the fcc structure over the temperature range of a gas turbine engine, they must be alloyed, typically with Ni [4].

#### **2.1.1 Nickel-based superalloys**

Overall, Ni-based superalloys are the first choice for applications that require exceptional mechanical properties at elevated temperatures. Their unique combination of strength, ductility, and corrosion resistance makes them essential materials dedicated to high performance industries. They are widely used in aerospace, power generation, and chemical processing industries, where materials capable of withstanding extreme environments are required. There are several types of Ni-based superalloys, such as wrought alloys, cast alloys,

and powder metallurgy alloys [3-5]. All Ni-based superalloys possess an austenitic fcc matrix ( $\gamma$ ) that is strengthened through solid-solution strengthening, achieved by adding certain elements. In polycrystalline superalloys, additional strengthening is achieved through the precipitation of carbides, primarily at grain boundaries. Some Ni-based superalloys also contain coherent or semi-coherent intermetallic phases known as gamma prime ( $\gamma'$ ) and gamma double prime ( $\gamma''$ ) that contribute to their strength [2-5]. Precipitation strengthening is considered to be the most efficient form of strengthening in Ni-based superalloys at elevated temperatures. In such alloys, the  $\gamma'$  phase is typically present as coherently embedded precipitates within the disordered  $\gamma$  matrix phase. It has an ordered intermetallic  $L1_2$  structure [6] (Al atoms at the cube corners and Ni atoms at the centre of each face) with a nominal stoichiometry of  $Ni_3Al$  (Figure 2.1).

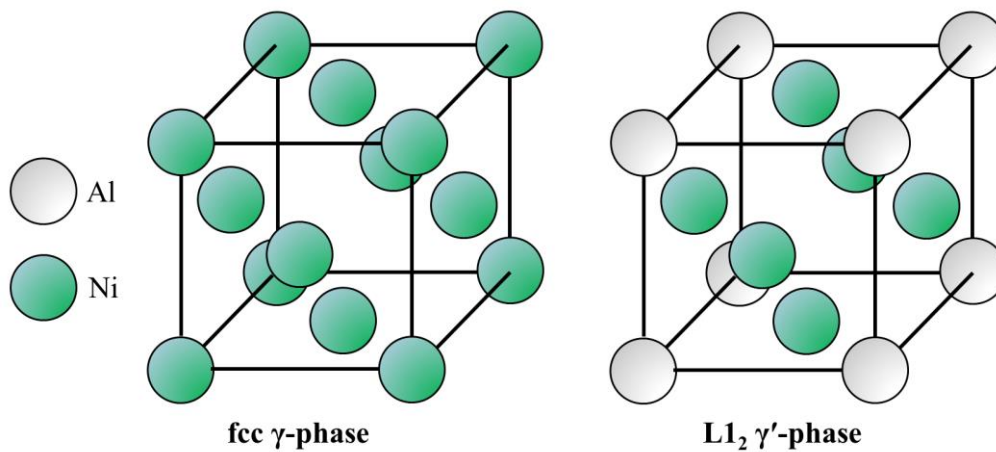


Figure 2.1: The crystal structures of disordered  $\gamma$  phase and ordered  $\gamma'$  phase.

The mechanical performance of the  $\gamma$ - $\gamma'$  superalloys at elevated temperatures is exceptional owing to strengthening by  $L1_2$  phases. Unlike in most alloy systems, the  $\gamma'$ -strengthened Ni-based superalloys exhibit a remarkable feature: their yield stress which is defined as the stress required for dislocation glide-induced plastic deformation, tends to either remain stable or increase slightly with increasing temperature up to approximately 800 °C, before declining sharply. The phenomenon is known as “yield-stress anomaly” and is typically caused by the self-locking mechanisms of individual superdislocations, often through the formation of Kear-Wilsdorf locks [6, 7].

### 2.1.2 Conventional cobalt-based superalloys

Age-hardenable Ni-based alloys are strengthened by the presence of the  $\gamma'$  intermetallic phase  $Ni_3(Al, Ti)$ , while the non-hardenable Ni-, Co-, and Fe-based alloys are strengthened by solid-solution strengthening of the fcc ( $\gamma$ ) matrix. Some precipitation strengthening from

carbides may occur in Co-based superalloys; however, they lack the intermetallic phase strengthening equivalent to the  $\gamma'$  strengthening observed in Ni-based alloys. These Co-based alloys exhibit superiority over Ni-based superalloys in various aspects, particularly in terms of higher thermal fatigue resistance and improved corrosion characteristics in environments rich in sulfur compounds [8-10].

Haynes (1905) patented Stellite, which is widely regarded as the first Co-based alloy [11]. During the early 1940s, researchers actively explored the Co-Cr-Mo system, which was found to possess exceptional corrosion resistance along with its good wear properties. This alloy system, commercially known as Vitallium, was used as dental material due to its biocompatibility [12]. The alloy was subsequently modified for specific high temperature applications, resulting in the development of the HA-21 alloy (Haynes Stellite Alloy no. 21) [13]. Over time, numerous other alloys were developed using the same strategy, such as the AiResist series, Haynes series, MAR-M series, and Stellite series, among others. These alloys relied on the solid solution strengthening achieved through the addition of refractory metals [9, 13].

During the aging process of these alloys at intermediate temperatures (between 650 °C and 1000 °C), carbides with the stoichiometries  $M_6C$ ,  $M_{23}C_6$ , and  $M_7C_3$  (where M stands for metal) precipitate and contribute to the increase of their high temperature strength [14]. The most widely used alloys for high temperature applications are Haynes 25, Haynes 188, and MAR-M-509, with yield strength values of up to 400 MPa at 540 °C [15]. Co-based alloys are employed in high temperature applications where the stress levels are comparatively low, such as in the static parts of gas turbine engines, for example, turbine engine buckets, nozzle guide vanes, and similar components. Despite their creep properties, Co-based alloys have not gained widespread usage due to lower strength when compared to Ni-based alloys [15, 16].

It would be possible to overcome the limitations of conventional Co-based superalloys through precipitation hardening with coherent intermetallic phases. Hence, significant efforts were made during the 1960-1970s to identify Co-based systems that could be potentially strengthened with  $\gamma'$  phases. Previous reports indicated the existence of metastable  $L1_2$  ordering in binary Co-X alloys with the stoichiometry  $Co_3X$  (where X = Ti, Al, Nb, Ta, W), but these phases do not remain stable at high temperatures exceeding 600 °C [17-21]. Co-Nb, Co-Ta, and Co-W binary alloys exhibit metastable  $L1_2$  ordering of  $Co_3Nb$ ,  $Co_3Ta$ , and  $Co_3W$ , respectively, along with hcp martensite plates in an fcc-Co matrix at the early stages of heat treatment. However, they subsequently transform to equilibrium structures [17, 22, 23]. In the Co-Ti system,  $Co_3Ti$  with an  $L1_2$  ordered structure is observed. Nonetheless, these

precipitates have a large lattice misfit, leading to decreased thermal stability at high temperatures. The  $\text{Co}_3\text{Al}$  phase is not stable in the Co-Al system, but its stability can potentially be obtained through the addition of other elements. In 1971, Lee studied the hardening behavior of the Co-Al-X ternary alloys (where X=W, Ta, Nb, Mo, Ti) and found an ordered fcc superlattice, or coherent precipitate in Co-Al-W system [18]. The continuous increase in hardness was observed for aging times up to 1000 h at 800°C due to the precipitation of this phase. Afterwards, it took 35 years for another significant discovery to be made in the area of  $L1_2$  phases in Co-based superalloys.

### 2.1.3 New $\gamma$ - $\gamma'$ cobalt-based superalloys

Sato et al. (2006) discovered  $\gamma'$ - $\text{Co}_3(\text{Al}, \text{W})$ , a ternary compound with an  $L1_2$  structure that precipitates in  $\gamma$ -matrix in Co-Al-W system [16]. The discovery began a new era in high temperature alloy development history. The  $\gamma'$ -strengthened Co-based alloys have demonstrated higher high temperature strength than conventional Co-based alloys [16, 24, 25]. The cuboidal precipitates of the  $\gamma'$ - $\text{Co}_3(\text{Al}, \text{W})$  phase coherently precipitate in the solid-solution  $\gamma$ -Co (fcc) matrix, as shown in Figure 2.2. This is due to the relatively small lattice misfit between the two phases, resulting in a two-phase microstructure of  $\gamma + \gamma'$ . Microstructures of Co-base alloys strengthened by  $\gamma'$  phase are similar to those of Ni-base superalloys, which are strengthened by  $\gamma'$ - $\text{Ni}_3\text{Al}$  precipitates.

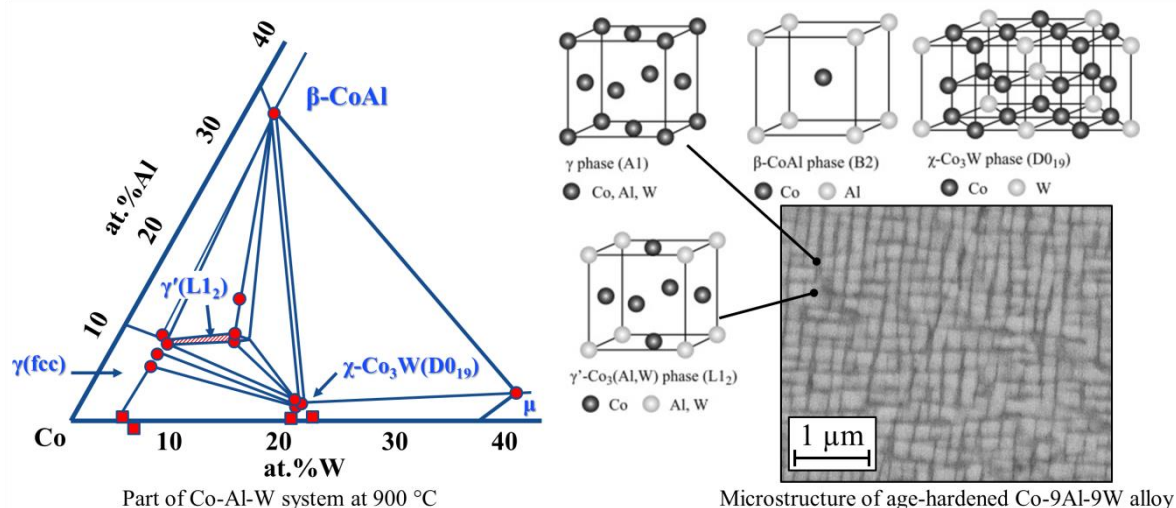


Figure 2.2: Schematic of the Co-rich corner of Co-Al-W ternary phase diagram at 1173 K with a representation of the unit cells for the  $\gamma$ ,  $\gamma'$ ,  $\beta$ , and  $\chi$  phases in the Co-Al-W system. The SEM micrograph shows the  $\gamma$ - $\gamma'$  microstructure. The schematic adapted from [26].

Unlike  $\text{Ni}_3\text{Al}$ ,  $\gamma'$ - $\text{Co}_3(\text{Al}, \text{W})$  is not an equilibrium phase. At 900 °C, there is a narrow phase field region of  $\gamma$ - $\gamma'$  in the Co-Al-W ternary section. However, prolonged aging at this temperature may result in the transformation of the  $\gamma$ - $\gamma'$  microstructure to the equilibrium

phases of  $\gamma$ -Co,  $\beta$ -CoAl, and  $\chi$ -Co<sub>3</sub>W [27-29]. The addition of different alloying elements, such as Ti and Ta, stabilizes the L1<sub>2</sub>-Co<sub>3</sub>(Al, W) phase [30, 31].

Since the new Co-based alloys are considered as alternative for Ni-based superalloys, it is worth discussing the fundamental differences between Ni-based alloys and Co-based alloys that are strengthened by L1<sub>2</sub> phases.

### Lattice misfit

The lattice misfit is one of the key parameters when designing superalloys [32]. The lattice misfit  $\delta$  is defined as:

$$\delta = \frac{2(a_{\gamma'} - a_{\gamma})}{a_{\gamma'} + a_{\gamma}} \quad (2.1)$$

where  $a_{\gamma}$  and  $a_{\gamma'}$  are the lattice parameters of  $\gamma$  and  $\gamma'$ , respectively.

The small lattice misfit is necessary to minimize the interfacial energy between  $\gamma$  and  $\gamma'$  and to slow down the coarsening of the  $\gamma'$  precipitates. The shape of the  $\gamma'$  precipitates is affected by the lattice misfit. Cuboidal precipitates with sharp corners are formed when the lattice misfit is  $\delta < 0.5\%$ , whereas spherical precipitates are formed when the misfit is  $\delta > 0.5\%$  [33]. The lattice parameters of  $\gamma$  and  $\gamma'$  are also influenced by temperature, along with the added elements, but to different extents. As temperature rises,  $\gamma'$  expands less than  $\gamma$ , causing the misfit to become “more negative” [32]. This phenomenon is commonly observed in Ni-based alloys that typically have a negative lattice misfit. However, new Co-based superalloys exhibit a positive lattice misfit. Mughrabi suggested that superalloys with a positive instead of a negative misfit parameter could provide better high temperature strength than otherwise similar alloys with a negative lattice mismatch [34]. Furthermore, difference in lattice misfit may result in P-type rafting in Co-based superalloys while N-type rafting in Ni-based superalloys under tension stress [35].

### Melting point

The upper limit of  $\gamma'$ -solvus temperatures in Ni-base superalloys is approaching their melting temperatures, while  $\gamma'$ -strengthened Co-base alloys have a higher upper limit. The melting temperatures of Co-base alloys are greater than those of Ni-base superalloys by 50-150 °C [36]. This difference is due to the inherent higher melting temperature of pure Co compared to that of pure Ni. The solidus and liquidus temperatures are significant but should not be the only criteria considered when evaluating superalloys. The  $\gamma'$  solvus is important factor that also need to be taken into account. The new Co-based superalloys possess a relatively small freezing range between the liquidus and solidus temperatures, which is advantageous in producing large-diameter ingots with minimal segregation [36, 37].

Additionally, their large temperature range between the solidus and  $\gamma'$ -solvus temperatures is beneficial for hot working processes (Figure 2.3). The increase of both the  $\gamma'$ -solvus and  $\gamma'$ -fraction may be achieved by alloying. Nowadays, there are Co-based alloys characterized by  $\gamma'$ -solvus exceeding 1200 °C and  $\gamma'$ -fraction over 70% [38, 39].

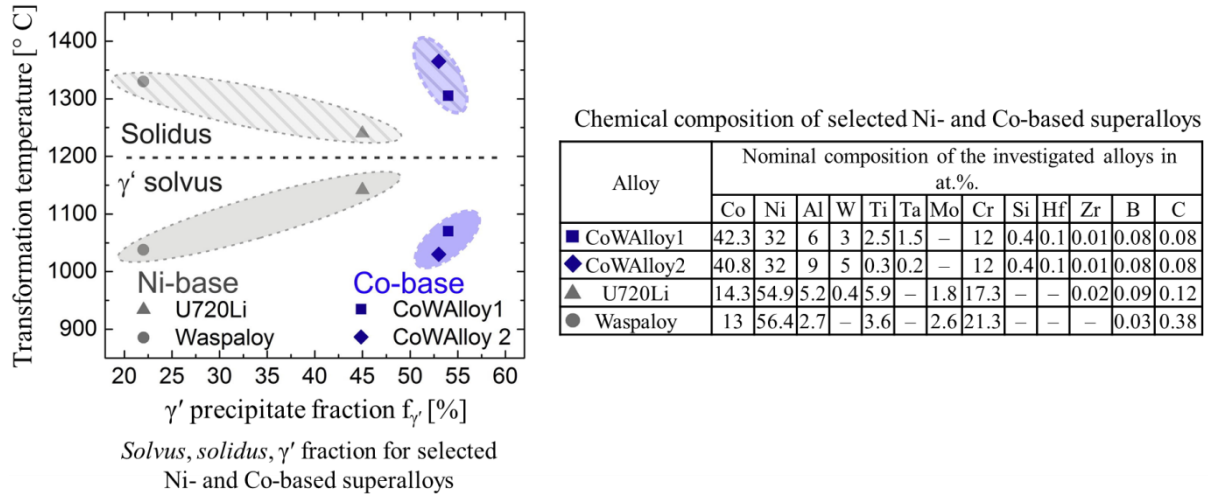


Figure 2.3: Advantages of Co-base superalloys compared to Ni-base superalloys: large processing window together with a high  $\gamma'$  fraction. Adapted from [40].

### Single-crystal solidification

New Co-based alloys exhibit favorable solute partitioning during solidification, which is in contrast to Ni-base single crystals. High levels of Re and W in Ni-base alloys can cause convective instabilities during solidification [41, 42], resulting in formation of freckle defects. These defects are small chains of equiaxed grains formed by the fragmentation of dendrite arms during solidification. Therefore, Co-based superalloys may be more attractive for use in large, complex single-crystal or directionally solidified castings, where the formation of misoriented grains and freckling are significant challenges. Initial studies demonstrated that Co superalloys can be processed into large single crystals without forming solidification defects on their surface [36], which is a major issue in Ni-based superalloys.

### Mechanical properties

The new Co-based alloys exhibit a superior resistance to creep when compared to conventional Co-based superalloys, like MAR-M-509 [43]. Moreover, Co-Al-W-based single-crystal superalloys alloyed with Ti and Ta may exhibit better resistance to creep compared to first-generation Ni-based single crystal superalloys (Figure 2.4a). Although there is a potential to improve the creep properties to match those of the fourth-generation Ni-based single crystal superalloys, it can be observed that Co-Al-W-based superalloys possess comparable or even superior creep properties when compared to certain commercially available Ni-based

superalloys, despite containing only a few alloying elements [44]. For novel Co-based alloys, there is still a room to optimize mechanical properties and solvus temperature. Figure 2.4b shows that the multicomponent Co-based alloy may demonstrate a flow stress-temperature relationship similar to that of MAR-M-247. Additionally, it may exhibit a higher flow stress at elevated temperatures when compared to both the Co-Al-W-Ta and Haynes 188 [45] alloys.

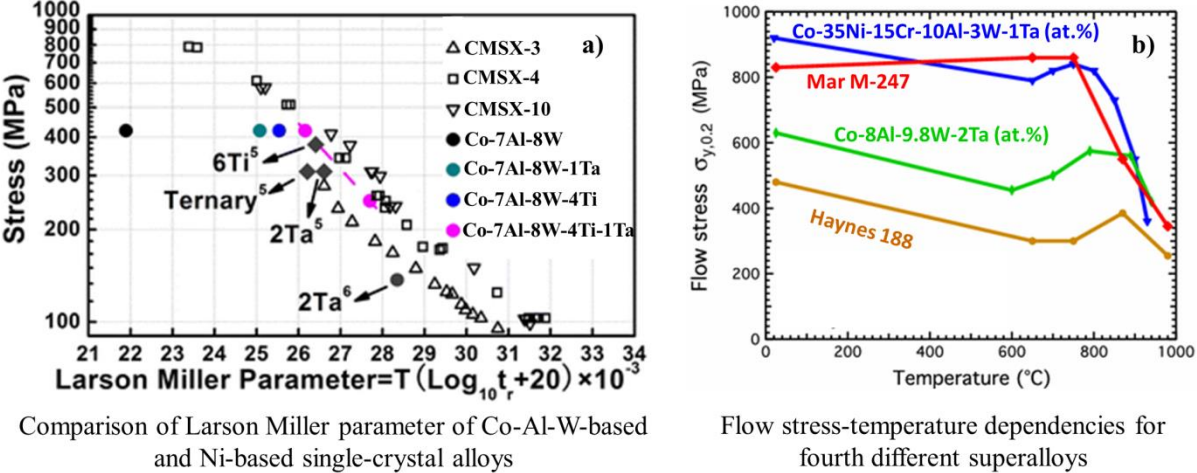


Figure 2.4: Larson-Miller parameters of Co-Al-W-based and Ni-based single-crystal alloys (a); Flow stress behavior with temperature, measured using isothermal compression testing for different Co- and Ni-based superalloys (b). The figures adapted from [44, 45].

The structured knowledge on the  $\gamma$ - $\gamma'$  Co-based superalloys can be found in the four review papers [15, 43, 46, 47]. Co-based alloys can be processed to have a  $\gamma$ - $\gamma'$  microstructure that resembles the microstructure of commonly used Ni superalloys. In addition, Co-based alternatives may have certain advantages over Ni-based alloys. However, further research is required before these alloys can be implemented in the power or aircraft industries. One of the major challenges associated with newly developed alloys is their resistance to high temperature oxidation, which is an important aspect to be addressed in this thesis. Therefore, additional paragraphs in the literature review will be dedicated to this issue.

## 2.2 Fundamentals of high temperature oxidation

### 2.2.1 Thermodynamics of oxidation

Taking into consideration the use of superalloys in hot section of gas turbines, high temperature oxidation should be considered as material degradation process. Therefore, understanding of the oxidation theory is important for analysis of superalloys in view of their high temperature oxidation resistance.

The basic criterion allowing to evaluate whether, under given conditions, the oxidation process of a specific metal can occur at all, is the sign of the free energy change of the reaction,  $\Delta G$  [48]. Only when  $\Delta G$  from the reactants to products is negative, the reaction occurs spontaneously. In the simplest case of the oxidation of a pure metal M, this process can be expressed by an equation:



The equilibrium oxygen partial pressure  $p(O_2)$  required for the coexistence of the oxide and metal can be expressed as follows:

$$p(O_2) = e^{\left(\frac{\Delta G_0}{RT}\right)} \quad (2.3)$$

where  $\Delta G_0$  is the standard Gibbs free energy, T is the absolute temperature [K], and R is the molar gas constant ( $8.3144 \text{ Jmol}^{-1}\text{K}^{-1}$ ). The equilibrium oxygen partial pressure influenced by temperature and type of the oxide is known as the dissociation pressure of the oxide. At a specific temperature T, if the partial pressure of oxygen is lower than the dissociation pressure of the oxide, formation of the oxide becomes thermodynamically unfavorable [49].

The  $\Delta G_0$  at a given temperature and  $p(O_2)$  may be determined using the standard enthalpy of reaction  $\Delta H$  as well as the standard entropy change  $\Delta S$  [50].

$$\Delta G = \Delta H - T\Delta S \quad (2.4)$$

The dissociation pressure of an oxide and its standard Gibbs free energy ( $\Delta G_0$ ) for formation at a specific temperature can be found in the Ellingham-Richardson diagram [51], which is shown in Figure 2.5. It is important to note that the Ellingham-Richardson diagram only provides thermodynamic parameters and does not offer any information about reaction kinetics. The oxidation kinetics are another crucial factor that needs to be addressed.

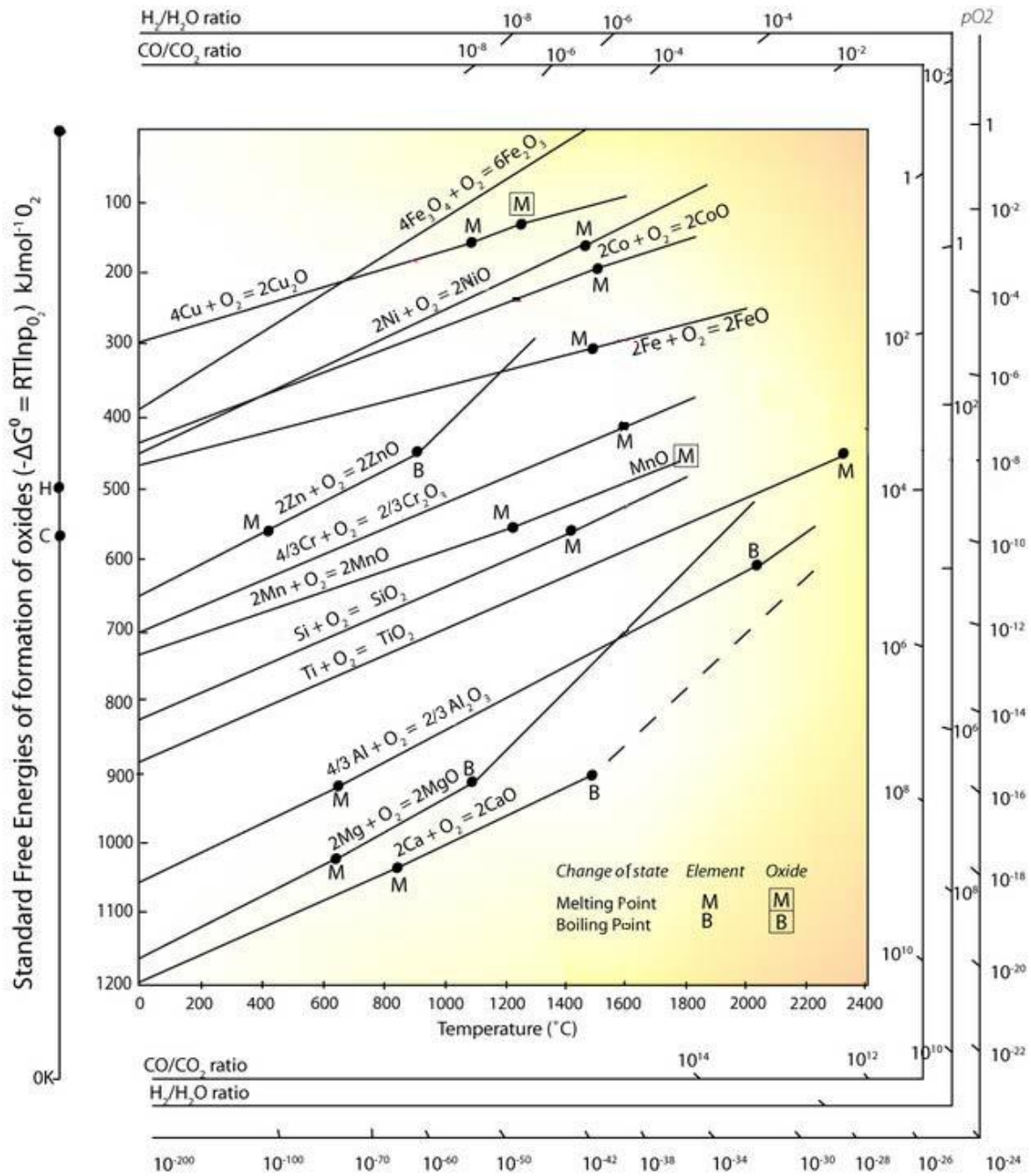


Figure 2.5: Ellingham-diagram for the formation of oxides based on their standard free energy of formation over temperature. From [52].

## 2.2.2 Oxidation kinetics and transport mechanisms

Although thermodynamics can provide information on whether a reaction is thermodynamically favorable, knowledge of the reaction rate is also necessary to assess its practical viability. Measuring the kinetics of oxidation is a fundamental method for evaluating the behavior of alloys under high temperature conditions. Research by Tammann [53] and Pilling and Bedworth [54] established that the formation of a dense layer on a metal surface can be modeled using the parabolic rate law, a basic kinetic equation. The parabolic rate law

is applicable to the corrosion process for both pure metals and alloys over a wide temperature range, which is supported by numerous studies [55]. Tammann's empirical equation can be used to describe the kinetics of oxidation for metals and alloys:

$$x = 2k'_p t + C' \quad (2.5)$$

where  $x$  is the scale thickness [cm] after a time  $t$  [s],  $k'_p$  is the parabolic rate constant measured in  $\text{cm}^2\text{s}^{-1}$ , while  $C'$  is a constant.

In order to determine the parabolic rate constant  $k'$  from equation (2.5), it is necessary to measure the thickness of the scale at various time intervals during the oxidation process. However, this procedure can be time-consuming. Alternatively, they can be calculated from values of  $k''_p$ , which can be obtained more accurately through gravimetric measurements using Pilling and Bedworth's equation [54]:

$$\left(\frac{\Delta m}{A}\right)^2 = k''_p + C \quad (2.6)$$

where  $\Delta m$  is a weight gain [g] after a time  $t$  [s],  $A$  is the surface area of metal [ $\text{cm}^2$ ],  $k''_p$  denotes the parabolic rate constant in  $\text{g}^2\text{cm}^{-4}\text{s}^{-1}$ , and  $C$  is a constant. It is important to note that such method may not yield accurate results if volatilization occurs.

The oxidation process may undergo kinetics law other than parabolic, including: linear, cubic, logarithmic or inverse logarithmic laws [56]. The oxidation kinetics of an alloy are closely related to the transport mechanisms through the oxide scales that form on its surface during oxidation. According to the Tammann's mechanism of formation of a dense single-layer scale [53], there is a constant difference in the concentration of the allowed oxidant in the growing scale, which enables the inward diffusion of this reagent. Pfeil's research [57] showed that the marker (a particle which does not participate in the oxidation process) was always located inside the scale, near the substrate. This behavior indicates that the oxidation is a result of outward metal diffusion. These findings provided an experimental basis for Wagner's theory of metal oxidation [56], which was developed and extended to two-component alloys in further decades. At high temperatures, oxidation rate is limited by solid-state diffusion through the scale, causing a decrease in reaction rate as oxide thickness increases. Lattice diffusion of reacting atoms, ions, or electrons is assumed to be the rate-determining factor, with short-circuit diffusion not contributing to the process. This occurs due to point defects, with migrating species being lattice and electronic defects such as vacancies, interstitial ions, electrons, and electron holes. The growth process of the oxide scale can occur either by metal or oxidant diffusion or through two-way diffusion of both reagents. The involvement of each reagent's diffusion in the overall transport process through

the oxide scale depends on the type of crystal lattice defects present in the oxidation product. If the cation sublattice of the oxidation product is predominantly disordered, the growth of the oxide scale can occur only by outward diffusion of the metal (Figure 2.6a). In the case of the oxides  $M_{1-y}O$  (e.g. CoO), diffusion of metal (Co) takes place by movement of ions and electrons through vacancies and electron holes [58]. In the case of the oxides  $M_{1+y}O$  (e.g. ZnO), the diffusion may be through interstitial spaces [59]. Alternatively, the oxide scale growth occur via inward diffusion of the metal (Figure 2.6b) in the case of disordered anion sublattice of the oxidation products [55]. The example of such inward transport is yttrium [60], whose oxidation proceeds primarily by the diffusion of oxygen through the oxide layer.

Point defects may not only determine the oxidation mechanism of a metal but also its kinetics. A high concentration of defects may facilitate ion transfer and thus increase the oxidation rate. This can be observed in the case of Co, which has higher oxidation rates than Ni, since the cation sublattice of CoO is more disordered than that of NiO [55, 61]. Moreover, the oxidation rate through an oxide may be increased or decreased by impurities in alloys, according to the Hauffe–Wagner theory of doping [62]. The classical explanation of the doping effect can only be applied when the concentration of defects is extremely low and the scale is growing primarily through volume diffusion. It can be inferred that the type of the oxide scale plays a crucial role in determining oxidation resistance of a metal. Hence, it is important to investigate the types of oxides that may form during the high temperature oxidation of multicomponent alloys, such as superalloys.

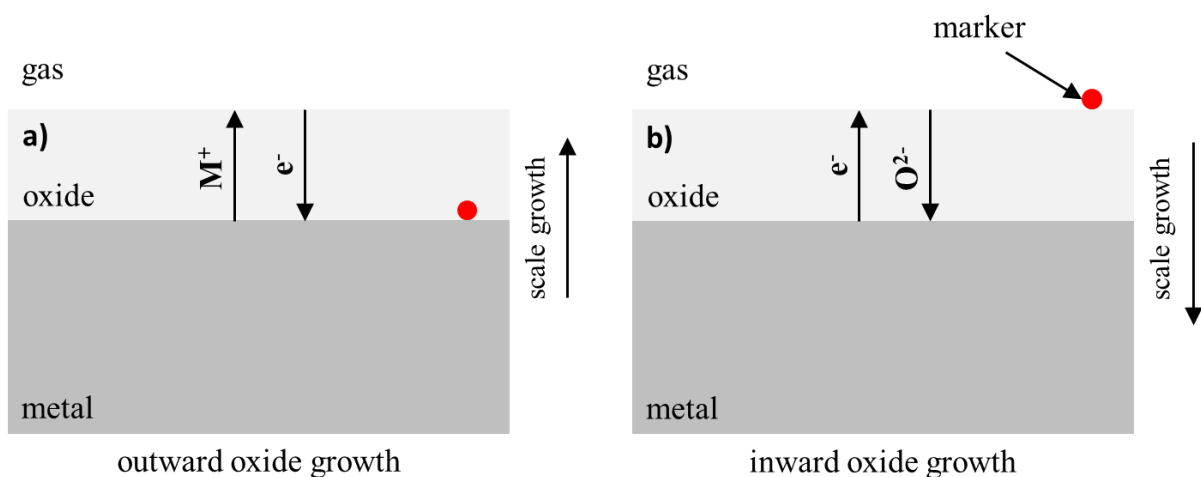


Figure 2.6: Schematic of outward (a) and inward (b) diffusion in a metal during oxidation.

### 2.2.3. Oxide scale formation in multicomponent alloys

Various models of oxidation assume formation of a single-phase, dense oxide layer, such as  $\text{Al}_2\text{O}_3$ . In the case of binary and multicomponent alloys, the formed oxide scales may be complex. There are numerous models describing formation of hetero-phase scales on alloys [63]. Superalloys may form both single-phase and hetero-phase scales depending on an alloy's composition. In general, multi-phase scales are considered as non-favorable unless they contain a continuous layer of a protective oxide, such as  $\text{Al}_2\text{O}_3$  or  $\text{Cr}_2\text{O}_3$ . The alloys that are capable of forming the continuous oxide layers of  $\text{Cr}_2\text{O}_3$  and  $\text{Al}_2\text{O}_3$  are so-called chromia-formers and alumina-formers respectively [50, 64]. For applications where the temperature exceeds  $900\text{ }^\circ\text{C}$ , alumina-formers are more desirable due to the stability of  $\text{Al}_2\text{O}_3$  at very high temperatures [50]. The required aluminum content to create and maintain a protective  $\text{Al}_2\text{O}_3$  layer on Ni-Al binary alloys at  $1000^\circ\text{C}$  varies between 7 to 12.5 wt% of Al. The minimum required value of Al to form and maintain a protective  $\text{Al}_2\text{O}_3$  scale on binary Ni-Al alloys at  $1000^\circ\text{C}$  can be decreased by the “third element effect”, in which other alloying elements like Cr promote alumina formation [64, 65].

Taking into consideration the oxide scale formation and chemical composition of Ni-Al-Cr-based superalloys [66], one can distinguish three main groups (Figure 2.7). The outer scale of the Ni-2Cr-4Al (wt%), corresponding to the group I, was composed of NiO, while the subscale precipitate was a mixture of  $\text{Cr}_2\text{O}_3$ ,  $\text{Al}_2\text{O}_3$ , and  $\text{Ni}(\text{Cr}, \text{Al})_2\text{O}_4$ . These findings indicate that nickel is oxidized externally to produce a continuous scale, whereas the internal oxidation of both Cr and Al results in a discontinuous subscale of  $\text{Cr}_2\text{O}_3$  and  $\text{Al}_2\text{O}_3$ . As a result, the oxidation rates of these alloys are likely controlled by transport through the NiO scale. The alloy exhibited higher oxidation rate than pure Ni.

The Ni-20Cr-2Al (wt%) alloy belonging to the group II showed a dense outer scale of  $\text{Cr}_2\text{O}_3$  and a subscale containing  $\text{Al}_2\text{O}_3$  precipitates. Selective oxidation of Cr and Al leads to the formation of the external  $\text{Cr}_2\text{O}_3$  scale and the internal  $\text{Al}_2\text{O}_3$  subscale. The diffusion through the Al-doped  $\text{Cr}_2\text{O}_3$  scale controls the oxidation rate.

The group III alloy, Ni-20Cr-4Al (wt%), showed the outer scale that was composed entirely of  $\text{Al}_2\text{O}_3$ , with a small amount of Cr in solution. The findings for this group of alloys suggest that Al undergoes selective oxidation and that the diffusion through the external  $\text{Al}_2\text{O}_3$  scale governs the oxidation rate.

Besides the influence of the Al-content, the temperature dependence is especially noteworthy. For Ni-based alloys, increasing the exposure temperature may allow a transition

from group I and II towards group III for one and the same alloy [67]. The discussed groups [66] may also be found in the case of Fe- and Co-based alloys.

The oxidation behavior of numerous alloys can be divided into two stages: transient oxidation, which is followed by a steady-state oxidation period [68].

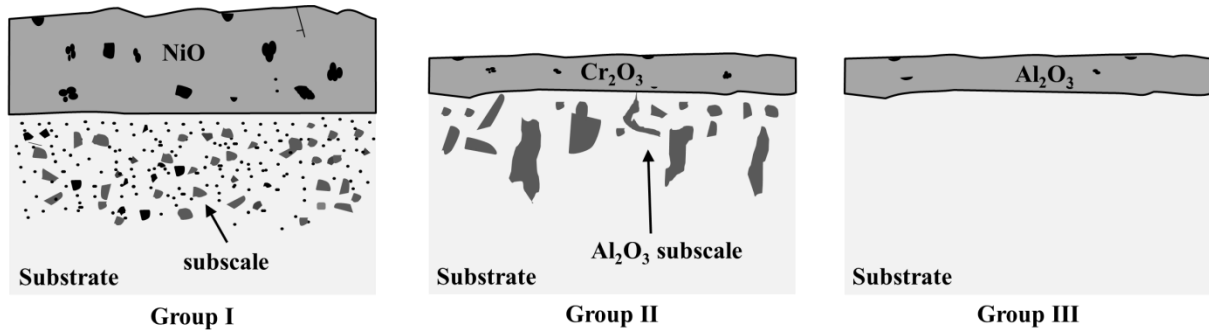


Figure 2.7: Schematic presenting oxide scale microstructure related to three groups of Ni-Al-Cr alloys. Adapted from [66].

### 2.3 Oxidation of $\gamma$ - $\gamma'$ cobalt-based superalloys

As it was mentioned, new Co-based alloys suffer from high temperature oxidation. In the early stages of development, the oxidation resistance of the  $\gamma$ - $\gamma'$  alloys was considerably inferior to that of Ni-based superalloys. In comparison to Co, pure Ni exhibits higher oxidation resistance, and the development of a protective layer in Co-based alloys is considerably more difficult than in Ni-based alloys. Although an increase in the exposure temperature can lead to a transition from group I and II to group III in the same Ni-Al-based alloy [67], the content of Al required to ensure continuous alumina scale growth increases with rising temperature for Co-Al alloys [69]. If the Al levels are too low, a CoO scale is formed on the outer layer, under which  $\text{CoAl}_2\text{O}_4$  and  $\text{Al}_2\text{O}_3$  precipitates are present. In opposite to conventional Co-based superalloys, which are oxidation resistant, new alloys cannot be alloyed by the same amount of Al and Cr due to the  $\gamma$ - $\gamma'$  microstructure stability. Therefore, the development of Co-based superalloys presents a significant challenge to researchers.

The initial references to the high temperature oxidation of the novel  $\gamma$ - $\gamma'$  Co-based superalloy system were reported in 2010 [36]. Pollock et al. investigated various ternary and multicomponent alloys based on Co-Al-W system. The work revealed that ternary Co-Al-W alloys and higher order alloys have lower oxidation resistance compared to Ni-based single crystals due to lack of a protective oxide layer. At 900 °C, oxidation of the Co-based alloys resulted in the formation of a thick and non-protective CoO layer, followed by an inner layer containing a mixture of CoO and other oxides, an inner alumina layer, and a  $\gamma'$ -free zone of  $\gamma/\text{Co}_3\text{W}$ . To improve the oxidation resistance, the authors of the study chromized Co-7.8W-7.8Al-4.5Cr-1.5Ta to create a protective  $\text{Cr}_2\text{O}_3$  layer during high temperature oxidation. Although successful, this protection was only maintained up to 950°C. Therefore, further improvements are necessary to enable the formation of a continuous external alumina layer on the surface of Co-based superalloys. Figure 2.8 shows the oxide scales formed on the Co-Al-W alloy at various temperatures after 100 h of oxidation. The images clearly indicate that the alloy does not form a protective scale in the temperature range of 500-1000 °C. Instead, it consistently exhibits an external layer consisting of non-protective Co-oxides.

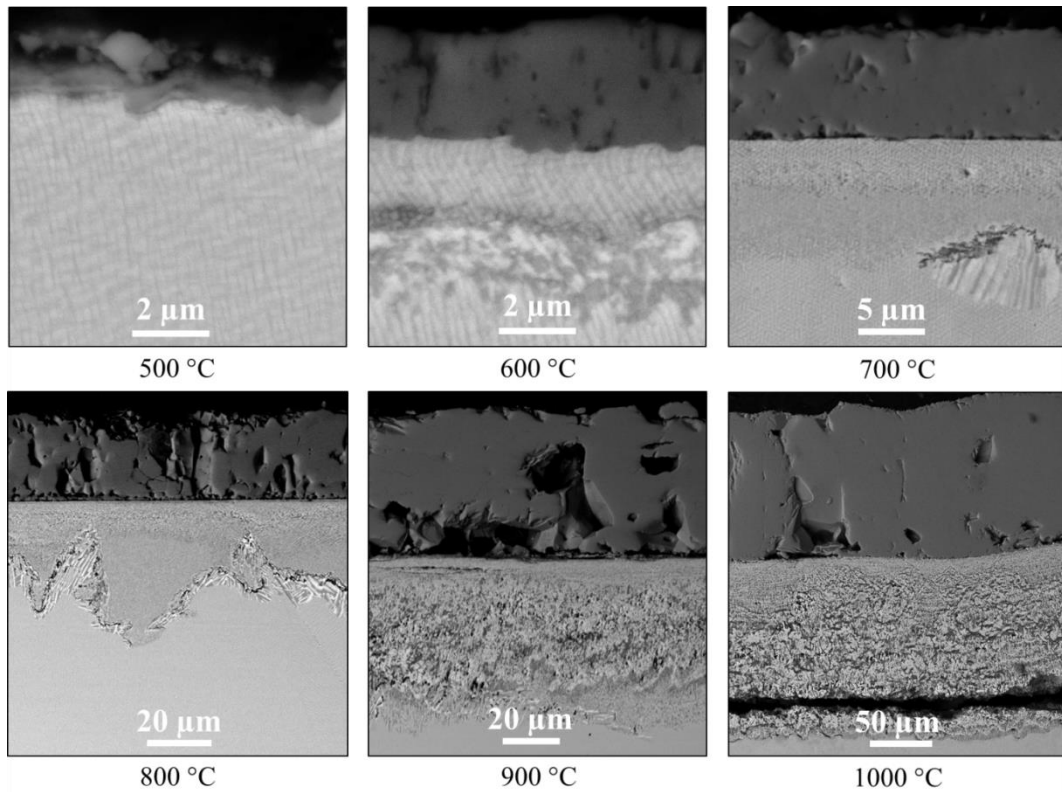


Figure 2.8: SEM micrographs of the oxide scales formed on Co-9Al-9W (at%) alloy after oxidation at 500-1000 °C for 100 h [author's own research].

In the same year, Xu et al. conducted the study on the oxidation of Co-8.8Al-9.8W-2X (X= Ta, Ti, Mo, Nb) alloys at 800 and 900 °C [70]. This research revealed the harmful impact of Nb, Ti, and Mo on the oxidation resistance of new Co-based alloys at 800 °C. At 900 °C, all alloying elements reduced the oxidation rate of the alloys, while tantalum decreased the oxidation rate at both 800 and 900 °C. It is important to note that the total duration of the oxidation test was only 100 h.

Further investigations on the effect of alloying on oxidation resistance of new Co-based alloys were conducted in 2011 by Klein et al [71]. The investigation focused on determining the thickness of the oxide layer in ternary Co-9Al-9W-X (X=0.12B, 0.08B, 2Ta) and quaternary Co-9Al-9W-Y (Y=2Ta-2Cr, 2Ta-2Nb, 2Ta-2Si, 2Ta-2V, 2Ta-2Mo, 2Ta-2Ir) alloys. The alloys containing B were subjected to oxidation at 800 and 900 °C for 500 h, while all other samples were oxidized for 400 h at 900 °C. The results showed that only the 2Ta2Si, 2Ta2Mo, and 2Ta2Ir alloys exhibited a thinner oxide scale after oxidation, while the other alloys had a higher thickness of the oxidized layer compared to the reference alloy. The authors also noted the beneficial effect of B on high temperature oxidation, which led to the formation of a continuous inner alumina layer at 800 °C and improved the scale adhesion.

A few months later, Klein et al. conducted another study [72] on the influence of B and Cr on the high temperature oxidation of Co-based superalloys. They observed a favorable effect of B, which was attributed to its accumulation in the inner oxide layer, leading to the increase in oxidation resistance by promoting the formation of the inner  $\text{Al}_2\text{O}_3$  layer. Additionally, co-doping with Cr and B may have a positive effect on oxidation resistance through formation of protective inner chromia and alumina layers when Cr-containing samples were oxidized at 800 °C. Xu et al. determined the activation energy of oxidation of various Co-Al-W superalloys at high temperatures [73].

One year later, Yan et al. examined cyclic oxidation of  $\gamma$ - $\gamma'$  Co-based alloys [74]. They found Co-based alloys prone of oxide spallation. In 2013, Klein et al. studied co-doping of Co-Al-W-B alloys with Ni (9, 18 at%) and with Si (2 at%) [75]. Moreover, they evaluated oxidation resistance of the Co-9Al-9W-0.12B (at%) alloy doped with 0.005% Y. The authors found beneficial effect of Si on oxidation resistance of the alloys at 800 and 900 °C, whereas addition of Ni caused increase of the oxidation rate [76]. Fan et al. [77] reported deterioration of the isothermal oxidation resistance of Co-9Al-9W-2Ta-0.02B (at%) alloy upon Mo alloying (2 and 4 at%).

Klein et al. conducted another study on the B-containing alloys, namely performed isothermal oxidation experiments on the single-crystal and polycrystalline Co-Al-W-B superalloys at temperatures ranging from 800 to 1000 °C [78]. The results revealed that the polycrystalline variant displayed better oxidation resistance at lower temperatures (800 and 900 °C), possibly due to grain boundary diffusion dominance. In contrast, the absence of grain boundaries in the single crystalline variant caused lower accumulation of B in the inner oxide layer, thereby inhibiting the formation of the protective inner  $\text{Al}_2\text{O}_3$  (Figure 2.9).

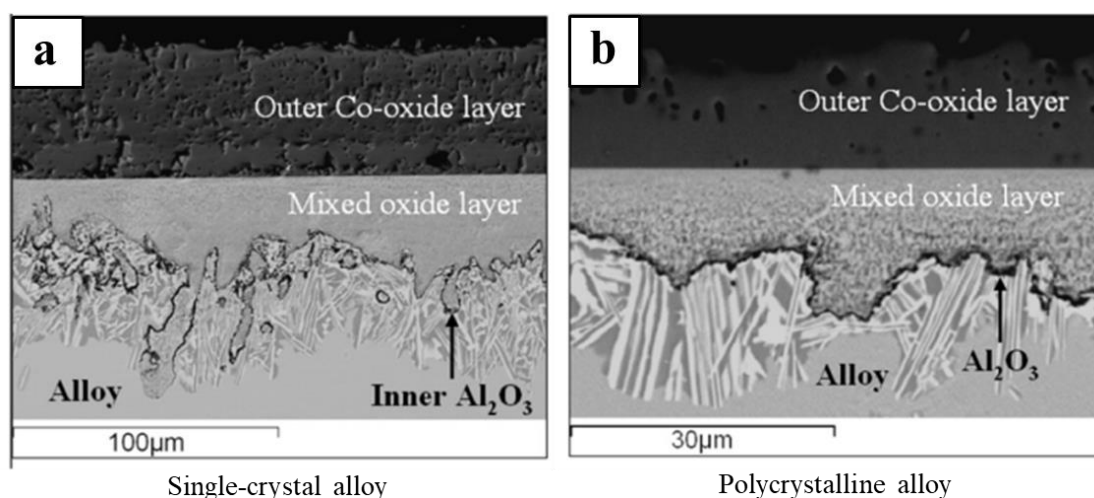


Figure 2.9: SEM micrographs of Co-9Al-9W-0.12B alloy oxidized at 800 °C for 500 h: a) single-crystal alloy; b) polycrystalline alloy. Adapted from [78].

Furthermore, Klein et al. carried out thermodynamic modelling of the high temperature oxidation behaviour of ternary  $\gamma'$ -strengthened Co–Al–W superalloys [79]. Yan et al. investigated effect of alloying (Cr, Fe, Si, Ni, Ta, Mo, Ti, V, Ni and V, Cr and Ni) on the oxidation behaviour of Co–Al–W superalloys [80, 81]. They found alloying Cr, Fe and Si into Co–7Al–7W beneficial. Alloying with Cr, Fe, and Si was found to improve the oxidation resistance of the Co-7Al-7W (at%) alloy. The addition of 10% Cr resulted in the most significant enhancement.

Weiser et al. carried out In-situ investigation of the oxidation of the Co-9Al-9W (at%) alloy in the environmental SEM [82]. They observed that oxidation initiates not necessarily at the grain boundaries, and that both the onset temperature (which lies between 600 and 655 °C) and the oxidation rate are influenced by the crystallographic orientation of the crystallites. Neumeier et al. [40] developed the alloys (see Figure 2.3), which show excellent mechanical properties and oxidation behavior much better than that of previous Co-Al-W superalloys due to a high Cr content and addition of Si. The improvement of the oxidation properties was achieved also by Ito et al. [83], which studied influence of Cr addition (from 2 up to 10 at%) on oxidation rate of Co-20Ni-9Al-9W-xCr alloys.

In 2016, Zhong et al reported detrimental effect of alloying elements such Mo, Ta, and Hf on high temperature oxidation of the Co-9Al-9W-2Ta-0.02B (at%) alloy [84]. In their study, Zenk et al. observed that increasing Co:Ni ratio can deteriorate oxidation resistance of Co–Ni–9Al–8W–8Cr–0.04B alloy [85]. Stewart et al. utilized the combinatorial approach coupled with rapid oxide screening based on photo-stimulated luminescence spectroscopy and the Calphad database to outline regions of composition space giving rise to  $\alpha$ -Al<sub>2</sub>O<sub>3</sub> scales and two-phase  $\gamma$ – $\gamma'$  microstructures [86-88]. The authors demonstrated that relatively thin layers of continuous  $\alpha$ -Al<sub>2</sub>O<sub>3</sub> may be achieved at 1100 °C after 1 h of the isothermal oxidation exposure of alloys containing >11 at% Al, >4 at% Cr, between 7 and 10 at% W, and >26 at% Ni [88]. Wang et al. studied the effect of rare earth elements on the oxidation behavior of the  $\gamma$ – $\gamma'$  Co-Al-W [89] and Co-Al-Cr alloys [90]. The addition of elements such as La, Ce, Dy, and Y resulted in only a minor improvement in oxidation resistance. Ismail et al. presented experimental evidence that oxidation-resistant, protective oxide scales can be formed in Co–Ni–Al–W–Cr superalloys [91]. Furthermore, alumina layers can be achieved during oxidation of the Co–Al–W–Ni–Si  $\gamma'$ -forming alloys [92].

In 2018, Chater et al. used the FIB-SIMS technique in combination with two-step tracer oxidation to investigate ion transport mechanisms through oxide scales formed on mixed Ni- and Co-based alloys at 900 °C [93]. Moreover, Weiser et al. utilized the same techniques to

evaluate oxidation mechanisms during the transient stages of scale growth between 800 °C and 900 °C on single-crystalline Co-Al-W alloys [94]. All investigated oxide scales showed evidence of counter-current transport of Co cations and oxygen after exposure in the considered temperature range (Figure 2.10). The transportation of oxygen through  $d_1$  towards the  $d_2/d_3$  interface drives the development of an internal oxidation zone. The general trend of higher W contents leading to lower oxidation rates within the transient oxidation stage was observed. W can have a positive impact on the oxidation rate at 900 °C [92, 95]. On the other hand, decreasing the W content can improve the oxidation resistance significantly at 1000 and 1150 °C [92]. Weiser et al. carried out the comprehensive study on early stages of scale formation during oxidation of the single-crystal Co-Al-W alloy at 900 °C [96].

Forsik et al. presented the Co-Ni-Al-W-Cr-Ti alloy with oxidation resistance higher than the benchmark Waspaloy [97]. This alloy exhibit formation of a protective  $Al_2O_3$  layer up to 1000 °C. The cyclic oxidation behavior of Co-Al-W and W-free Co-Al-Mo-Nb alloys was studied [98]. The findings indicate that the Co-Al-Mo-Nb alloys exhibit significantly poorer oxidation resistance compared to the base alloy.

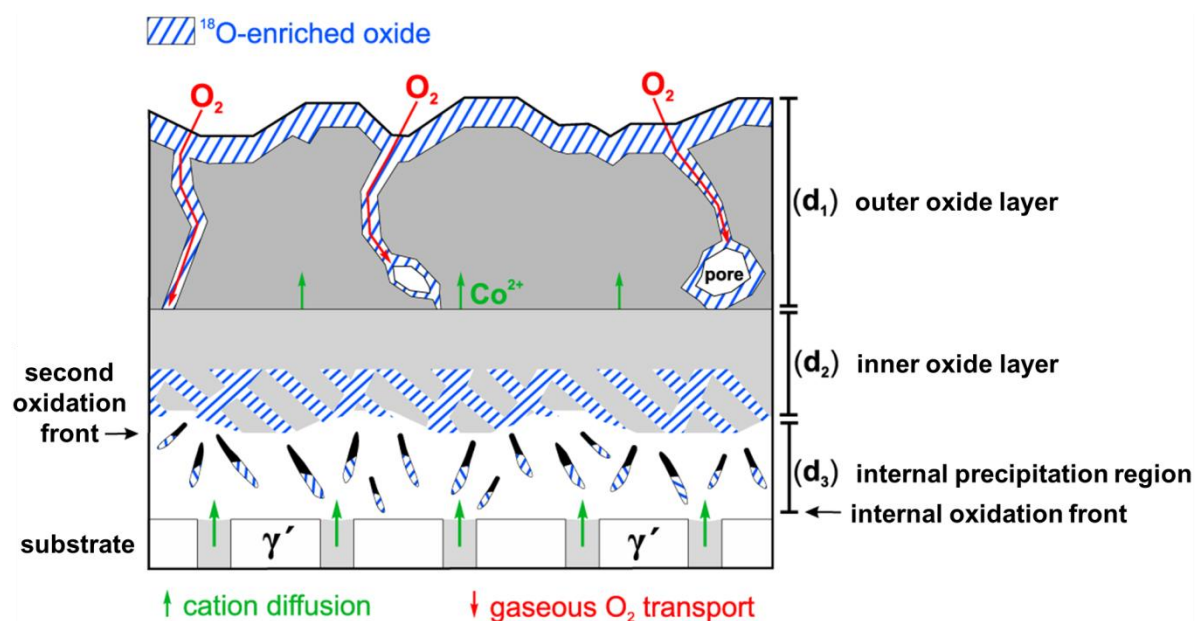


Figure 2.10: Schematic illustrating the distribution of  $^{18}O$  in multilayered oxide scales Co-Al-W alloys following two-stage tracer exchange experiments. Adapted from [94].

The effectiveness of the halogen effect and the influence of the Co to Ni ratio on scale growth of the Co-Ni-Al-W-Cr alloys were both examined by Weiser et al. [99]. The Ion-implantation with fluorides prior to thermal exposure can facilitate the external growth of protective  $Al_2O_3/Cr_2O_3$  scales for alloys with high Ni contents. Gao et al. investigated oxidation behavior of the Co-Ni-Al-W-Cr-Ti-Ta-B-Zr alloys with various Ni-content [100].

Bantounas et al. reported Cr-containing W-free Co alloys which were found to have relatively low density, good oxidation resistance with coherent alumina and chromia scales at 800 °C [101]. Moreover, the W-free alloys, from Co-Ni-Al-Mo-Ta system, were studied in view of their oxidation behavior at 800 °C [102]. The high temperature cyclic oxidation and spallation of oxide scales in Co-Al-W alloys were investigated in detail [103].

Substantial progress has been made in the development of Co-based alloys capable of forming protective oxide scales since 2020 [104-121]. Nowadays, optimized compositions allow for the production of Co-based superalloys capable of forming protective scales and with oxidation resistance comparable to Ni-based superalloys. Obtaining of protective scales is possible at temperatures of 1000 °C and above [104, 106, 111, 114, 115]. The relationship between the parabolic rate constants and reciprocal temperature of the Co-Ni-Al-W-based alloy systems, Co-Ni-Al-Mo-based alloy systems, and some nickel-based superalloys at 700–1000 °C (Figure 2.11) were presented by Quian et al. using data from their study [117] and available data from the literature. Various Co-based alloys exhibit comparable oxidation kinetics with chromia-formers, although they also produce protective alumina layers. The oxidation resistance of the newest Co-based superalloys is still below the level of the most advanced Ni-based superalloys. Moreover, it is important to provide both excellent oxidation resistance together with high solvus temperature and enhanced creep properties. Although compared to first studies on the oxidation of new Co-based superalloys in 2010, the improvement degree is impressive, there is still a room to improve oxidation resistance of the alloys.

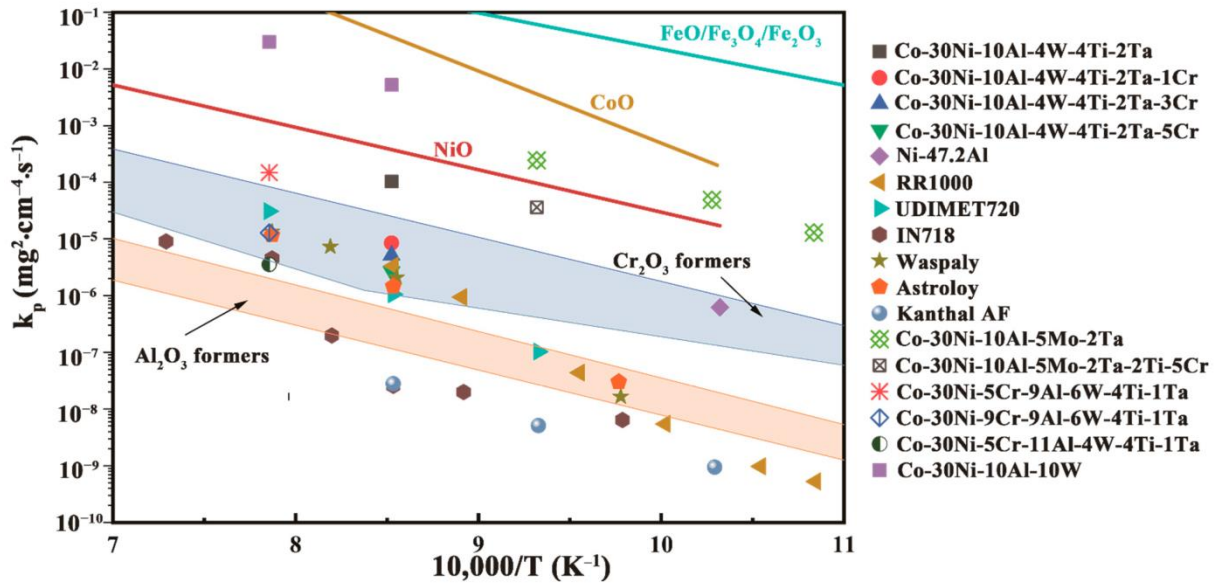


Figure 2.11: Parabolic rate constants versus reciprocal temperature for various Ni- and Co-based superalloys. The shaded areas represent the typical values of chromia- and alumina-forming alloys. From [117].

It is necessary to transform base Co-Al-W alloys into multicomponent alloys to enhance their oxidation resistance. Within the literature data, one can find numerous attempts of alloying with Cr and Si, which is not unexpected due to the influence of these elements on oxidation behavior of metallic alloys. A considerable number of investigations were conducted on the doping or co-doping with B [71, 72, 75, 76, 78, 120], which added in small quantities can considerably enhance oxidation resistance and facilitate the formation of protective scales. By reviewing the literature data on new group of superalloys, one can note that relatively low attention has been paid to reactive elements (RE) and their introduction to the  $\gamma$ - $\gamma'$  Co-based alloys.

## 2.4 Reactive elements effect

The reactive elements are sometimes termed “magic dust” due to their remarkably beneficial effects on high temperature oxidation of alloys [122]. The RE dopants were first patented by Pfeil et al. [123, 124] for chromia-forming alloys more than 85 years ago. Over the years, the use of RE in high performance, high temperature materials has been the subject of much research and controversy. While mechanistic models to explain the role of RE have been proposed and revised, their incorporation into such materials is still deemed essential. As a result, the RE effect remains a significant and ongoing issue in materials science [125]. The term “reactive element” has been coined to replace “rare earth” in order to better capture the beneficial effect of oxygen-active additions, such as Y, La, Ce, and Hf, on high temperature oxidation [122]. The term “reactive elements effect” does refer to the beneficial effect of adding rare earth elements to different alloys, but it specifically refers to the improvement in high temperature oxidation resistance.

Typically, when adding RE to alloys, the most common methods involve adding them as alloy additions in small amounts, ranging from 0.05 to 0.5 at%, or as RE oxide dispersions in concentrations ranging from 0.2 to 2 vol%. Surface doping, such as ion implantation or oxide coating, can also be effective in improving properties of alloys [126]. RE are known to have a beneficial effect on isothermal oxidation resistance and oxide scale adherence of chromia- and alumina-forming metallic materials. There are multiple mechanisms that explain how reactive elements influence oxidation behavior of alloys.

### 2.4.1 Reduction in scale growth rate

The growth of oxide scale during isothermal oxidation of different alloys can be decreased by the proper addition of RE. The mechanisms responsible for improving oxidation resistance were proposed in the XX century, and some of them have been further revised.

#### Facilitation of selective oxidation

One well-known effect of RE is that when they are introduced to alloys in the form of alloying elements or dispersed oxides, they enhance selective oxidation of Al or, in particular, Cr. As a consequence, the critical Cr content necessary to form a protective, chromia scale can be lowered. While this effect is widely acknowledged, it is not necessarily unique to the presence of RE. The introduction of these elements by alloying or oxide dispersions can achieve the selective oxidation effect by pinning grain boundaries of an alloy and creating subgrain structures. This, in turn, leads to the formation of more short-circuit pathways for the diffusion of Cr or Al within the alloy. The selective oxidation can be enhanced through

methods such as reducing the alloy grain size or increasing the dislocation density via cold working. These improvements can occur even without the use of RE doping [127, 84].

#### Change in the scale growth mechanism

The presence of RE ions during oxidation has another impact, as they have a tendency to segregate at the oxidizing interface and incorporate into grain boundaries of the  $\text{Al}_2\text{O}_3$  scale. This phenomenon is supported by the dynamic segregation theory (Figure 2.12), which is now a part of the lexicon of RE effects and has been reinforced by both earlier and subsequent research [128, 129]. According to this theory, certain large oxygen-active elements present in the alloy diffuse toward the scale-gas interface due to the oxygen potential gradient in the metal-scale-gas system. However, the effects of this outward transport are not fully realized until a dense, external scale of either  $\alpha\text{-Al}_2\text{O}_3$  or  $\alpha\text{-Cr}_2\text{O}_3$  is formed. During the initial stages of oxidation, where metastable or base-metal oxides are dominant, the RE effect on the scale growth mechanism is not observed. As RE ions move upwards, they first segregate to the metal-oxide interface. Then, the outward-diffusing RE ions follow the fastest path to the gas interface, which is through the scale grain boundaries. When the concentration of RE ions on the boundaries reaches a critical level, the segregation-diffusion of RE ions produces two effects.

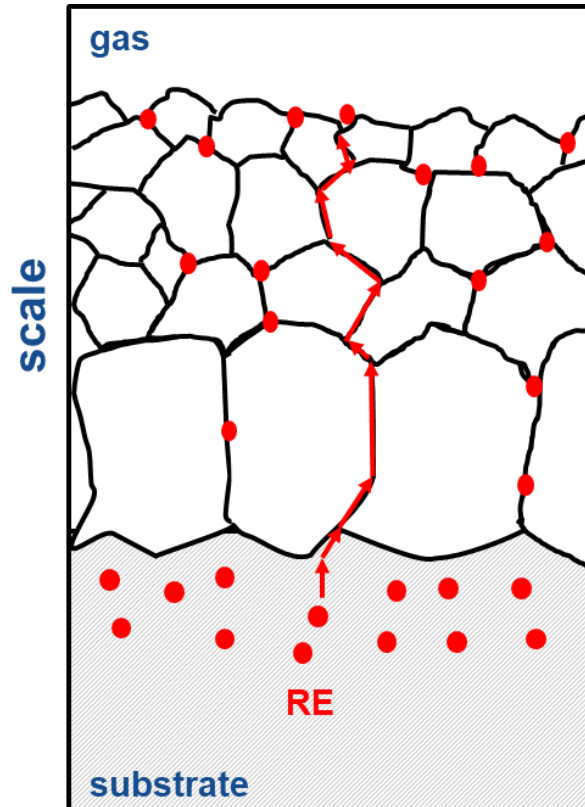


Figure 2.12: Schematic presenting the outward diffusion of RE ions during oxidation. Adapted from [128].

One effect of the presence of large RE ions is their slower diffusion compared to the native cation (either Cr or Al), which inhibits the usual outward short-circuit transport of cations along the scale grain boundaries. In the formation of  $\alpha$ -Cr<sub>2</sub>O<sub>3</sub> and  $\alpha$ -Al<sub>2</sub>O<sub>3</sub> scales, the inward transport of O ions along the scale grain boundaries becomes the new rate-limiting step. At a macroscopic level, the inhibition of outward cation transport results in a decrease in the parabolic oxidation rate constant. A difference between Cr<sub>2</sub>O<sub>3</sub> and Al<sub>2</sub>O<sub>3</sub> can be observed, where the inhibition of cation transport has a greater effect on the parabolic rate constant in the Cr<sub>2</sub>O<sub>3</sub> scale due to its higher ratio of cation to anion transport.

Furthermore, RE-containing alloys exhibit the growth of columnar scales which as a result of stress-free growth mainly driven by inward oxygen diffusion and preferential growth at the metal interface. In contrast, undoped alloys tend to form equiaxed scales, which result from a combination of inward oxygen diffusion and outward aluminum diffusion [128, 130].

#### **2.4.2 Improvement of scale adherence**

It is believed that the addition of RE to alloys provides the greatest benefits in terms of improving the adherence of the scale to the metal, particularly for alloys that form alumina scales. These alloys are less benefited by a reduction in scale growth rate compared to alloys that chromia-formers.

##### Preventing sulfur segregation

One of the major RE roles is to prevent sulfur segregation at the oxide-metal interface, which is substantially detrimental to oxide scale adherence and difficult to observe due to low S-contents in superalloys. The reduction of the interfacial segregation of S may be achieved by formation of thermodynamically stable RE sulfides (e.g. Y<sub>2</sub>S<sub>3</sub>) due to sulfur reactivity of RE and their low solubility in the base alloy (Fe, Ni, Co). Moreover, by the same way, the RE-dopants may react with O, C (Zr, Hf) and other impurities [129].

##### Vacancy sink

RE doping also has another aspect, which is a reduction in void formation at the metal-scale interface. This is due to the internal RE oxides or complexes acting as vacancy sinks, which prevent void formation caused by substantial outward Al growth and Al vacancy injection. In contrast, undoped alloys typically exhibit large interfacial voids and extensive spallation over large areas when a thick scale forms during air oxidation of alumina-forming alloys. The segregation of RE affects surface energy, thus inhibiting interfacial void growth by decreasing the driving force for the void to grow. However, the mechanism through which the addition of RE reduces void formation is not yet fully understood [125, 129].

### Mechanical properties of the scale

Undoped  $\alpha$ -Al<sub>2</sub>O<sub>3</sub> scales are expected to exhibit enhanced scale plasticity, which is associated with non-adherent behavior. On the other hand, RE-doped scales are expected to be more resistant to deformation and less plastic, and are associated with adherent behavior [129].

### Keying effect

The formation of oxide keys or stringers is a well-known phenomenon that occurs when RE is added to an alloy and internally oxidized beneath the scale (Figure 2.13). This has attracted attention as a mean of improving scale adhesion. The so-called “keying” or “pegging” effect was the earliest observation and proposed mechanism for scale adhesion. It is believed that the RE, which are capable of oxidizing at a lower pO<sub>2</sub> than Al, undergo partial oxidation near the surface and create rapid diffusion pathways for the growth of Al<sub>2</sub>O<sub>3</sub>. However, growth of alumina occurs in a non-planar manner. The intrusion of RE-oxides into the oxide scale/metal interface can provide interlocking mechanical strength, which improves the adhesion between the scale and the metal. Even at lower dopant levels, adherence can still be achieved [129-131].

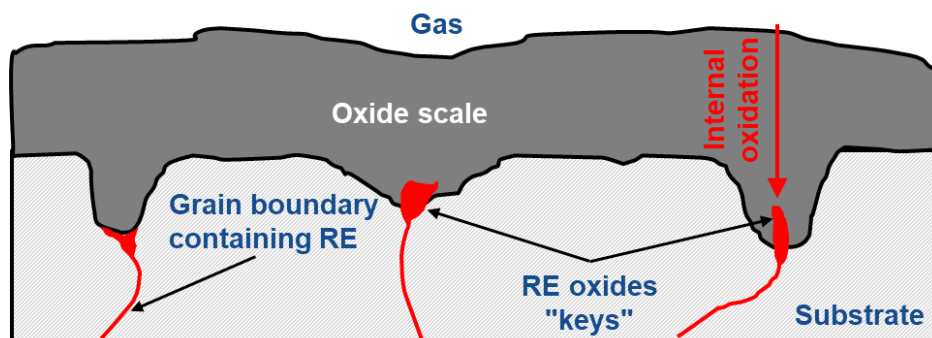


Figure 2.13: Schematic of the keying effect.

### **2.4.3 Reactive elements in cobalt-based alloys**

The reactive elements have been successfully utilized in improvement of oxidation properties of conventional Co-based alloys [132-141]. However, it should be noted that in most cases where reactive elements were successfully utilized to improve the oxidation properties of superalloys, the alloys contained high amounts of Cr, which cannot be maintained in the new  $\gamma$ - $\gamma'$  Co-based alloys.

Wu et al [142] and Zeng et al. [143] studied high temperature oxidation of the binary Co-Y alloys. According to Zeng et al., activity of Co in Y-rich phase (Y<sub>2</sub>Co<sub>17</sub>) is substantially lower than that in  $\alpha$ -Co. Moreover, the internal oxidation of Y<sub>2</sub>Co<sub>17</sub> results in formation of Y<sub>2</sub>O<sub>3</sub>.

Presence of yttrium oxide may hamper outward Co diffusion, since for  $Y_2O_3$ , oxygen defects predominate and oxygen diffusion is much faster than cation diffusion.

Some attempts or RE-introduction to  $\gamma'$ -forming Co-based alloys have been undertaken [76, 89, 90, 144-151]. The Y-effect on oxidation behavior of new Co-based alloys was mentioned in the study of Klein et al. [76]. They found that Y did not improve the oxidation resistance compared to the Co-9Al-9W-0.12B (at%) alloy. Y in the 0.12B0.005Y alloy was found to diffuse mainly into the inner oxide layer, likely forming  $Y_2O_3$ . The conclusion was made based on the observation that Y accumulates mostly in the inner oxide layer, similarly to W. However, such accumulation may result from overlapping of the Y-L $\alpha$  (1.922 keV) and W-M $\alpha$  (1.774 keV) lines. Therefore, detection of small amount of Y in the neighbourhood of W is difficult. Moreover, elemental mapping acquisition of areas composed of both W and Y may be tricky for the same reason and reveal presence of Y in areas, where only W is located. It can be seen in Figure 2.14. The same area analyzed using the accelerating voltage of 30kV and with consideration of Y-K $\alpha$  (14.931 keV) instead of Y-L $\alpha$ , shows lack of yttrium in W-rich areas.

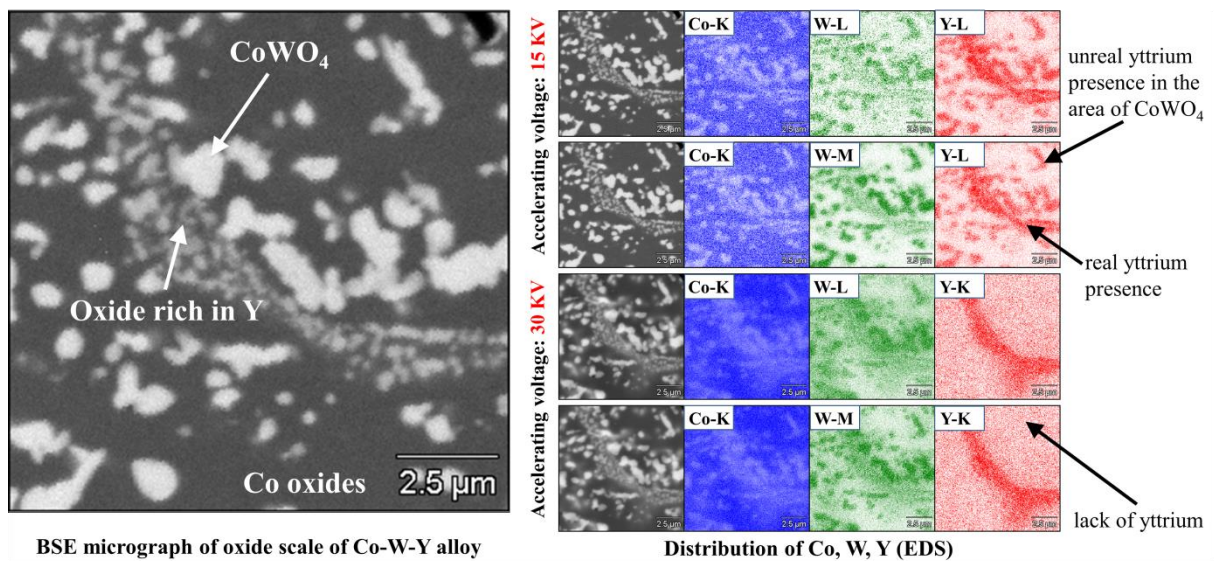


Figure 2.14: Microstructure of oxide scale formed on ternary Co-W-Y alloy and distribution of Co, W, and Y within the oxidized area (EDS) [author's own research].

The same note may be done in the case of the studies carried out by Wang et al. [89, 90]. In the all mentioned works [76, 89, 90], the amount of RE added was very small. Such addition is difficult to control during preparation of alloys. Except for the apparent accumulation of Y in the inner oxide layer, Y was not found in either the alloys' microstructure or oxide scale. The Y-doping was studied by Ma et al [144] in view of the microstructure and grain boundary morphology evolution of the Co-9Al-9W-2Ta-0.02B alloy.

They found Y to segregate at grain boundaries. The positive impact of Ce was reported for high temperature tensile behavior [145], oxidation [146], and hot corrosion resistance [148] of the Co-Al-Mo-Ta-B alloys. Zhong et al. reported that a mechanism that involves both the rapid formation of a continuously protective  $\text{Al}_2\text{O}_3$  layer and the thickening of the  $\text{Al}_2\text{O}_3$  layer has contributed to the excellent oxidation resistance upon adding Ce [146]. However, no mechanisms have been proposed to explain the formation of the inner protective alumina layer.

The microstructural role of Ce was found to be similar compared to Y [144]. None of the authors reported Y- or Ce-containing phases. Xu et al. found Nd to improve the compressive behavior of the Co-8.8Al-9.8 W alloy [147]. Besides nano  $\text{Nd}_2\text{O}_3$ , the authors did not observe any Nd-containing phases, what is interesting taking into consideration the excessive content of the dopant (3 at%). No intermetallic phases containing RE (Y, Ce) were reported in other studies [89, 90, 144-146, 148], except for Ma et al., who found Y to segregate to the  $\text{Co}_3(\text{Ta}, \text{W})$  phase [144]. However, other authors did not indicate the role of Ce in the as-cast microstructure. In addition, the authors who studied Co-Al-W and Co-Al-W-Cr alloys [89, 90] containing rare earths did not provide any information on their fabrication process, which makes it more difficult to compare the results between different series of alloys. Xu et al. [147] reported that the Co-Al-W-Nd alloys were fabricated via vacuum arc melting using metallic powders (Co, Al, W) and  $\text{Nd}_2\text{O}_3$  oxide powder as feedstock materials, which is atypical for this melting method. Other studies revealed that Ce can improve oxidation resistance of the Co-Al-W alloys, but also decrease their melting temperature [149, 150]. Other studies imply that the addition of Ce can enhance the oxidation resistance of Co-Al-W alloys but can also reduce their melting temperature [149, 150]. Moreover, in both as-cast and as-aged states, Ce can form intermetallic phases with Co and Al [150]. The similar findings may be done in the case of the Co-Al-W-Y alloys, whose oxidation properties were studied by the author of the dissertation and his co-workers in detail [151].

The current literature on the effects of RE on the microstructure and properties of recently developed Co-based alloys is insufficient. The available information is not comprehensive and lacks systematic studies. Therefore, it is necessary to conduct detailed and systematic research on this topic to obtain a better understanding of the influence of RE on the properties of these alloys.

## 2.5 Summary

Co-based superalloys strengthened with  $\gamma'$  phase have emerged as highly promising metallic materials for high temperature applications. There is still room for the development of new alloys, particularly regarding their high temperature oxidation behavior. One of the possible ways is doping with RE, which has proven to be a successful method for enhancing the high temperature oxidation resistance of  $\gamma'$ -strengthened Ni-based superalloys. Although the effects of RE have been extensively studied for decades, there is still a significant level of interest in this topic, as evidenced by the emergence of this thesis and the likelihood that it will not be the last PhD thesis related to the RE effect.

The review of the current state of the art on the effect of RE on Co-based alloys, particularly the new generation, highlighted significant limitations. The available literature provides only concise information on the new cobalt superalloys doped with these elements. The effects of RE on new  $\gamma$ - $\gamma'$  Co-based alloys have not yet been comprehensively studied, including various aspects such as properties, manufacturing, thermal behavior, as-cast and as-heat treated microstructure. Therefore, it can be concluded that there is a gap in the current state of the art that needs to be addressed. The potential advancements in this area served as a strong motivation for conducting the research and preparation of this thesis.

To systematically investigate the effects of doping new generation superalloys with RE, it is recommended to begin with modifying the basic Co-Al-W alloy. Following that, the advantages of introducing RE can be investigated in the recently developed multicomponent oxidation resistant superalloys.

The prediction of RE effect on high temperature oxidation behavior of the Co-Al-W alloys can be challenging due to the fact that majority of examples of doping superalloys with RE concerns alloys that are alumina- or chromia-formers. The main aim of the work is to investigate in detail influence of RE addition of oxidation behavior of the base Co-9Al-9W (at%) alloy. The supplementary aim is to evaluate the microstructure evolution in the Re-modified alloys from as-cast to as-aged state with particular attention to the RE presence.

The thesis statement is following: **The introduction of reactive elements such as La, Nd, Dy, or Y to the Co-9Al-9W alloy (at%) may improve its high temperature cyclic and isothermal oxidation resistance to a certain extent, whereas it does not considerably change the oxidation mechanism and does not promote the formation of a protective alumina layer.**

## 3. Experimental

### 3.1 Selection of materials and research programme

The reference alloy for the research was Co-9Al-9W (at%). Such composition allows for obtaining of the  $\gamma$ - $\gamma'$  microstructure. Although the newest multicomponent alloys provide better properties, the ternary Co-Al-W alloy is the most studied alloy due to the fact that it was the first promising  $\gamma'$ -forming Co-based alloy. Therefore, this alloy was selected as the first for systematic studies on the introduction of RE to the  $\gamma$ - $\gamma'$  Co-based alloys. The preliminary studies carried out by the author of the dissertation included two sets of RE considered, having oxidation states III and IV, i.e., RE(III): La<sup>3+</sup>, Ce<sup>3+</sup>, Nd<sup>3+</sup>, Dy<sup>3+</sup>, Y<sup>3+</sup> and RE(IV): Zr<sup>4+</sup>, Hf<sup>4+</sup>, and Ce<sup>4+</sup>.

All the aforementioned elements were proved to increase the oxidation properties of metallic high temperature alloys. Among them, the most studied reactive element was Y. For the most detailed studies, included in the dissertation, four reactive elements were selected: La, Nd, Dy, Y. The nominal content of each RE added to the reference alloy was 0.1 at%. Such amount allows for the detection of RE addition in the alloy and is in the range typically used for Ni- or Fe-based alloy. The level of 0.1 at% is not necessarily optimal. The content of RE should be tailored, taking into consideration the mechanical properties and oxidation resistance. Such an evaluation should be a part of further studies. Since the most characteristic difference between the studied alloys is the type and amount of RE addition or its lack, the reference alloy is labeled as “0RE”, while other alloys are “0.1La”, “0.1Nd”, “0.1Dy”, and “0.1Y” respectively.

The research programme includes two steps, of which the first one consists of the evaluation of the as-cast microstructure of the alloys, their thermal analysis, and microstructure after solution heat treatment and aging. The second step was focused on the characterization of the alloys' resistance to isothermal and cyclic oxidation at elevated temperatures. The reasonable temperature range for examining such alloys is 700-900°C. The oxide scales formed during isothermal oxidation were analyzed in detail. Based on the oxidation kinetics and characteristics of the oxide scales, appropriate conclusions were drawn. All of the planned experiments allowed for the achievement of the research aims of the thesis.

## 3.2 Alloys processing

The alloys for this PhD project were in-house produced. Polycrystalline cylindrical ingots were cast via the conventional gravity die casting process. The ingots without pouring cups measured approximately 100 mm in length and 18 mm in diameter. First, the correct amount of small pieces of each element was placed in an alumina crucible with a capacity of 0.2 L or in a feeder in the laboratory vacuum induction furnace (Balzers VSG 02). The main feedstock materials were cobalt in the form of pressed powder pellets (min. 99.98% Co), aluminum (grade AW – 99.98% Al), and tungsten in the form of high pressed rods (99.99% W). The reactive elements were introduced to the alloy as very small pieces of lanthanum (99% La), neodymium (99.9% Nd), dysprosium (99.9% Dy), or yttrium (99.9% Y). The casting procedure was as follows:

- placement of Co and W pellet in alumina crucible and Al in vacuum feeder;
- three times flushing with Ar;
- pumping to the pressure of  $10^{-3}$  Tr (~0.13 Pa);
- melting of Co and W;
- addition of Al to molten Co-W alloy;
- addition of previously cleaned reactive elements (if applicable) to molten Co-Al-W alloy;
- filling the chamber with Ar and casting to the graphite mold.

The melting was performed at approximately 1600 °C for about 10 min. The detailed information concerning manufacturing of Co-Al-W alloys via vacuum induction melting (VIM) technique may be found in the already published studies [152, 153]. Besides the ingots dedicated for analysis of as-cast microstructure, the obtained castings were subjected to peeling to remove external surface layer.

Another step in the alloy processing involved solution heat treatment. During this process, the alloy was annealed at 1200°C for 16 h in a tubular furnace, and then quenched in water. Afterwards, the alloys were aged at 900 °C for 100 h. Both heat treatment processes were performed under Ar protection. The high aging time was selected to provide heat treatment of the alloys comparable to that in other publications, where aging time was often 100 h or more. The heat treated alloys were turned in a lathe to obtain  $\varnothing 15$  mm rods. The chemical composition of the finished alloys measured by the XRF method is shown in Table 3.1. The contents of Al, W, and Co are comparable for all alloys.

Table 3.1: Chemical composition of the investigated alloys measured by the XRF method.

Alloy	Nominal composition [at.%]	Chemical composition determined by XRF[at.%]					
		Co	Al	W	RE	Fe	Cu
0RE	Co-9Al-9W	bal.	11.3	8.58	-	-	-
0.1La	Co-9Al-9W-0.1La	bal.	10.28	8.65	0.08 La	0.03	0.06
0.1Nd	Co-9Al-9W-0.1Nd	bal.	10.52	8.62	0.07 Nd	0.01	0.03
0.1Dy	Co-9Al-9W-0.1Dy	bal.	10.76	8.55	0.06 Dy	0.01	-
0.1Y	Co-9Al-9W-0.1Y	bal.	11.01	8.58	0.11 Y	0.01	-

The heat treatment provided the proper microstructure containing the desirable microstructure containing the  $\gamma$ -Co and  $\gamma'$ -Co<sub>3</sub>(Al, W) phases. The experimental XRD pattern and micrographs of the reference 0RE alloy are shown in Figure 3.1.

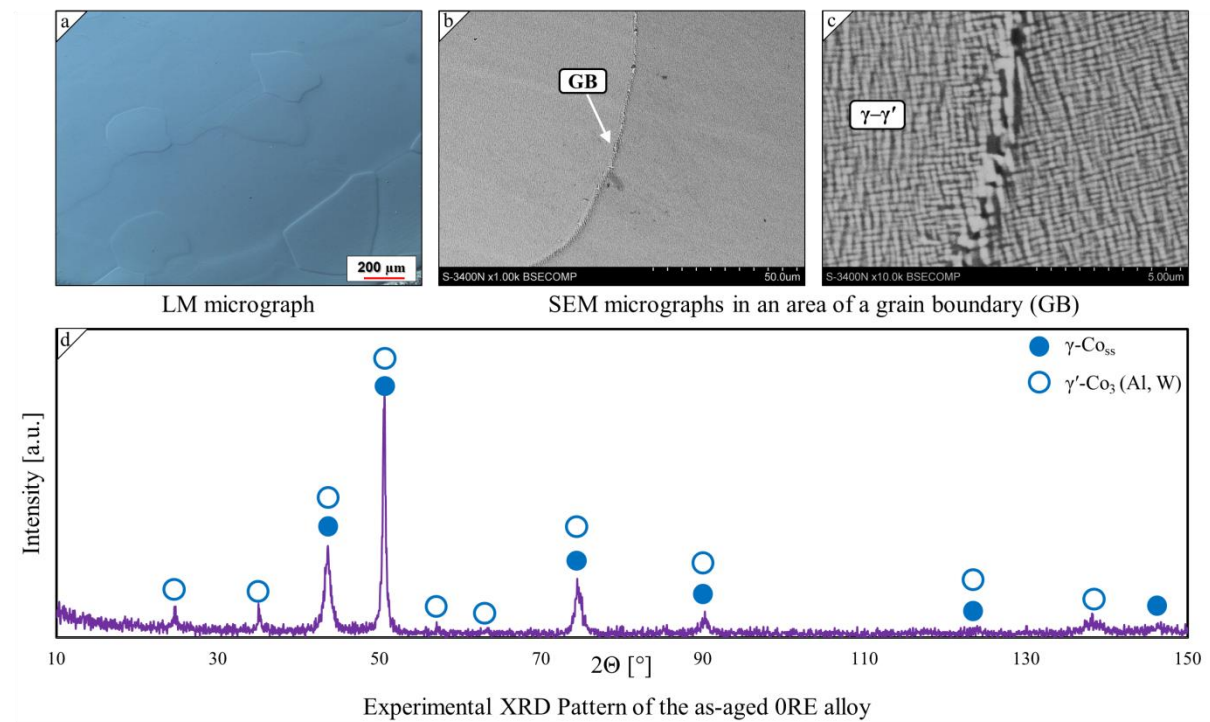


Figure 3.1: The results showing a proper microstructure of the 0RE alloy after heat treatment: a) LM micrograph; b-c) SEM micrographs; d) experimental XRD pattern.

### 3.3 High temperature oxidation

#### 3.3.1 Isothermal oxidation tests

The high temperature isothermal oxidation experiments were carried out on the ORE, 0.1La, 0.1Nd, 0.1Dy and 0.1Y alloys at 700, 800, and 900 °C for 500 h, whereas the selected samples were oxidized also at 1000 °C. The schematic of measurements is presented in Figure 3.2 to illustrate the experimental setup and methodology. To ensure the accuracy and reproducibility of the results, at least three samples were used for each oxidation time (1, 3, 5, 25, 100, 300, and 500 h) at a certain temperature. After removal from the furnace, the samples were placed directly into alumina crucibles and closed to contain any oxidation products in case of oxide spallation. Afterwards, the samples were weighed together with spalled oxides using a laboratory balance with a resolution of 0.1 mg. The mass change ( $\Delta m$  in mg) was then related to the surface area of the sample ( $A$  in  $\text{cm}^2$ ) for further calculations and plotting.

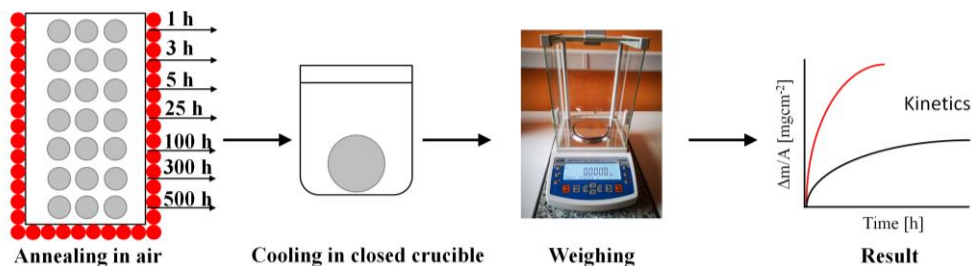


Figure 3.2: Schematic presenting procedure of isothermal oxidation experiments.

#### 3.3.2 Cyclic oxidation tests

The cyclic oxidation experiments were performed at 700, 800, and 900 °C using two regimes: short-term and long-term. The schematic presented in Figure 3.2 can also be useful in describing the long-term cyclic oxidation procedure. The duration of single cycle was 25 h, and the number of cycles was 20. The samples were introduced to a hot furnace, annealed for 25 h, and then cooled to room temperature outside the furnace in a closed crucible. Mass of the sample and mass of the spalled oxides need to be measured separately. The measured specimens were then placed back into the furnace and the oxidation procedure was repeated until the total oxidation time reached 500 h.

The short-term oxidation was performed in an analogous way to the long-term regime; however, the duration of each cycle was 1 h, and the number of cycles was 50. Moreover, the mass of spalled oxidation products was not measured. To ensure the accuracy and reproducibility of the results, at least three samples of each alloy were used for both long-term and short-term cyclic tests.

## **3.4 Characterization techniques**

### **3.4.1 Scanning Electron Microscopy (SEM)**

The microstructure and chemical composition of the oxidized samples were evaluated using scanning electron microscopy (SEM, Hitachi S-3400 N) and energy-dispersive X-ray spectroscopy (EDS, Thermo Noran System Seven). The techniques were utilized for microstructural characterization of the alloys and oxide scales. Imaging was accomplished in backscattered electron mode (BSE). The measurements of chemical composition in micro-areas were performed using standards (Astimex Standards Limited). Furthermore, the electron backscattered diffraction (EBSD, 5 Inca HKL, INCA HKL Nordlys. II (Channel 5)) was used as a supplementary method for phase composition analysis.

### **3.4.2. Scanning Transmission Electron Microscopy (STEM)**

The most detailed studies on the microstructure and oxide scale morphology of the alloys were performed by transmission electron microscopy (TEM). TEM observations were performed on a probe Cs-corrected S/TEM Titan 80–300 FEI microscope, equipped with an EDAX EDS detector. The main imaging methods were high-angle annular dark-field (HAADF) and bright-field (BF). Selected area electron diffraction (SAED) was used to determine the structure of the phase constituents. The studies were performed in the Materials Research Laboratory of the Silesian University of Technology.

### **3.4.3. Differential Scanning Calorimetry (DSC)**

The differential scanning calorimetry (DSC) was used to investigate the temperature at which the order-disorder phase transition occurred in the alloys, as well as other phase transformations. The measurements in the temperature range of 40–1400 °C were performed using the multi-HTC high temperature calorimeter from Setaram. The measurements were performed under the Ar protection; the heating rate was 5 °C min<sup>-1</sup>.

### **3.4.4. Light Microscopy (LM)**

The light microscopy (LM) technique was used for imaging of the alloys and oxide scales. The observations were performed using both the default mode and Nomarski interference contrast with polarized light. The acquisition of micrographs was performed using the Nikon Eclipse MA200 microscope.

### **3.4.5 Hardness**

The hardness of specimens was investigated by the Vickers method. Measurements were performed using the ZWICK ZHV TKV5030 Vickers hardness tester using a test force of

98.07 N. The method was utilized to evaluate hardness distribution across as-cast and as-aged alloys.

### **3.4.6 X-ray diffraction (XRD)**

Phase compositions of alloys were determined using a D8 Advance diffractometer (Bruker AXS, Karlsruhe, Germany) with Cu-K $\alpha$  cathode ( $\lambda = 1.54 \text{ \AA}$ ) operating at a voltage of 40 kV and current of 40 mA. The scan rate was  $0.60^\circ/\text{min}$  with scanning step  $0.02^\circ$  from  $20$  to  $120^\circ$   $2\theta$  was applied. Data collection was performed using a LYNXEYE XE-T linear detector (Bruker AXS, Karlsruhe, Germany), operating in a modified high resolution mode. The high threshold discriminator was maintained at 0.954 V, while the lower threshold discriminator increased from 0.614 to 0.750 V to minimize fluorescence, regarding its presence in the cobalt sample. Additionally, a Ni-filter was applied to remove K $\beta$ . Identification of fitted phases was performed using the DIFFRAC.EVA program and the ICDD PDF-2 database. The research was performed in the Centre of Polymer and Carbon Materials Polish Academy of Sciences.

### **3.4.7 Analysis of chemical composition**

#### Analysis of the average chemical composition

The average compositions for the 0RE, 0.1La, 0.1Nd, 0.1Dy, 0.1Y alloys were determined by X-ray fluorescence spectroscopy (XRF) on a RIGAKU ZSX PRIMUS spectrometer, equipped with a rhodium X-ray tube, with stepless voltage adjustment between 20 and 60 kV, analysing crystals LiF, Ge and a number of synthetics. The compositions were determined at the Institute of Non Ferrous Metals. Moreover, the chemical composition analysis was additionally performed by the EDS method.

#### Elemental analysis of impurities

RE have a high affinity for different impurities present in superalloys, such as sulfur, oxygen, and phosphorus. Therefore, any excess of such elements in an alloy, relative to others, may disturb the comparability of the RE effect on microstructure and oxidation behavior of the alloys. Therefore, the particular analysis of impurities content was performed for all the alloys. The analysis was performed using the elemental analysers LECO ONH836 (for O, N and H) and LECO CS844 (for C and S).

### **3.5. Preparation of samples**

#### Isothermal and cyclic oxidation.

The cylindrical specimens with dimensions of  $\varnothing 15 \times 2$  mm were electro-discharge machined from the aged ingots. The sample surfaces were ground with 1000 mesh SiC paper, polished, and then ultrasonically cleaned in high purity acetone for 15 min. The samples were placed on highly porous ceramic foams inside the furnace to minimize their contact with the crucible and facilitate air access.

#### Microstructural characterization of the alloys.

The same procedure was applied to investigate the microstructure of the alloys, with the exception that the specimens were previously mounted using a hot mounting resin and ultrasound was not used. The same samples were used for hardness testing. The samples for hardness tests and SEM-EDS analysis were not etched, whereas chemical etching was used to reveal dendritic microstructure for the LM observations of as-cast alloys. A solution containing 25 mL H<sub>2</sub>O, 50 mL HCl, 15 g FeCl<sub>3</sub>, 3 g CuCl<sub>2</sub> × NH<sub>4</sub>Cl × H<sub>2</sub>O was used for etching.

#### Microstructural characterization of the oxide scales.

The oxidized samples were hot-mounted before further preparation. Then, the specimens were subjected to grinding to reveal an oxide scale in a cross section perpendicular to the base of the cylinder. Afterwards, the specimens were prepared analogously to the samples for the SEM microstructural characterization of the alloys.

#### Differential Scanning Calorimetry (DSC).

Rectangular specimens (~1 g) were cut from metal slices. Sample surfaces were ground with 1000 mesh SiC paper, polished, and ultrasonically cleaned.

#### Transmission Electron Microscopy.

Thin lamellae for TEM observations were prepared by FIB using a Hitachi FB-2100 device (Tokyo, Japan) with gallium ions.

#### Analysis of chemical composition

The chemical composition of the alloys determined by both XRF and EDS methods was performed on non-etched specimens. The samples for elemental analysis using the LECO devices were prepared using the same procedure as the samples prepared for DSC analysis.

### 3.6 CALPHAD modelling

For the support of the results of thermal analysis and microstructural analysis, the CALPHAD (Calculation of Phase Diagrams) method was employed to investigate the thermodynamic equilibrium of a specific alloy composition. The CALPHAD method is a powerful computational tool that is widely used for predicting the phase behavior of multicomponent systems, such as alloys. It is based on the Gibbs energy formalism, which describes the thermodynamic behavior of a system in terms of the chemical potentials of its components.

The use of CALPHAD was limited to calculating volume fractions of phases as a function of temperature for the alloy composition. The example diagram is shown in Figure 3.3 and denotes a one-axis calculation of volume-fraction of stable phases as a function of temperature for the Co-9Al-9W (at%) alloy. The phase diagrams were determined by Thermo-Calc Software (Thermo-Calc Software AB, Solna, Sweden), using the TCNI10 database. The calculations were performed courtesy of the AGH University of Science and Technology, Faculty of Metals Engineering and Industrial Computer Science.

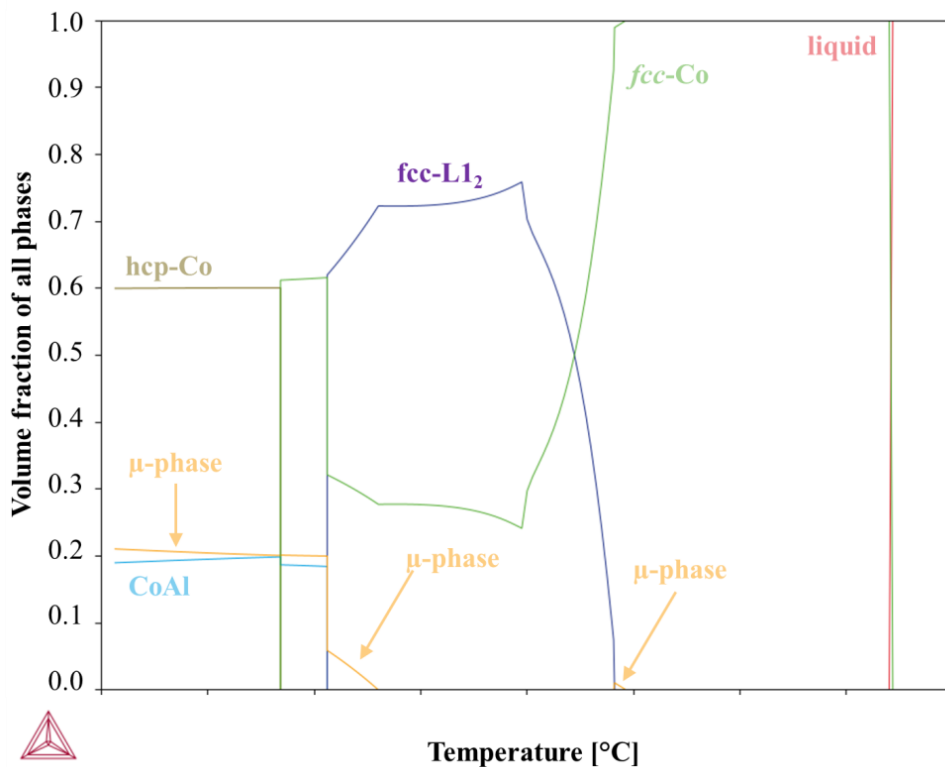


Figure 3.3: Diagram showing predicted proportion of phase as a function of temperature for the Co-9Al-9W (at%) alloy.

## 4. Results

### 4.1 Microstructural and thermal analysis of alloys

#### 4.1.1. Characterization of as-cast microstructure

The aim of the thesis is to investigate the relationship between the addition of RE and the oxidation behavior of Co-based superalloys. To better understand this effect, it is important to know the chemical composition and microstructure of the alloys. The micrographs illustrating the as-cast microstructure of the 0.1La, 0.1Nd, 0.1Dy, and 0.1Y are shown in Figure 4.1. The micrographs revealed dendritic cores (“a”) and interdendritic spaces (“b”) containing small precipitations (“c”) rich in RE. The chemical composition in micro areas corresponding to the RE-rich precipitates can be seen in Table 4.1. The shape of the phases is mostly round, and the precipitates have diameters ranging from 2 to 6  $\mu\text{m}$ . The composition of the phases is characterized by up to 10 at.% of RE, similar or higher amount of Al, and relatively low or undetectable levels of W. What is more, there are substantial local chemical inhomogeneities, which are readily observable in the case of the 0.1La and 0.1Nd, and 0.1Dy alloys. As the oxidation experiments were performed on as-aged alloys, a special focus will be given to the phases containing RE in the heat-treated alloys. The microstructure of the 0RE alloys was the same, although without any RE-containing phases. The detailed information on the microstructure of Co-Al-W alloys manufactured via VIM technique may be found in the already published papers [152, 153].

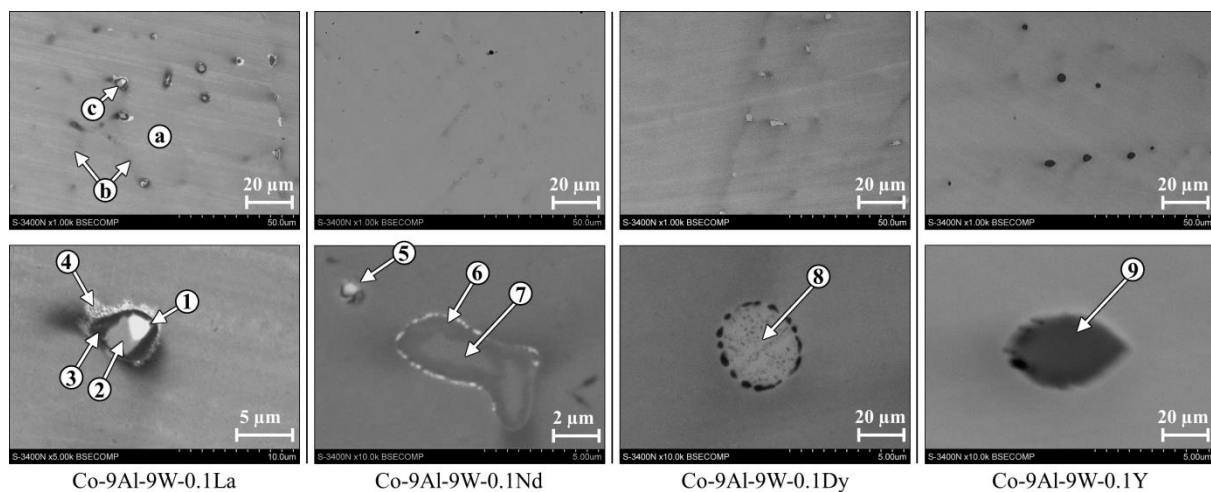


Figure 4.1: SEM micrographs presenting the as-cast microstructure of the 0.1La, 0.1Nd, 0.1Dy, and 0.1Y alloys.

Table 4.1: Chemical composition (EDS) in micro areas corresponding to Y-rich areas of different investigated alloys; the measurement points are indicated in Figure 4.1.

Point	Composition in at.%							
	Al-K	Co-K	La-L	Nd-L	Dy-L	Y-L	W-M	S-K
1	8.2	19.6	69.4	-	-	-	2.8	-
2	17.6	74	7.1	-	-	-	1.3	-
3	15.9	79.5	2.9	-	-	-	1.7	-
4	16	80.9	0.7	-	-	-	2.4	-
5	9.7	16.6	-	36.5	-	-	4	33.2
6	17.5	75.9	4.7	-	-	-	1.9	-
7	17.4	73	7.8	-	-	-	1.8	-
8	9.9	78.1	-	-	9.7	-	2.3	-
9	11.2	77	-	-	-	10.1	1.7	-

Presence of some phases composed of RE and impurities was observed. Such phenomenon is not surprising, since elements such as La, Nd, Dy, and Y are often introduced to alloys for their purification. Taking into account high affinity of RE to elements such as O or S, it is expected that they will first react to form non-metallic inclusions rather than intermetallic phases („C” in Figure 4.1). Therefore, the next step was to analyze the content of impurities in the alloys by elemental analysis methods. The experimentally determined contents of elements such as C, S, O, N, and H are shown in Table 4.2. The level of impurities was very low for all the investigated alloys.

Table 4.2: Results of elemental analysis of C, S, O, N, and H in the investigated alloys.

Alloy	Weight content of C, S, O, N, H [ppm]									
	C		S		O		N		H	
	$\bar{x}$	$\sigma$	$\bar{x}$	$\sigma$	$\bar{x}$	$\sigma$	$\bar{x}$	$\sigma$	$\bar{x}$	$\sigma$
ORE	38.7	4.7	5.5	0.9	6.3	8.1	0.2	0.2	2.1	0.4
0.1La	18.1	8.0	*	-	5.2	3.8	1.0	1.2	2.3	0.9
0.1Nd	46.4	6.9	*	-	5.1	6.2	2.2	2.8	1.7	1.5
0.1Dy	26.5	6.7	3.3	1.4	6.6	1.9	3.4	0.4	1.5	0.6
0.1Y	66.1	6.9	*	-	5.7	8.0	1.1	0.3	1.7	0.3

\* concentration below a detection threshold

Another aspect of the analysis of the castings was how the introduction of RE affected the macrostructure of the alloys. Since reactive elements are often used as grain refiners in alloys, it is worth studying their effect on the  $\gamma$ - $\gamma'$  Co-based superalloys, given the potentially significant impact of grain refinement on oxidation behavior. Figures 4.2a and 4.2b show macrographs and micrographs of the investigated as-cast alloys. The macrographs are shown on the left side, while the right side shows multiple combined micrographs obtained using

LM. The micrographs show the grain structure of the alloys from the middle to the edge of the ingot. Both macro- and micrographs were taken at different heights of the ingot. Zone “A” is connected with the bottom of the ingot, while zone “C” is the upper part, just below the pouring cup. All alloys are characterized by large grain size, typical for Co-based superalloys. Moreover, the alloys exhibited mostly (0RE, 0.1Nd, 0.1Dy) or partially (0.1La, 0.1Y) columnar-crystals microstructure. The primary crystals of the 0.1La were mostly equiaxed (dominance of columnar crystals only in the upper part).

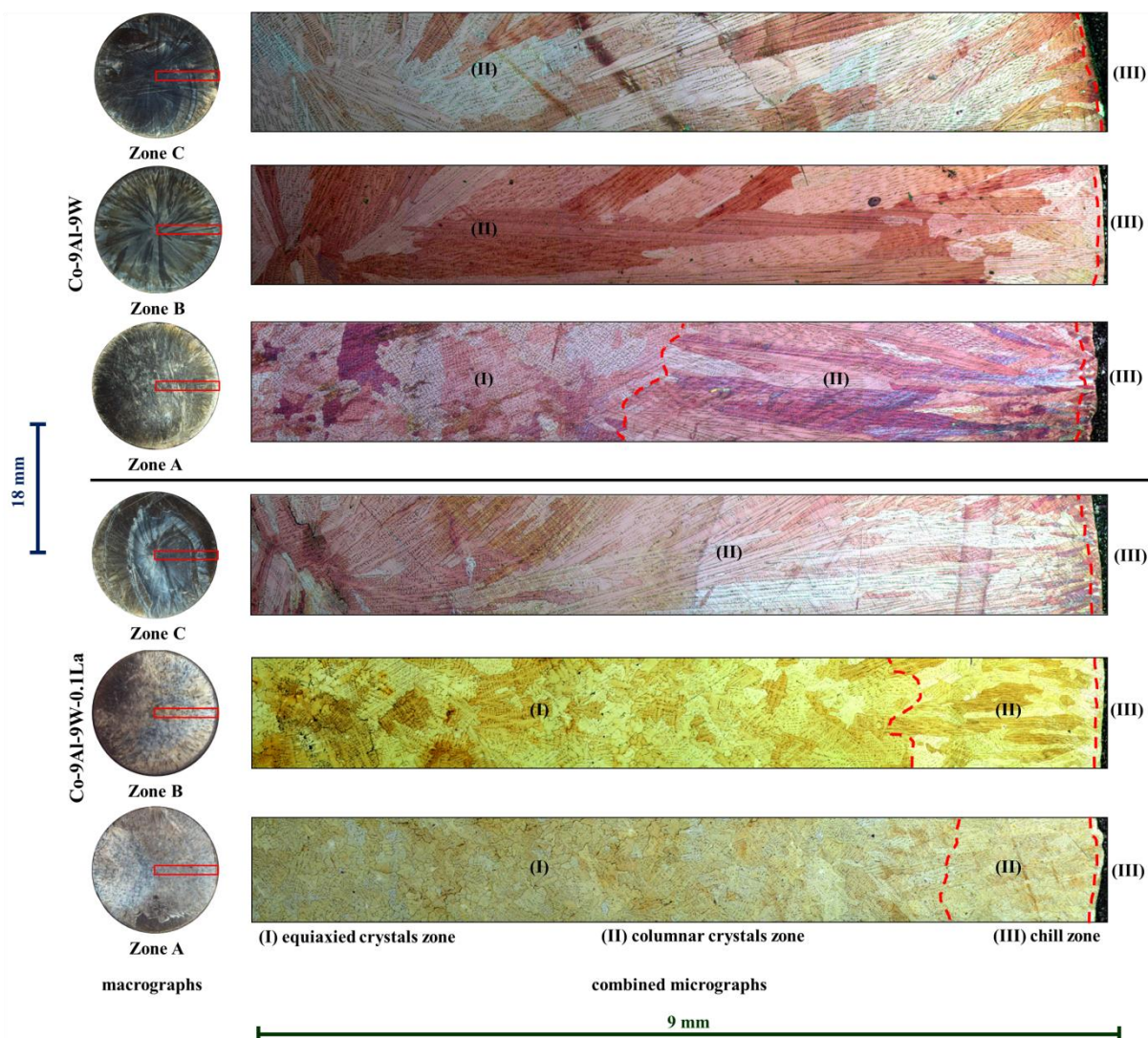


Figure 4.2a: Macrographs and micrographs of the as-cast 0RE and 0.1La alloys.

Introduction of RE caused some microstructural effects in the case of 0.1La and 0.1Y, limiting the content of columnar crystals, however, in general, no considerable grain refinement was observed upon RE-alloying, particularly for the alloys doped with La, Nd, Dy, and Y.

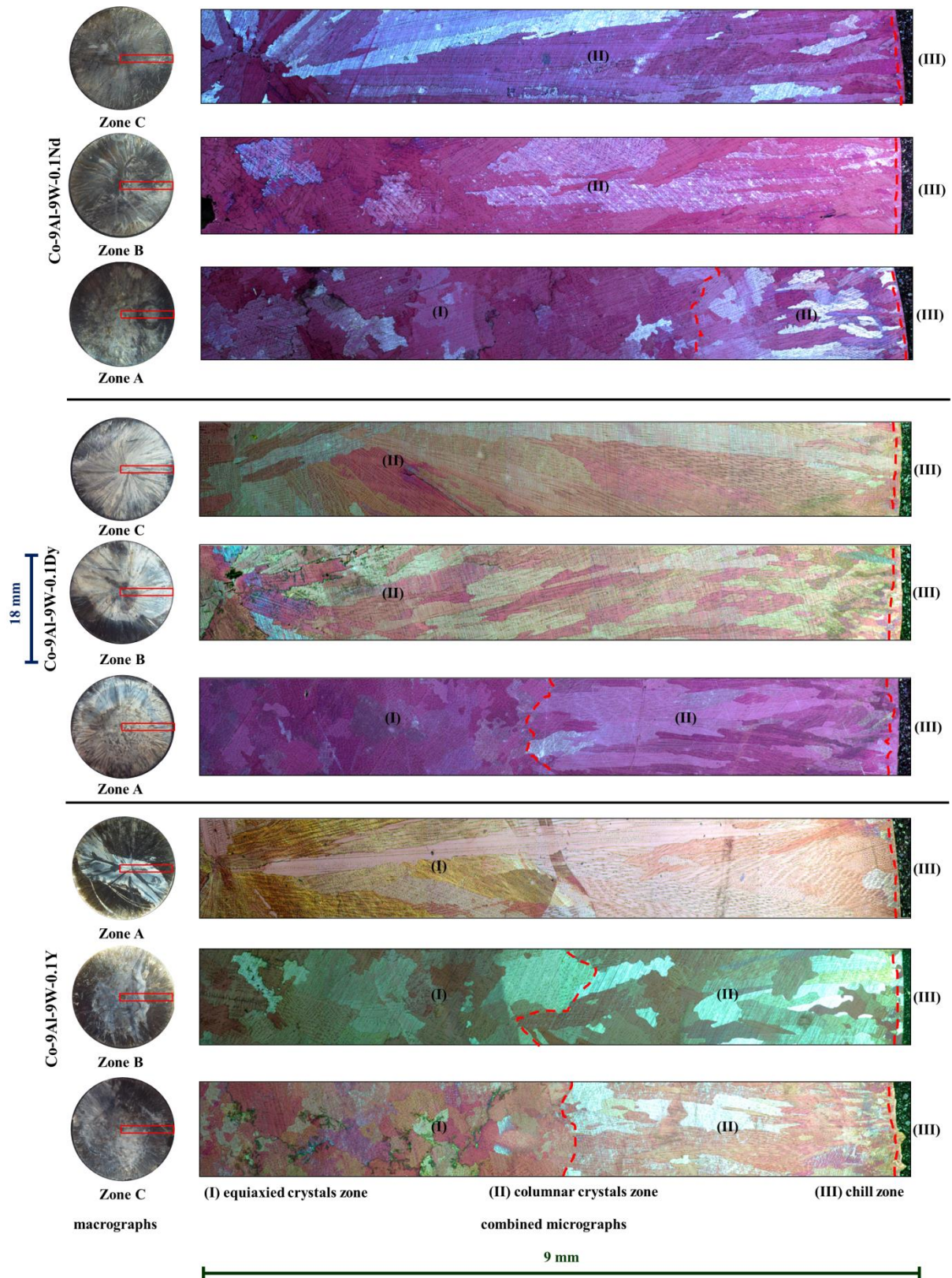


Figure 4.2b: Macrographs and micrographs of the as-cast 0.1Nd, 0.1Dy and 0.1Y alloys.

#### 4.1.2. Characterization of as-aged microstructure

The next part of the microstructural analysis focuses on the alloys following heat treatment. Figure 3.1 in the experimental part showed that the 0RE alloy exhibit the microstructure typical for new Co-based superalloys. These alloys are characterized by a large grain size, as shown in Figure 3.1a, which ranges from several hundred micrometers to even a few millimeters. The microstructure of the alloys is mainly composed of  $\gamma'$ -Co<sub>3</sub>(Al, W) and  $\gamma$ -Co<sub>ss</sub> phases, as evidenced by both SEM micrographs (Figures 3.1b and 3.1c) and the XRD pattern (Figure 3.1d). The microstructure of the other investigated alloys can be described similarly, although they also contain RE-rich phases (Figure 4.3) that require special attention. The phases are located mostly at grain boundaries. The size of the precipitates did not change substantially after heat treatment.

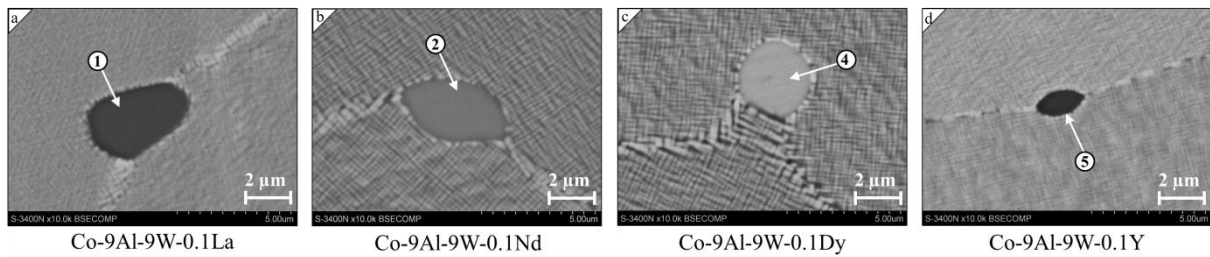


Figure 4.3: SEM micrographs of the as-aged microstructure of the 0.1La, 0.1Nd, 0.1Dy, and 0.1Y alloys.

The average chemical composition measured in the areas of RE-rich phases are shown in Table 4.3 together with the average compositions of the alloys. The analysis in macro areas did not reveal any reactive elements. The RE content in the alloys is presumably too low to be detected via such analysis.

Table 4.3: Average experimental composition of the investigated alloys measured by the EDS method, both in the areas of RE-rich phases and in macro areas.

Alloy	Compositon of RE-rich phase [at. %]				Compositon of the alloy [at. %]		
	Al-K	Co-K	W-M	RE	Al-K	Co-K	W-M
0RE	-	-	-	-	8.2	83.2	8.6
0.1La	11.2	76.3	0.9	11.6 (La-L)	7.9	83.4	8.7
0.1Nd	8.7	80.1	0.9	10.3 (Nd-L)	7.8	83.4	8.8
0.1Dy	6.9	81	2.1	10 (Dy-L)	8.1	83.2	8.7
0.1Y	7.6	81.1	2.3	9 (Y-L)	7.6	83.7	8.7

The phase composition of the as-aged alloys was analyzed by both the XRD and EBSD methods. The contents of the phases were too low to be detected by the XRD. The identification was possible owing to the EBSD method and obtainment of high quality

Kikuchi Patterns. The example patterns are shown in Figure 4.4, which denotes results of the EBSD analysis for Dy-rich phases in as-cast and as-aged state. Table 4.4 shows the results of the identification. The phase composition was analyzed for different precipitates, and mostly more than one type of the phase was recognized. In the case of the 0.1La, two phases were detected. Both were characterized by the structure of  $\text{NaZn}_{13}$  type (cubic, Fm-3c, space group 225.), whereas slightly different lattice parameters. Similar observations were made for the 0.1Nd alloy, where  $\text{Nd}_2\text{Co}_{15}\text{Al}_2$  and  $\text{Nd}_2\text{Co}_{17}$  phases were detected, both with the  $\text{Th}_2\text{Zn}_{17}$  crystal structure (trigonal, R-3m, space group no. 166). In the case of the 0.1Dy and 0.1Y alloys, three types of structures were detected:  $\text{Th}_2\text{Zn}_{17}$  type ( $\text{Dy}_2\text{Co}_{15}\text{Al}_2$ ),  $\text{Th}_2\text{Ni}_{17}$  ( $\text{Y}_2\text{Co}_{15}\text{Al}_2$ ), and  $\text{CaCu}_5$  ( $\text{DyCo}_4\text{Al}$ ,  $\text{YCo}_5$ ). The structure types  $\text{Th}_2\text{Ni}_{17}$  (hexagonal, P6\_3/mmc, 194) and  $\text{CaCu}_5$  (hexagonal, P6/mmm, 191) are similar, however, differ considerably in lattice parameters.

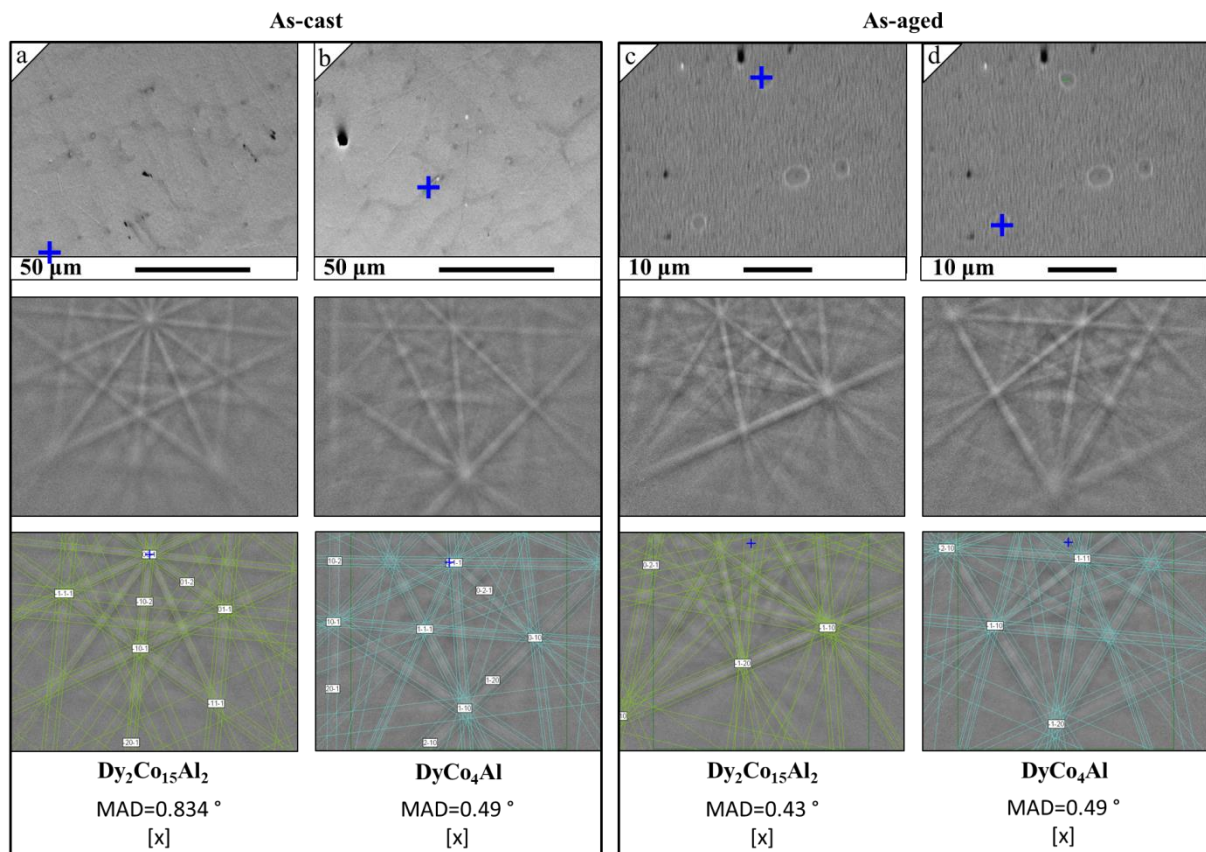


Figure 4.4: The EBSD patterns of Dy-rich phases identified in as-cast state (a, b) and as-aged state (c, d).

Table 4.4: The RE-rich phases identified in the as-aged 0.1La, 0.1Nd, 0.1Dy, and 0.1Y alloys by the EBSD method.

Alloy	Phase 1	MAD [°]	Structure	Phase 2	MAD [°]	Structure
0.1La	LaCo <sub>10.3</sub> Al <sub>2.7</sub>	0.51	NaZn <sub>13</sub>	LaCo <sub>13</sub>	0.51	NaZn <sub>13</sub>
0.1Nd	Nd <sub>2</sub> Co <sub>15</sub> Al <sub>2</sub>	0.81	Th <sub>2</sub> Zn <sub>17</sub>	Nd <sub>2</sub> Co <sub>17</sub>	0.48	Th <sub>2</sub> Zn <sub>17</sub>
0.1Dy	Dy <sub>2</sub> Co <sub>15</sub> Al <sub>2</sub>	0.43	Th <sub>2</sub> Zn <sub>17</sub>	DyCo <sub>4</sub> Al	0.49	CaCu <sub>5</sub>
0.1Y	Y <sub>2</sub> Co <sub>15</sub> Al <sub>2</sub>	0.58	Th <sub>2</sub> Ni <sub>17</sub>	YCo <sub>5</sub>	0.48	CaCu <sub>5</sub>

The identification of the RE-rich phases in the RE-modified Co-Al-W alloys is challenging due to its very low content. In the already published studies, the phases were identified in the case of alloys containing Ce [150] and Y [151], whereas the RE content in the alloys was higher (up to 0.5%). Another obstacle in the identification process is the limited data available on such phases. Therefore, this topic will be covered in more detail in the discussion section. Due to the limitations of the EBSD method, one should approach the obtained results with skepticism and they should be discussed carefully and within a broader context. The detailed analysis supported by the literature data and information obtained for different alloys and by other methods, will be presented in the discussion section.

The LM observations (Figures 4.2a and 4.2b) were also performed for the as-aged alloys. The macrostructure of the alloys after heat treatment was quite similar. Additionally, the characteristic crystal zones were also readily visible in the macrostructure of the samples after early stages of the oxidation at 900 °C.

Besides microstructure and phase composition, another method that can be used to evaluate the effectiveness of a heat treatment is hardness testing. The mean hardness of the as-cast and as-aged alloys is shown in Table 4.5. The approximate 50% increase in hardness was achieved as a result of the solution heat treatment followed by aging, and this increased hardness corresponds to the formation of the  $\gamma$ - $\gamma'$  microstructure. The hardness of the various alloys does not show significant differences. This observation supports the conclusion that the microstructure and chemical composition of the alloys are highly similar. The hardness of the alloys was not found to be significantly influenced by the presence of RE-rich phases. It is anticipated that the effect of RE on the mechanical properties of the  $\gamma$ - $\gamma'$  Co-based alloys will be more apparent at elevated temperatures [145, 147].

Table 4.5: Results of the hardness tests for the as-cast and as-aged alloys.

The alloy condition	Hardness HV10									
	0RE		0.1La		0.1Nd		0.1Dy		0.1Y	
	$\bar{x}$	$\sigma$	$\bar{x}$	$\sigma$	$\bar{x}$	$\sigma$	$\bar{x}$	$\sigma$	$\bar{x}$	$\sigma$
As-cast	267.4	13.1	270.2	4.7	269.1	12.9	262.4	4.8	262.4	7.9
As-aged	407.6	10.5	411.9	3.5	410.8	10.4	410.8	2.5	403.5	9

### 4.1.3 Thermal analysis

The thermal analysis was an interesting aspect of studying the properties of the Co-based superalloys doped with RE. The main aim of the studies was to determine the temperature range of solution heat treatment as well as the aging temperature. The DSC plots of the analyzed alloys are illustrated in Figure 4.5. The heating and cooling plots corresponding to the 0RE alloy may be seen in Figure 4.5a. The DSC curves show solidus (1445 °C) and liquids (1458 °C) temperatures as well as order-disorder ( $\gamma'$  solvus, 968 °C) and disorder-order ( $\gamma'$  precipitation, 975 °C) transitions. Given the solution heat treatment process, the solvus and solidus temperatures play a crucial role as the treatment should be carried out at a temperature above the  $\gamma'$  phase dissolution temperature but below the melting temperature of the alloy. The aging process should be carried out below the solvus temperature. From the analysis of the DSC plot depicted in Figure 4.5b, the solvus temperatures of four alloys (0.1La, 0.1Nd, 0.1Dy, and 0.1Y) was identified. The comparable temperature at which the  $\gamma'$  phases dissolved in these alloys indicates that they have comparable compositions, characterized by similar amounts of Al, W, and Co. Figure 4.5c displays the DSC plots of the 0.1La, 0.1Nd, 0.1Dy, and 0.1Y alloys in the temperature range of 900-1400 °C. Notably, small endothermic effects are observable above 1250 °C, with varying temperatures for different alloys as depicted in Figure 4.5d. It is worth noting that the 0RE alloy does not exhibit these endothermic peaks. Therefore, it is believed that these effects correspond to the melting or dissolution of the RE-rich phases. These thermal events also have exothermic counterparts on the cooling plots, except of the 0.1La alloy. However, to accurately identify the specific phase transformations responsible for these thermal peaks, a thorough analysis and the use of additional methods may be necessary. The characteristic temperatures of peaks as well as the equilibrium temperatures corresponding to crystallization of RE-rich phases (RE-rich phases corresponding to compositions with the lowest content of RE) in binary Co-RE alloys are shown in Table 4.6.

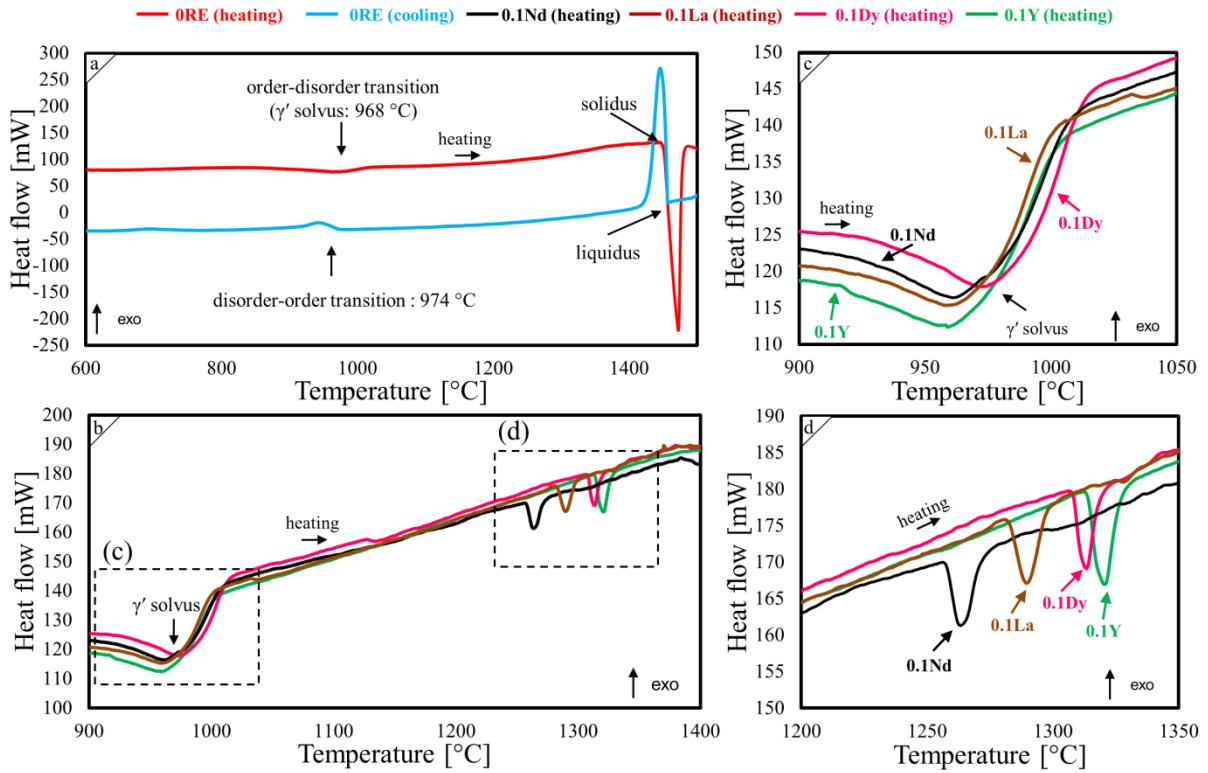


Figure 4.5: The DSC plots: a) heating and cooling plots of the 0RE alloy; b-d) heating plots of the 0.1La, 0.1Nd, 0.1Dy, and 0.1Y alloys.

Table 4.6: Characteristic temperatures connected with melting or crystallization of RE-rich phases determined by DSC analysis (quaternary alloys) or by thermodynamical modeling (binary alloys).

Co-Al-W-RE alloys		0.1La	0.1Nd	0.1Dy	0.1Y	
DSC	heating	$T_{\text{onset}} [^{\circ}]$	1280	1256	1307	1312
		$T_{\text{peak}} [^{\circ}]$	1288	1262	1312	1320
		$T_{\text{offset}} [^{\circ}]$	1298	1272	1321	1330
	cooling	$T_{\text{onset}} [^{\circ}]$		1188	1280	1275
		$T_{\text{peak}} [^{\circ}]$	x	1185	1277	1272
		$T_{\text{offset}} [^{\circ}]$		1175	1268	1262
Binary Co-RE alloys		Co-La [154]	Co-Nd [155]	Co-Dy [156]	Co-Y [157]	
Equilibrium	$T [^{\circ}]$	1185 (LaCo <sub>13</sub> )	1300 (Nd <sub>2</sub> Co <sub>17</sub> )	1360 (Dy <sub>2</sub> Co <sub>17</sub> )	1342 (Y <sub>2</sub> Co <sub>17</sub> )	

The assumption that the observed thermal effects are linked to the local melting of RE-rich phases has significant implications for the design of heat treatment processes and temperature limits of the alloys' application. Therefore, this aspect was extensively investigated through

the analysis of other similar alloys, aided by the CALPHAD method. Due to insufficient information and models related to alloys containing La, Nd, and Dy, a comprehensive analysis was conducted on the alloys containing Y. Thermo-Calc diagrams that demonstrate the predicted proportion of phases based on temperature for Co-9Al-9W-0.5Y, Co-9Al-0.5Y, Co-9W-0.5Y, and Co-0.5Y can be observed in Figure 4.6. The Multi HTC device shows incipient melting effects in the 0.1La, 0.1Nd, 0.1Dy, and 0.1Y alloys, despite the small amount of RE present, which is attributed to the high sensitivity of the device. The alloys did not show any such event when analyzed using other devices and methods, such as the Differential Thermal Analysis. Therefore, these alloys, which contain a higher amount of Y (0.5 at.%), were selected for further analysis of the discussed effect. It is worth noting that these alloys were previously studied in a published paper [151].

The diagrams in Figure 4.6 demonstrate the presence of various phases, with the Y-rich phases and liquid phase being particularly relevant for this analysis. For the alloys Co-0.5Y, Co-9Al-0.5Y, and Co-9W-0.5Y, the temperature at which  $Y_2Co_{17}$  forms (liquid+fcc-Co $\rightarrow$  $Y_2Co_{17}$ ) may indicate the solidus temperature, since crystallization finishes at this temperature. This analysis was focused on alloys containing Y due to the lack of information and models available for alloys containing La, Nd, and Dy. The Co-9Al-0.5Y, Co-9W-0.5Y, and Co-0.5Y alloys have solidus temperatures of 1235, 1324, and 1342 °C, respectively. In the case of the Co-9Al-9W-0.5Y alloy,  $YCo_5$  forms at 1179 °C, and  $Y_2Co_{17}$  forms at a lower temperature (1106 °C) at the expense of  $YCo_5$ . A similar behavior was observed in the case of Co-9Al-9W-0.1Y, where  $YCo_5$  is stable in the temperature range of 1120-1178 °C. The content of both  $YCo_5$  and  $Y_2Co_{17}$  is lower in this alloy than in Co-9Al-9W-0.5Y.

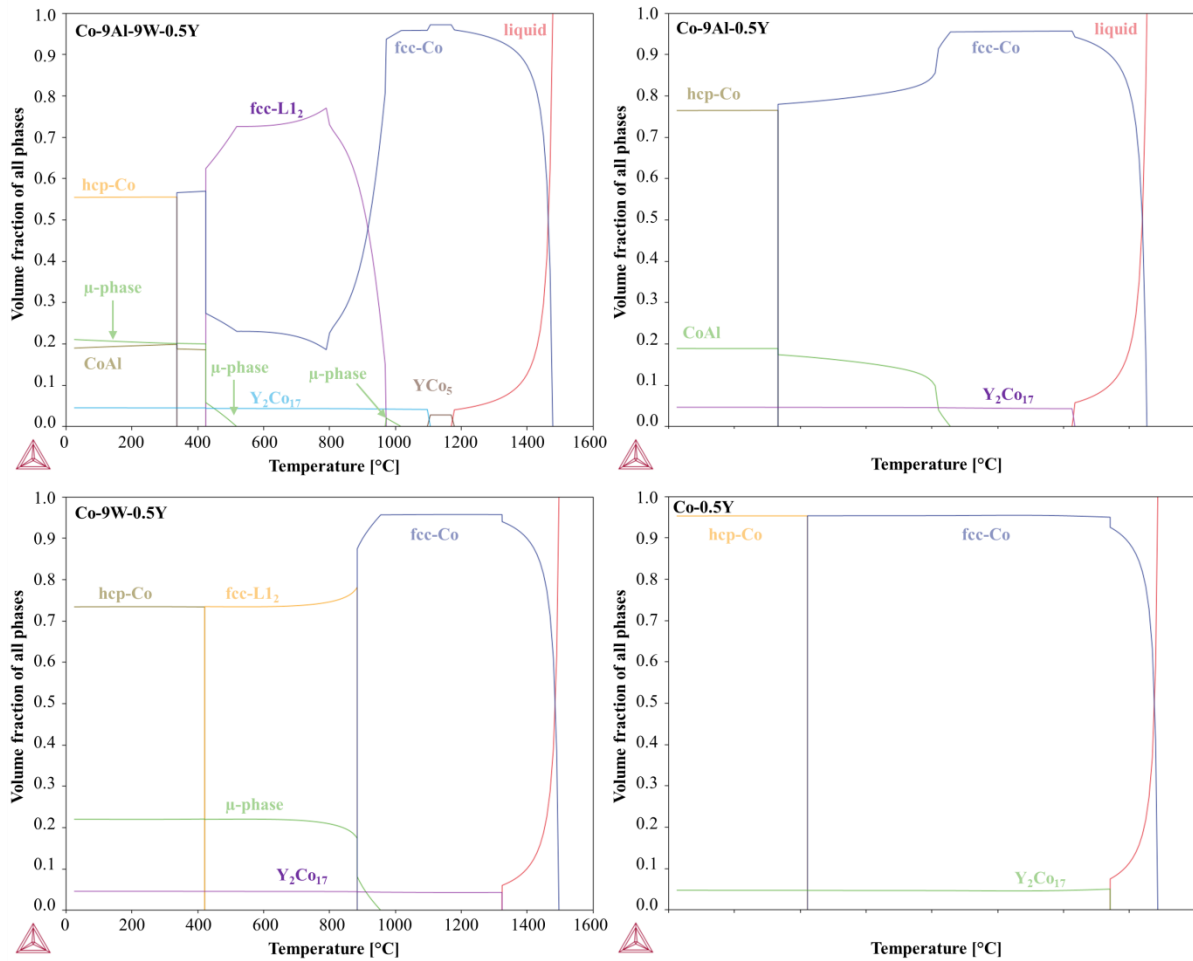


Figure 4.6: Thermo-Calc diagrams showing predicted proportion of phase as a function of temperature for the Co-9Al-9W-0.5Y, Co-9Al-0.5Y, Co-9W-0.5Y, and Co-0.5Y.

The addition of Al, W, or both elements to the Co-Y alloy is seen to have an impact on the formation temperatures of fcc-Co and Y-Co phases, as shown in Figure 4.7a. The plot illustrates that the content of Al, W, and both elements in the Co-Al-W-Y alloys influences these changes. While the introduction of W to the Co-Y alloy raises the liquidus temperature, it has only a slight effect on the solidus temperature. The addition of Al, W, or both to the Co-Y alloy has a noticeable effect on the temperatures of formation of the fcc-Co and Y-Co phases, as shown in Figure 4.7a. Introducing W to the Co-Y alloy increases the liquidus temperature but slightly decreases the solidus temperature. Adding Al to the Co-Y alloy has the opposite effect, slightly decreasing the liquidus but substantially lowering the solidus. When both Al and W are added, both liquidus and solidus temperatures decrease more than in the case of Co-Al-Y alloys alone. As a result, the incipient melting temperature, which can also be considered as the solidus temperature, can vary substantially depending on the alloying elements in Co-based alloys containing Y. The trends predicted by the model were

experimentally studied, and Figure 4.7b shows the corresponding DSC plots for the Co-9Al-9W-0.1Y, Co-9Al-9W-0.5Y, Co-9Al-0.5Y, Co-9W-0.5Y, and Co-0.5Y alloys.

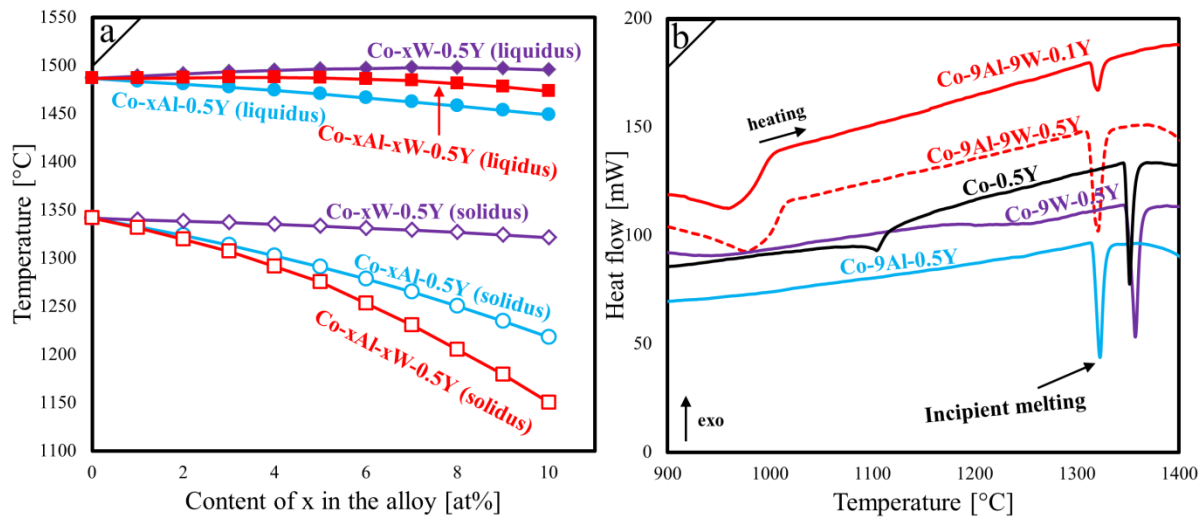


Figure 4.7: The diagrams showing: a) liquidus and solidus temperatures plotted versus content of x in the alloys Co-xW-0.5Y, Co-xAl-0.5Y and Co-xAl-Xw-0.5Y; b) DSC plots of the Co-9Al-9W-0.1Y (0.1Y), Co-9Al-9W-0.5Y, Co-9W-0.5Y, and Co-0.5Y alloys.

The Co-9Al-9W-0.1Y and Co-9Al-9W-0.5Y alloys exhibit thermal effects associated with both order-disorder transition and incipient melting at similar temperatures (with a peak temperature at approximately 1318 °C). However, the incipient melting effect is significantly more prominent in the alloys with higher Y content. On the other hand, the incipient melting peaks observed in the Co-0.5Y and Co-9W-0.5Y alloys are present at substantially higher temperatures, with peak temperatures of 1351 °C and 1357 °C, respectively. The incipient melting peak temperature for the Co-9Al-0.5Y alloy is observed to be 1321 °C, which differs from the temperature predicted by the model (Figure 4.7a). It is important to note that the characteristic temperatures determined by the Thermocalc are based on equilibrium conditions and may not fully represent actual behavior. Additionally, models generated for multicomponent alloys may be unreliable. Nevertheless, both the models (Figure 4.7a) and the DSC plots (Figure 4.7b) suggest that introduction of Al or both Al and W may decrease temperature at which there is no liquid in the alloy containing yttrium. Additionally, studies were also conducted for the alloys containing Ni [158]. The Co-20Ni-9Al-9W-0.5Y alloy exhibited an even lower peak temperature (1286 °C) for the incipient melting effect compared to the Co-9Al-9W-0.5Y alloy. These results suggest that the endothermic thermal effects observed in Figure 4.5d are likely connected to local incipient melting of the RE-rich phases. Although melting processes may occur locally for alloys with low RE-content, it is important to avoid heating the alloy to such temperatures during operation, hence the effect limits the

maximum operating temperature of an alloy. To address this issue, a solution heat treatment was performed at a temperature lower than the incipient melting temperature of the 0.1Nd alloy, which is approximately 1250 °C. Since the solvus temperature for the studied alloys (0RE, 0.1La, 0.1Nd, 0.1Dy, and 0.1Y) was roughly 960 °C, the aging temperature of approximately 900 °C, which is about 60 °C lower, was selected.

While the primary objective of the thermal analysis was to aid in the heat treatment design, an additional goal was to assess the impact of RE-doping on the DSC plots of the alloys. The results showed that introduction of RE may substantially decrease solidus temperature of the alloys, and this change is sensitive to the overall composition of an alloy. The available data on the effects of RE-doping in Co-based alloys, particularly in  $\gamma$ - $\gamma'$  Co-based superalloys, is almost non-existent. Thus, the discussion section will expand on this topic.

### 4.3 High temperature isothermal oxidation behavior of alloys

Figure 4.8 shows the isothermal oxidation behavior of the alloys at 700, 800, and 900 °C in air. Long-term measurement were carried out for 500 h and representative oxidation curves are illustrated. Both the specific mass change  $\Delta m/A$  and its square  $(\Delta m/A)^2$  are plotted against oxidation time. The values of  $\Delta m/A$  are plotted with the standard deviation as error bars. The shape of the plots imply parabolic growth of the scale with time for all alloys at temperature range 700-900 °C. The shape of the plots implies parabolic growth of the scale with the time for all alloys in the temperature range of 700-900 °C. The experimental data was utilized to determine the parabolic rate constant ( $k_p$ ) utilizing equation (2.6).

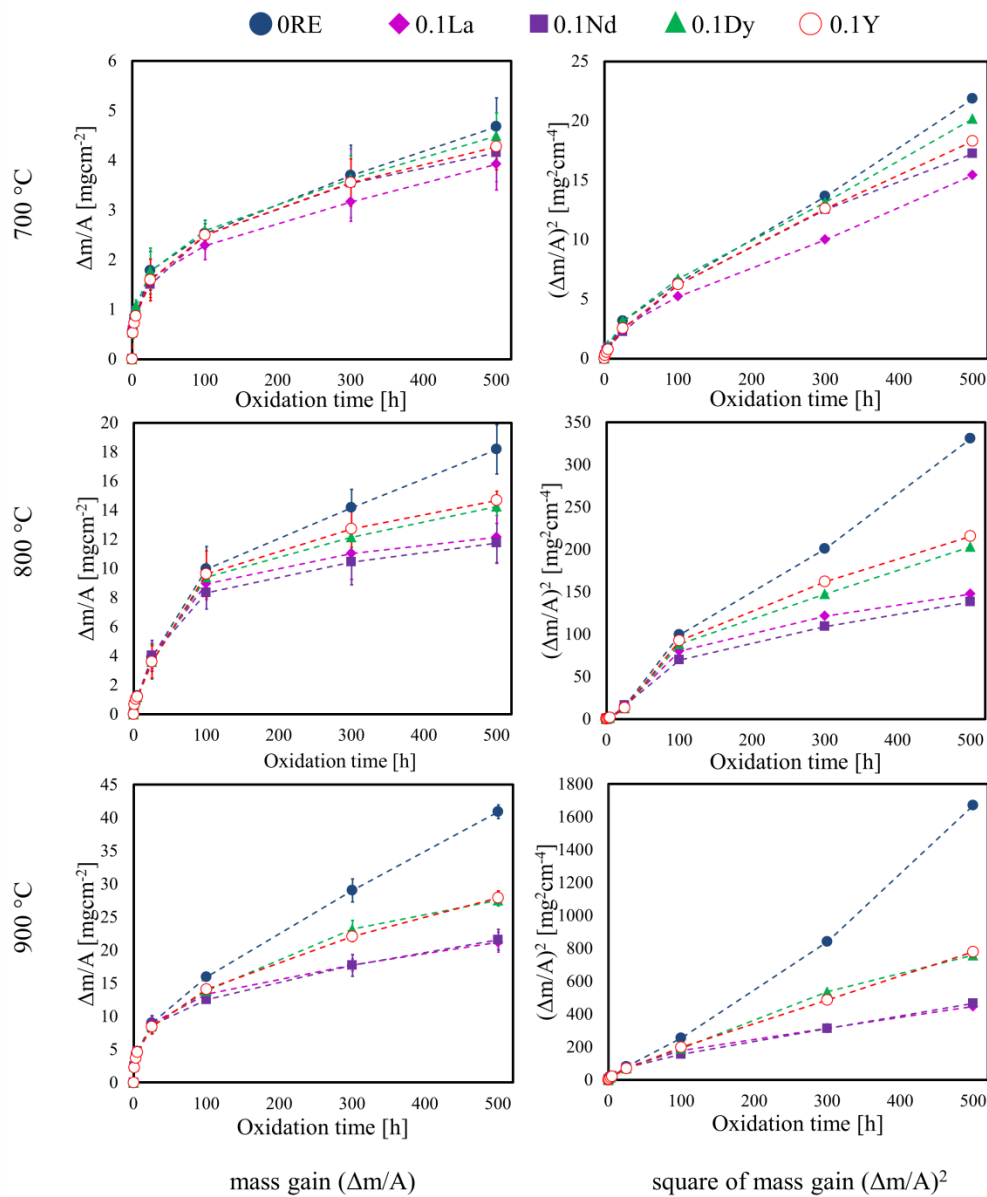


Figure 4.8: Isothermal oxidation kinetics of the alloys oxidized at 700, 800, 900°C for 500 h.

The parabolic rate constants ( $k_p$  in  $\text{g}^2\text{cm}^{-4}\text{s}^{-1}$ ) for the all investigated alloys are presented in Table 4.7. The isothermal oxidation experiments revealed that the oxidation rate of the base alloy was higher than that of the RE-modified alloys, with the difference being most pronounced at 900 °C. The alloys with the lowest values of  $k_p$  were found to be the 0.1La and 0.1Nd alloys, suggesting their superior oxidation resistance relative to the other investigated materials. Additional isothermal oxidation measurements at 1000 °C were conducted for two extreme alloys in view of oxidation kinetics, namely 0RE and 0.1Nd. The determined values of  $k_p$  for the 0RE and 0.1Nd alloys are  $4.95 \times 10^{-9}$  and  $1.59 \times 10^{-9} \text{g}^2\text{cm}^{-4}\text{s}^{-1}$ , respectively. The relationship between oxidation temperature and the differences in  $k_p$  values between the RE-modified alloys and the 0RE alloy show an increasing trend as the oxidation temperature increases.

Table 4.7: Calculated  $k_p$  values for the 0RE, 0.1La, 0.1Nd, 0.1Dy, and 0.1Y alloys at temperatures ranging from 700 °C to 900 °C.

Alloy	700 °C		800 °C		900 °C	
	R	$k_p$ [ $\text{g}^2\text{cm}^{-4}\text{s}^{-1}$ ]	R	$k_p$ [ $\text{g}^2\text{cm}^{-4}\text{s}^{-1}$ ]	R	$k_p$ [ $\text{g}^2\text{cm}^{-4}\text{s}^{-1}$ ]
0RE	0.99	$1.2 \times 10^{-11}$	0.99	$1.8 \times 10^{-10}$	0.99	$8.9 \times 10^{-10}$
0.1La	0.98	$8.3 \times 10^{-12}$	0.90	$8.7 \times 10^{-11}$	0.96	$2.5 \times 10^{-10}$
0.1Nd	0.97	$9.6 \times 10^{-12}$	0.92	$8.0 \times 10^{-11}$	0.98	$2.5 \times 10^{-10}$
0.1Dy	0.98	$1.1 \times 10^{-11}$	0.95	$1.2 \times 10^{-10}$	0.99	$4.3 \times 10^{-10}$
0.1Y	0.98	$1.0 \times 10^{-11}$	0.95	$1.3 \times 10^{-10}$	0.99	$4.3 \times 10^{-10}$

Since the oxidation is a thermally activated process, The constant  $k$  is related to the oxidation activation energy, which can be expressed by the Arrhenius equation:

$$k_p = k_0 e^{-\frac{Q}{RT}} \quad (2.6)$$

where  $k_p$  is the oxidation rate constant,  $k_0$  is a constant for equation,  $Q$  is the apparent activation energy [ $\text{Jmol}^{-1}$ ],  $R$  is the molar gas constant ( $8.3144 \text{Jmol}^{-1}\text{K}^{-1}$ ), and  $T$  is the absolute temperature [K]. The Arrhenius plots between  $\ln k(T)$  and  $1/T$  for the 0RE and 0.1Nd are shown in Figure 4.9. The apparent activation energy was calculated from the slopes of straight lines and found to be 203.7 and 169.4 kJ/mol respectively. The analogous calculations were performed for all the investigated alloys in the temperature range 700-900 °C (Table 4.8).

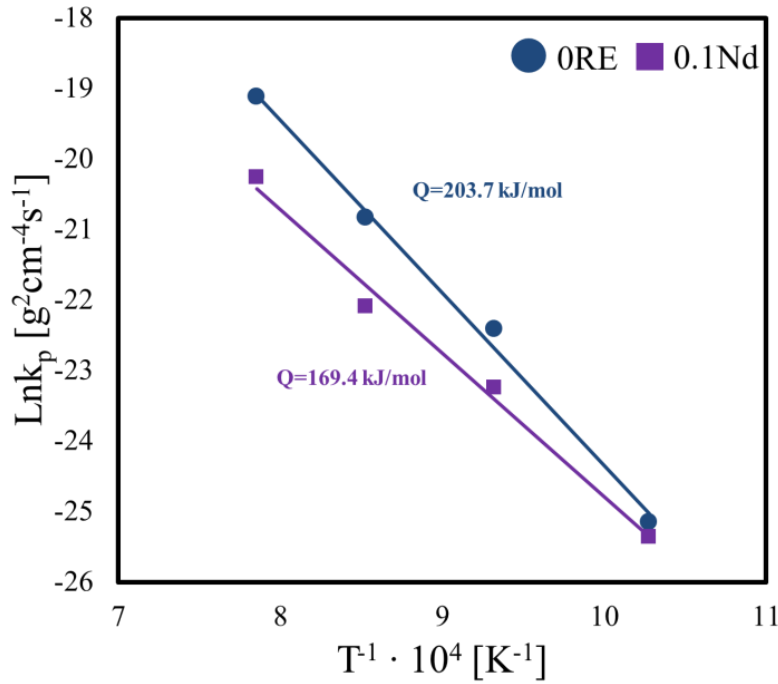


Figure 4.9: Arrhenius plots of  $\ln k_p(T)$  vs  $1/T$  yielding activation energy for oxidation of the 0RE and 0.1Nd alloys.

Table 4.8: Calculated  $Q$  values for the 0RE, 0.1La, 0.1Nd, 0.1Dy, and 0.1Y alloys at temperatures ranging from 700 °C to 900 °C and from 700 to 1000 °C.

Temperature range	Apparent activation energy $Q$ [ $\text{kJmol}^{-1}$ ]				
	0RE	0.1La	0.1Nd	0.1Dy	0.1Y
700-900 °C	206.3	162.4	156.2	175.4	179.1
700-1000 °C	203.7	-	169.4	-	-

The reference alloy 0RE exhibit the highest activation energy and  $k_p$  values among the all investigated alloys in the temperature range 700-900 °C. These results can be reflected not only in oxide scale thickness, but also in the oxide scale structure. Figure 4.10 shows SEM micrographs of the 0RE and 0.1Nd alloys oxidized at 900 °C for 300 h. In both cases, the oxide scale contain three layers: outer oxide layer (OOL), inner oxide layer (IOL) and internal precipitation region (IPR). the IOL and IPR together constitute the internal oxidation zone (IOZ) of the alloy. The nomenclature for these oxidation zones was inspired by previous references [94, 96]. The IPRs of the alloys have different ratio of thickness related to the overall oxide zone thickness. Furthermore, they contain different amount of dark phases (marked by white arrows) which are believed to be alumina. Since at lower temperatures, almost no oxide precipitates below IOL can be found, for the purpose of the thesis, the IPR will be also marked as the  $\gamma'$ -free zone ( $\gamma'$ -free).

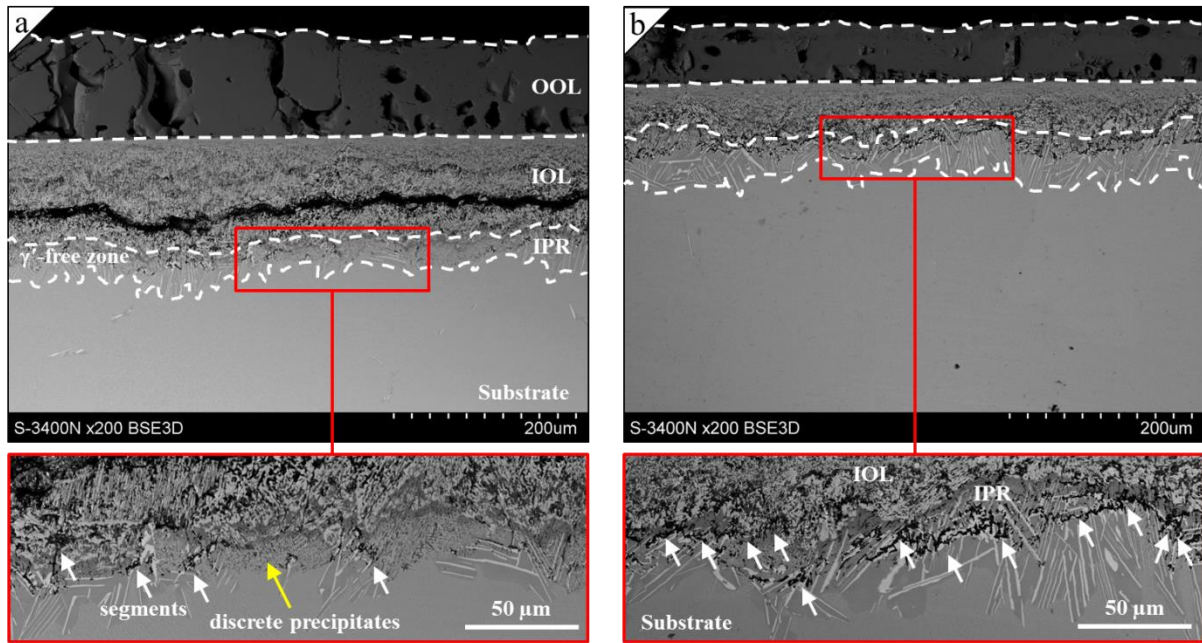


Figure 4.10: SEM micrographs (BSE) of the oxide layers formed on the investigated alloys after oxidation at 900 °C for 300 h: a) 0RE alloy; b) 0.1Nd alloy.

To acquire more information about isothermal oxidation behavior of the studied alloys, the thickness of the oxide scales after 500 h of oxidation was measured (Table 4.9). The table shows thickness of individual layers (OOL, IOL, and  $\gamma'$ -free). Furthermore, for the 0RE and 0.1Nd alloys, the oxide scale thickness was also measured after 1, 3, 5, 25, 100, and 300 h of oxidation at 800 and 900 °C.

To determine the thickness of each layer, five measurements were taken from representative areas of the cross-sections under investigation, and the mean values were calculated. The measurements were done on base surfaces of cylindrical samples. These mean values were then graphed, and the standard deviation was included as error bars to indicate the level of variability in the data.

The oxide layer thickness versus oxidation time plots are shown in Figure 4.11. The oxide layer of the 0RE alloy after oxidation at 900 °C for 500 h was not measured due to severe oxide spallation. The substantial oxide peeling was noticeable also in samples oxidized for 300 h, therefore, hence the number of areas able to be measured was limited.

Table 4.9: Mean oxide layer thicknesses and their standard deviations determined for the investigated alloys after oxidation for 500 h at 700, 800, and 900 °C.

Layer	Mean oxide layer thickness [ $\mu\text{m}$ ]										
	0RE		0.1La		0.1Nd		0.1Dy		0.1Y		
	$\bar{x}$	$\sigma$	$\bar{x}$	$\sigma$	$\bar{x}$	$\sigma$	$\bar{x}$	$\sigma$	$\bar{x}$	$\sigma$	
700 °C	OOL	17.9	1.4	16.3	1.7	16.3	1.9	17.2	2.3	16.5	1.7
	IOL	18.6	2.4	14.3	4.2	13.7	2.9	16.1	4.1	14.3	3.8
	$\gamma'$ -free	0.6	1.7	4.6	2.4	4.1	2.8	1.5	2.0	3.3	3.3
	total	37.1	2.7	35.2	4.3	34.1	4.4	34.8	3.5	34.1	3.1
800 °C	OOL	61.8	6.9	32.3	5.0	26.9	3.7	35.7	7.4	40.4	3.9
	IOL	50.8	21.7	26.4	10.0	20.0	12.0	34.6	19.0	39.2	12.7
	$\gamma'$ -free	21.8	12.8	17.6	6.1	13.0	6.0	17.7	9.7	18.5	9.3
	total	134.4	17.2	76.3	13.4	59.9	15.2	88.0	22.8	98.1	16.1
900 °C	OOL			73.5	5.2	76.3	6.8	111.9	6.7	102.9	6.1
	IOL			68.1	9.7	71.0	20.8	114.0	11.9	99.0	10.6
	$\gamma'$ -free			51.3	11.2	66.0	22.8	36.8	11.2	42.4	10.5
	total			192.9	15.9	213.4	21.2	262.7	12.7	244.2	13.8

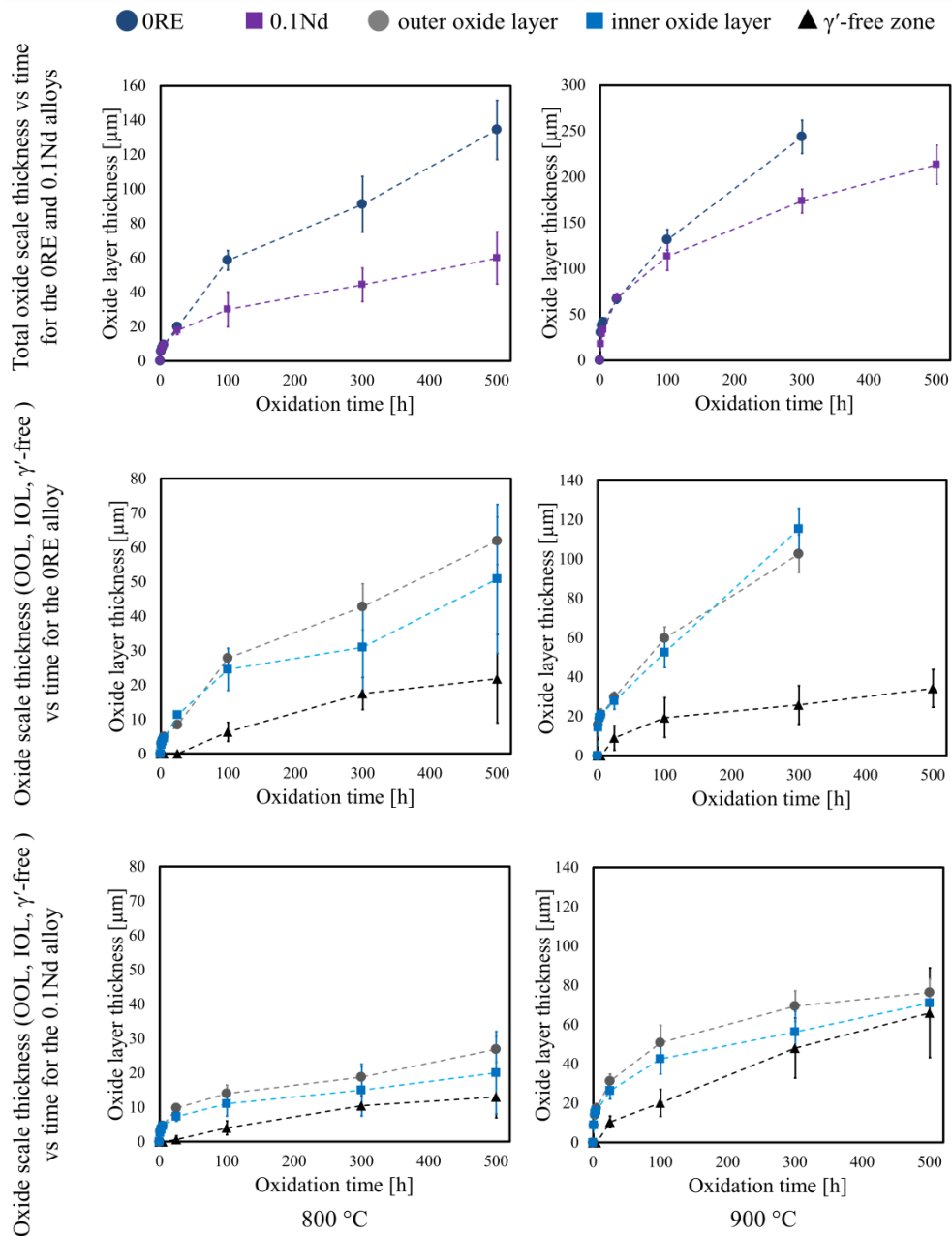


Figure 4.11: Oxide layer thickness vs oxidation time plots for the 0RE and 0.1Nd oxidized at 800 and 900 °C up to 500 h.

The plots of total oxide scale thickness versus time (Figure 4.11) indicate that the 0RE and 0.1Nd alloys follow a parabolic rate law. The main difference between the 0RE and 0.1Nd alloys, except for the oxide layer thickness, is a growth rate of the internal oxidation zone. Besides the oxide layer thickness, the growth rate of the internal oxidation zone is the main difference between the 0RE and 0.1Nd alloys. In comparison to the OOL and IOL, the  $\gamma'$ -free zone of the 0RE alloy is substantially thinner, and this difference becomes more pronounced as oxidation time increases. Conversely, the opposite phenomenon may be observed in the case of 0.1Nd. This will be discussed further in another part of the dissertation.

## 4.4 High temperature cyclic oxidation behavior of alloys

Another aspect of the characterization of the oxidation resistance of the alloys involved evaluating their resistance under thermal cyclic conditions. The evaluations were carried out using both long-term tests (single thermal cycle equal to 25 h) and short-term tests (single thermal cycle equal to 1 h) at 700, 800, and 900 °C. The plots in Figures 4.12, 4.13, and 4.14 show the specific mass change ( $\Delta m/A$ ) of the specimens, which were measured by weighing both the specimens and the spalled oxides after long-term thermal cycles.

The results of long-term cyclic oxidation measurements at 700 °C can be seen in Figure 4.12. The 0.1La and 0.1Nd alloys exhibit a lack of or very limited oxide scale spallation, whereas the 0.1Dy and 0.1Y alloys suffered from oxide peeling in the first experiment. In the case of the base alloy, oxide spallation was noticeable in all experiments, especially I and II.

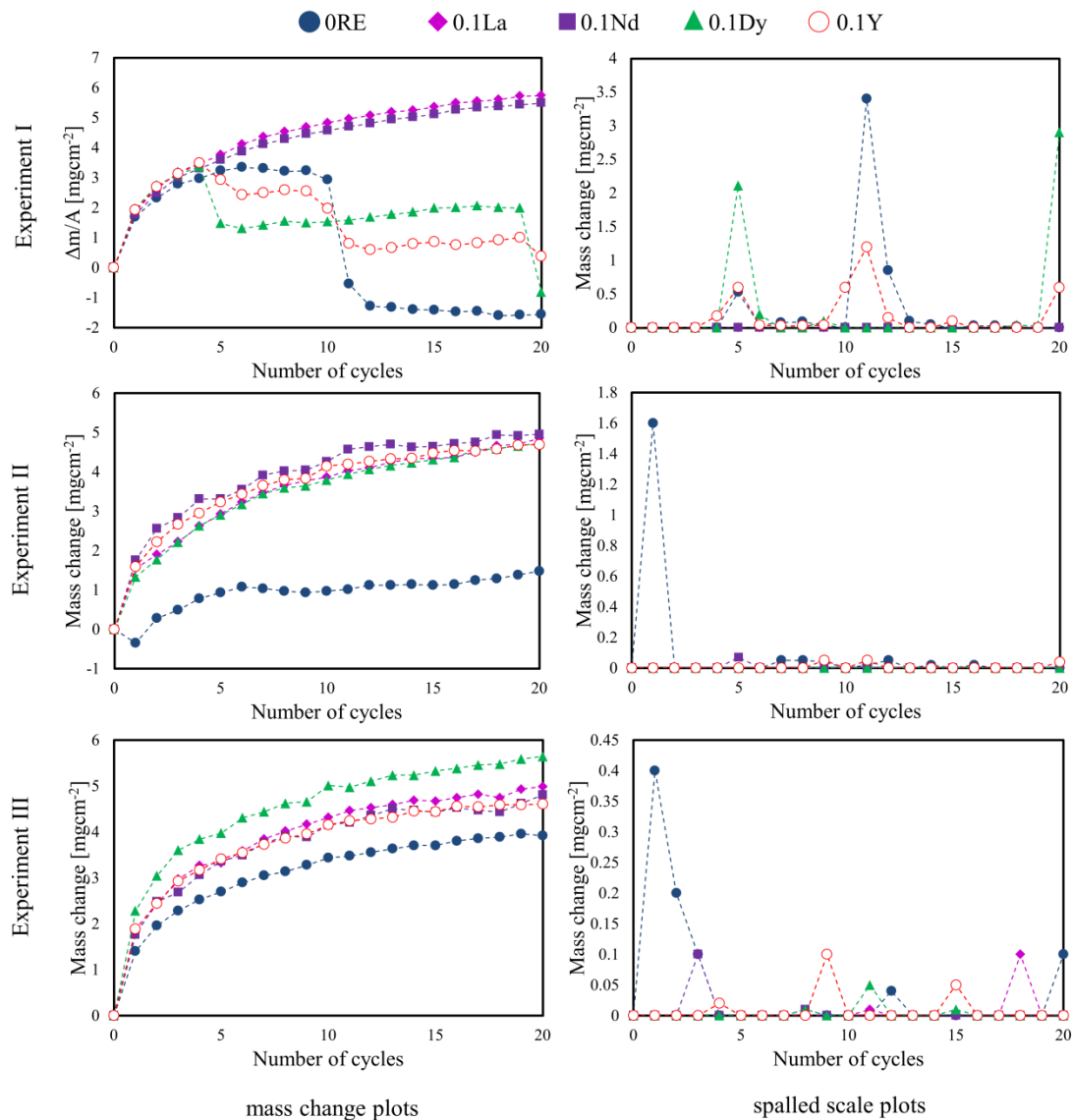


Figure 4.12: Long-term cyclic oxidation plots of the alloys oxidized at 700 °C.

Figure 4.13 shows the results of long-term cyclic oxidation tests at 800 °C. Although the 0RE alloy exhibited the most intense spallation, none of the attempts resulted in a complete loss of material, as indicated by the  $\Delta m/A$  measurements. The other alloys exhibited slight oxide spallation during thermal cycling.

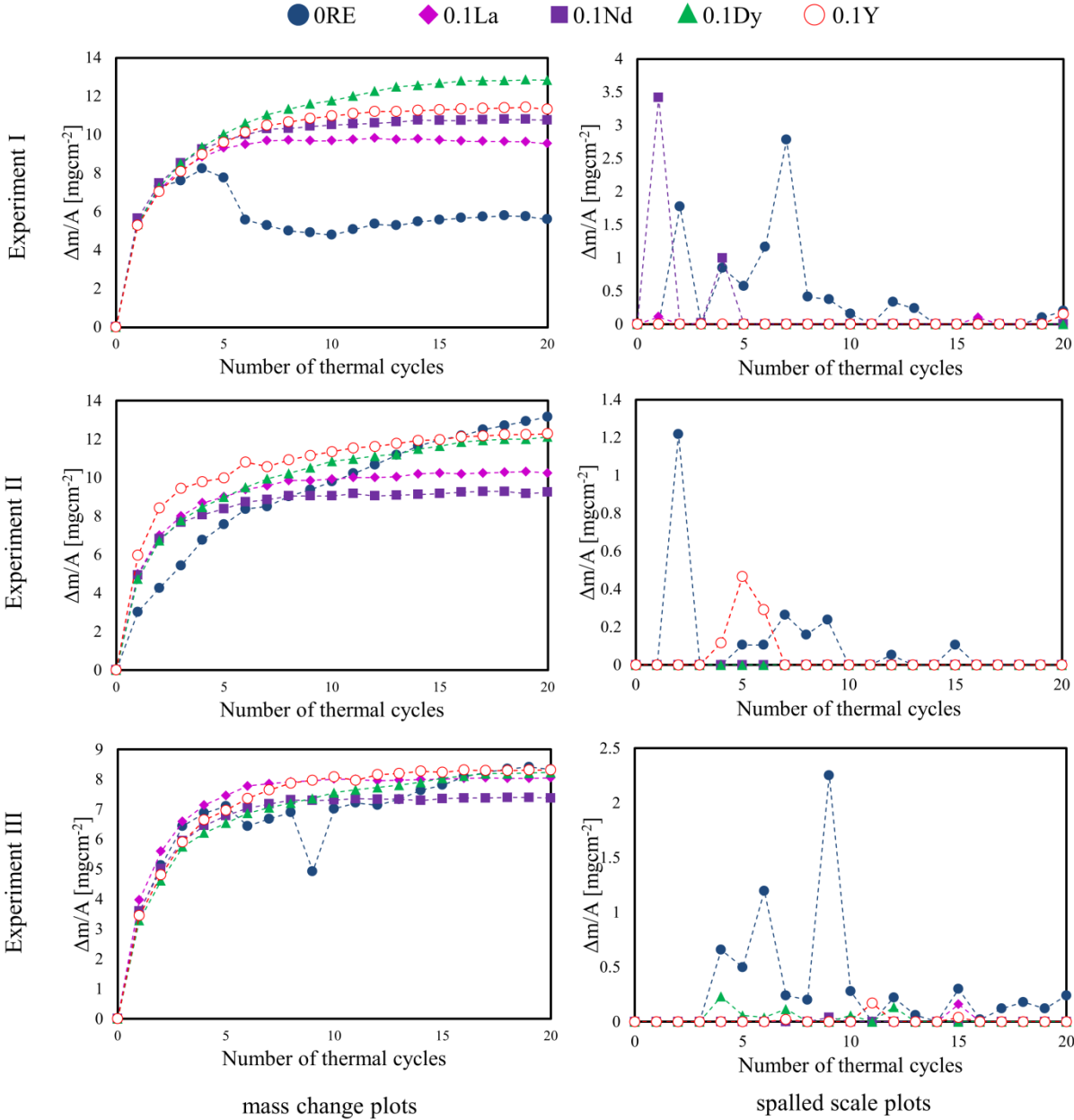


Figure 4.13: Long-term cyclic oxidation plots of the alloys oxidized at 800 °C.

The results of the long-term cyclic oxidation of the alloys at 900 °C are shown in Figure 4.14. The plots clearly show very low resistance of the 0RE alloy to thermal cycling at 900 °C. In the experiments I, II, and III, the 0RE alloy exhibited a total  $\Delta m/A$  of ca. -290, -408, and -280  $\text{mgcm}^{-2}$ , respectively. Among the alloys tested, 0.1La and 0.1Nd showed the best cyclic oxidation resistance, with almost no oxide peeling observed during thermal cycling.

The 0.1Y alloy showed significant spallation in Experiment I and slight spallation in the other experiments, whereas the 0.1Dy alloy exhibited slight spallation in Experiments I and II, but noticeable spallation in Experiment III.

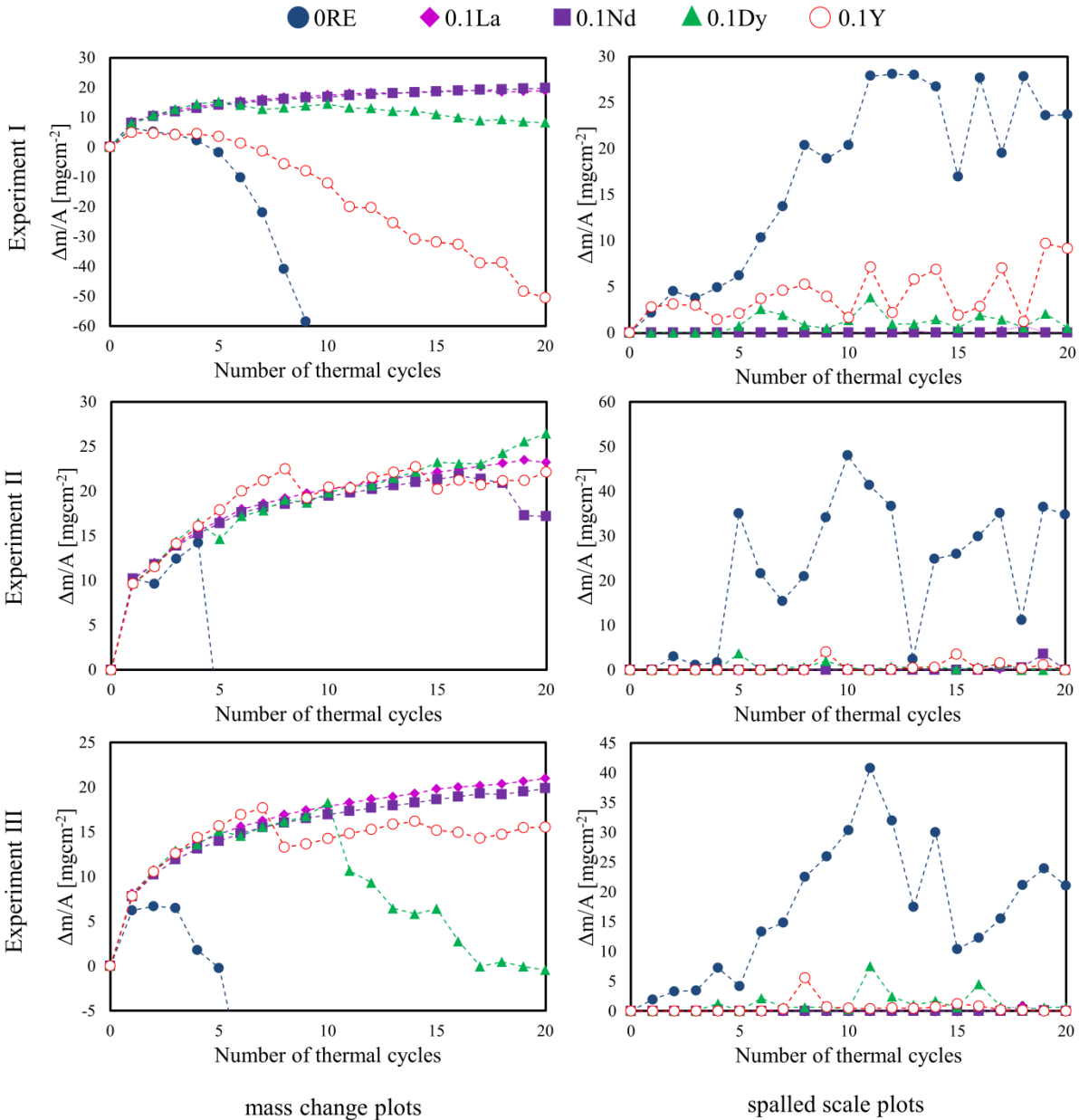


Figure 4.14: Long-term cyclic oxidation plots of the alloys oxidized at 900 °C.

Figure 4.15 shows the results of short-term cyclic oxidation tests of 0RE, 0.1La, 0.1Nd, 0.1Dy, and 0.1Y alloys at 700, 800, and 900 °C. At 700 °C, the 0RE alloy exhibited considerable oxide scale spallation, with two out of three experiments resulting in the  $\Delta m/A$  lower than 0 after a dozen thermal cycles. The oxidation under cyclic oxidation at 800 °C did not result in considerable spallation in the case of any alloys, similar to the long-term

oxidation (Figure 4.13). However, a slight oxide peeling was observed for the ORE alloy in experiment I.

At 900 °C, substantial oxide peeling was noticed in the case of the ORE alloy. Experiment II showed substantial oxide peeling for the 0.1Y alloy, while experiment III revealed a considerable effect for the 0.1Dy alloy. Although the cycles are shorter and the mass gains are lower compared to the previous experiments (Figures 4.12, 4.13, and 4.14), the trends are similar. Sometimes, the RE-doped alloys also exhibit oxide spallation, particularly the 0.1Dy and 0.1Y alloys. Nevertheless, the ORE alloy clearly suffers from thermal cycling at higher temperatures, particularly at 900 °C. When considering resistance to oxide peeling during thermal cycling, alloys containing RE additions exhibit higher oxidation resistance compared to the base alloy.

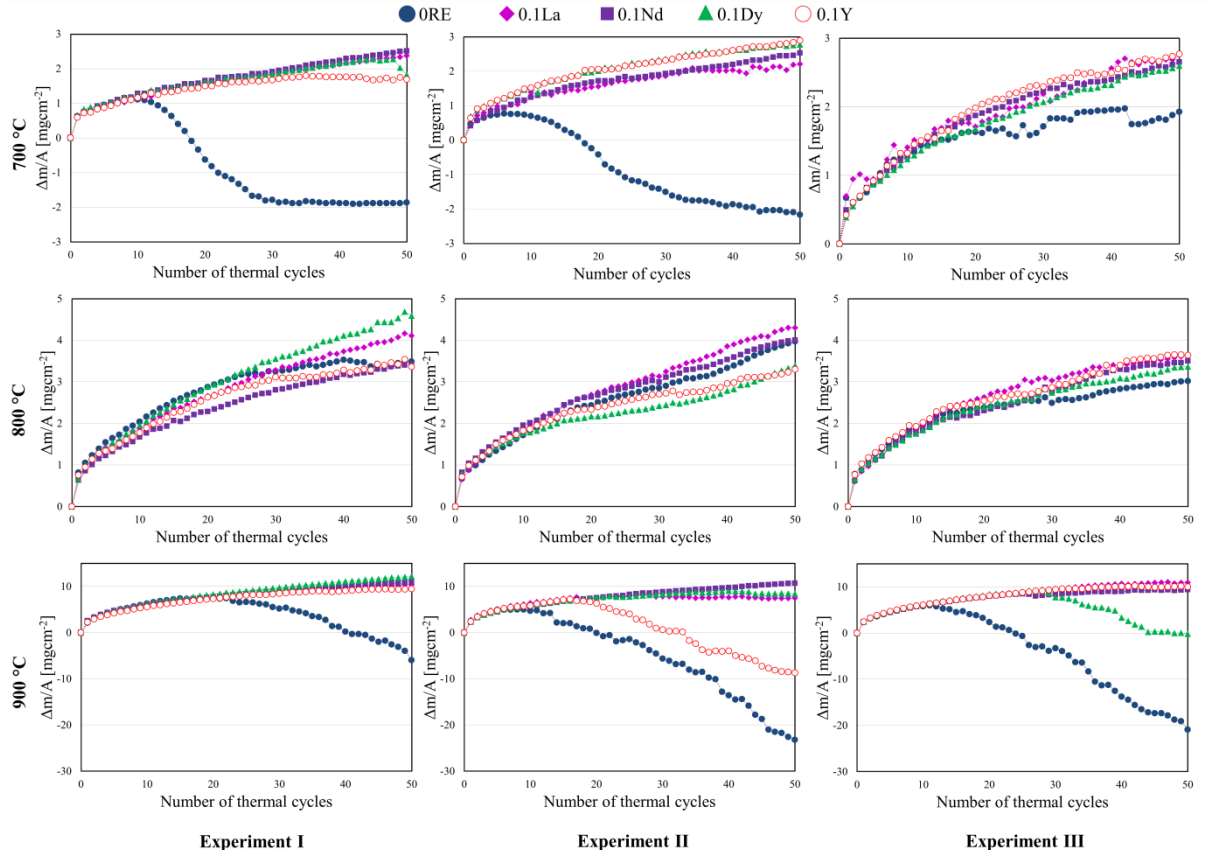


Figure 4.15: Short-term cyclic oxidation plots of the alloys oxidized at 700, 800, and 900 °C.

## 4.5 Microstructural characterization of oxide scales

The last part of the study involved the analysis of oxide scales formed during the isothermal oxidation. The SEM micrographs of the 0RE, 0.1La, 0.1Nd, 0.1Dy, and 0.1Y alloys oxidized at 700°C for 500 h are shown in Figure 4.16. Since high temperature oxidation studies on  $\gamma$ - $\gamma'$  Co-based superalloys typically focus on their oxidation behavior at 800 °C or higher temperatures, it is worthwhile to examine microstructures of the oxide scales at a lower temperature. The oxide scales formed on 700 °C are similar to those formed at 800 °C. They consist of three layers: the OOL, IOL, and  $\gamma'$ -free (Figure 4.16e). At the boundary between IOL and  $\gamma'$ -free zone, an a very thin inner layer that is rich in Al nad O can be found. Below this layer, within the  $\gamma'$ -free zone, the  $\gamma$ /Co<sub>3</sub>W area can be observed. The oxide scales of all the alloys are very similar in this regard, with one exception:  $\gamma'$ -free zone only occurs occasionally in the 0RE alloy, whereas it is more commonly observed in the other alloys.

Additional differences between the base alloy and the RE-doped alloys can be observed in the presence of RE-rich phases. RE-rich phases (I) can be observed below the  $\gamma'$ -free zone. Their morphology and chemical composition are analogous to those after heat treatment (Figure 4.3). The  $\gamma'$ -free zone contains dark grey phases (RE-rich phase II) with the same morphology. These characteristic micro-areas are oxide mixtures that contain W, Co, and the substantial amount of Al (up to 50 at.%) and RE (up to 18 at.%). They typically adhere to a thin Al-rich oxide layer, situated at the interface between the substrate and the oxide scale. These RE-rich phases located between the metal and oxide scale may, in some respects, resemble the oxide keys formed in Ni-based superalloys that contain RE. In addition, oxide mixtures containing RE may also be found within the IOL (RE-rich phases III and IV). The phases III and IV (Figure 4.16f) contain 15.8% and 15.4% Al, respectively, along with 56.6% and 66.6% Co, 13.4% and 14.2% Nd, and 14.2% and 3.9% W, respectively (at%). It is necessary to add that the EDS analysis of such small areas is only approximate. The OOL does not contain any elements other than Co and O. Although the RE-rich areas (RE-rich phases I, II, III, and IV) differ in chemical composition, they all morphologically similar to RE-rich phases (Figure 4.3) and seem to be oxidized RE-rich phases (I). Partial internal oxidation of RE-rich phase I was observed in a substrate (Figure 4.16g). It is worth noting that this phase adheres to the same grain boundary as RE-rich phase IV (Figure 4.16f).

Similar RE-rich areas (I, II, and III) were also observed in the scales that were oxidized at 800 and 900 °C. The microstructures of the oxide scales formed after the alloys were oxidized at 800 °C for 500 h are shown in Figure 4.17.

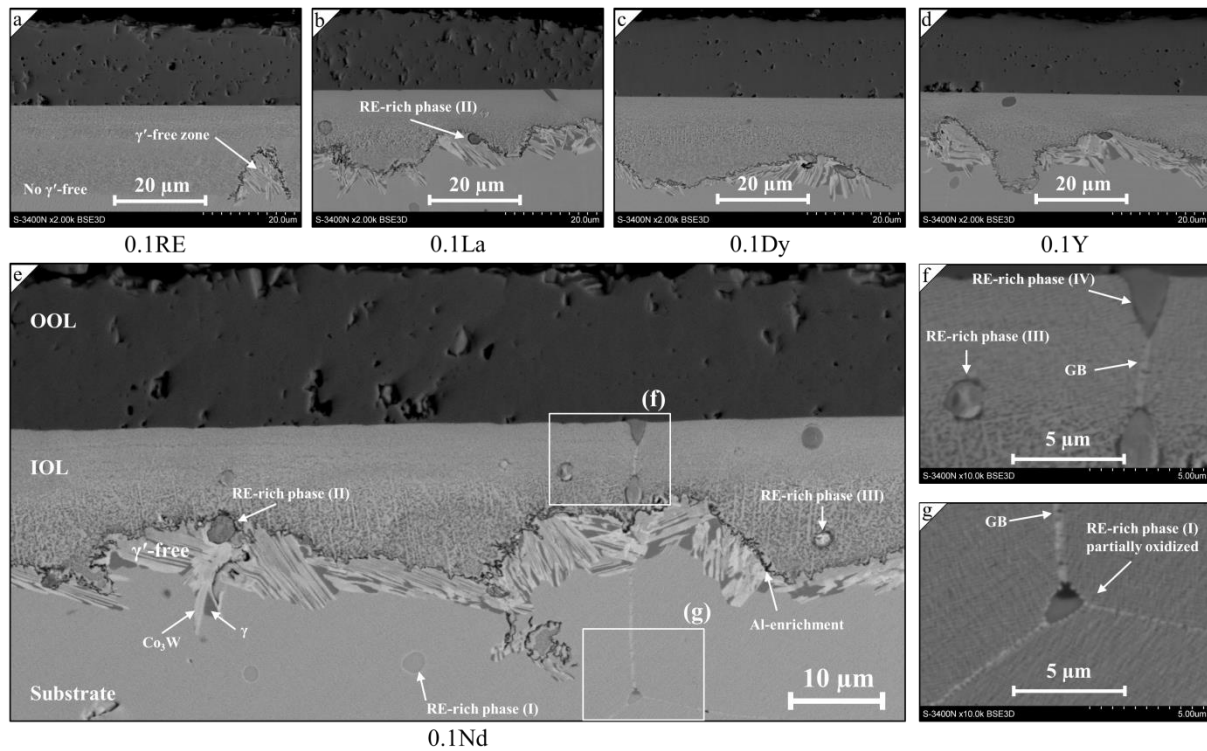


Figure 4.16: The SEM micrographs of the oxide scale formed on the alloys after isothermal oxidation at 700 °C for 500 h; a) 0RE; b) 0.1La; c) 0.1Dy; d) 0.1Y; e-g) 0.1Nd.

While the formation of oxide scales at 800 °C was similar to that observed at 700 °C during oxidation, the thickness of the  $\gamma'$ -free zone was found to be greater in all investigated alloys. At 800 °C, the IOL was separated from the  $\gamma'$ -free zone by a thin layer of Al-rich oxides. However, this layer was not continuous, similar to what was observed at 700 °C. Moreover, the oxide scales were bumpy and uneven in all cases.

Compared to the 0RE alloy, the oxide thickness of the RE-doped alloy was lower. Additionally, the oxide scales of the RE-doped alloy contained both oxidized and non-oxidized areas that were rich in RE (Figures 4.17f-e). In the IOL, only one type of the RE-rich area was observed (III). The chemical composition measured in this area, for the 0.1Nd alloy, was as follows: 19.2% Al, 39.8% Co, 20.2% Nd, 20.8% W (at%). Furthermore, numerous RE-rich areas (II) adhering to the thin Al-rich layer were observed within the  $\gamma'$ -free zone (Figure 4.17g). The chemical composition measured in this area, for the 0.1Nd alloy, was as follows: 64.1% Al, 7.4% Co, 12.9% Nd, 15.5% W (at%). Moreover, in the substrate, internally oxidized RE-rich phase (I) was found (Figure 4.17e).

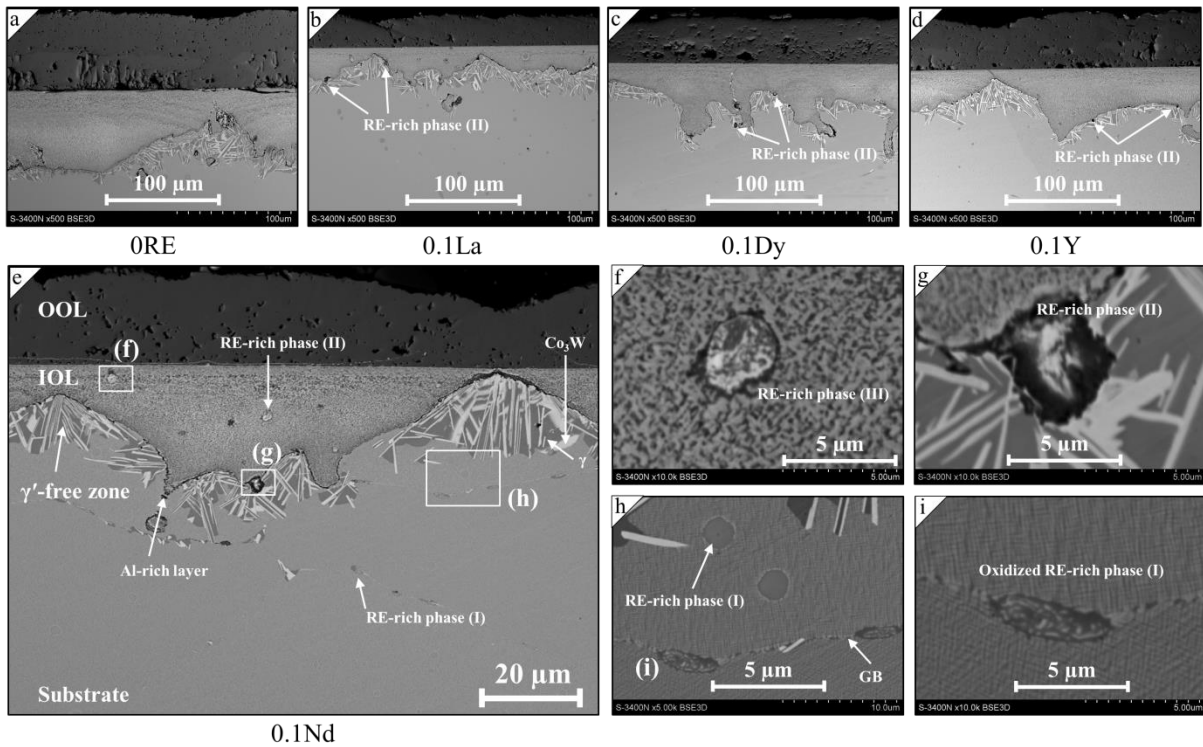


Figure 4.17: The SEM micrographs of the oxide scale formed on the alloys after isothermal oxidation at 800 °C for 500 h; a) 0RE; b) 0.1La; c) 0.1Dy; d) 0.1Y; e-i) 0.1Nd.

Figure 4.18 shows SEM micrographs of the oxide scales formed on the 0.1La, 0.1Nd, 0.1Dy, and 0.1Y alloys after oxidation at 900 °C for 500 h. It was not possible to observe the oxide scale formed on the 0RE alloy due to a severe oxide peeling, however, the scale formed after 300 h may be seen in Figure 10a. The 0.1La and 0.1Nd alloys were characterized by presence of discontinuous inner layer of Al-rich oxides as well as relatively wide  $\gamma'$ -free zone. They exhibited also the lowest overall thickness of the scale compared to other alloys (0.1Dy, 0.1Y). It is worth to note that Al-rich oxide segments in the RE-doped alloys grew parallel to the alloy surface. In the case of the 0.1La (Figure 4.18d), one can observe formation of discontinuous layer, thicker compared to that of formed at lower temperatures. After oxidation at 900 °C, similar RE-rich oxide phases were found in IOL (Figure 4.18e) and  $\gamma'$ -free zone (Figure 4.18f). Moreover, internal oxidation of RE-rich phases in the substrate (similar to Figure 4.17i) were noticed as well. The concentration of oxide segments rich in Al in the  $\gamma'$ -free zones of the 0.1Dy and 0.1Y alloys was found to be lower compared to that of the 0.1La and 0.1Nd alloys, although such segments were observable. The chemical composition measured in micro areas marked in Figure 4.18 is shown in Table 4.10.

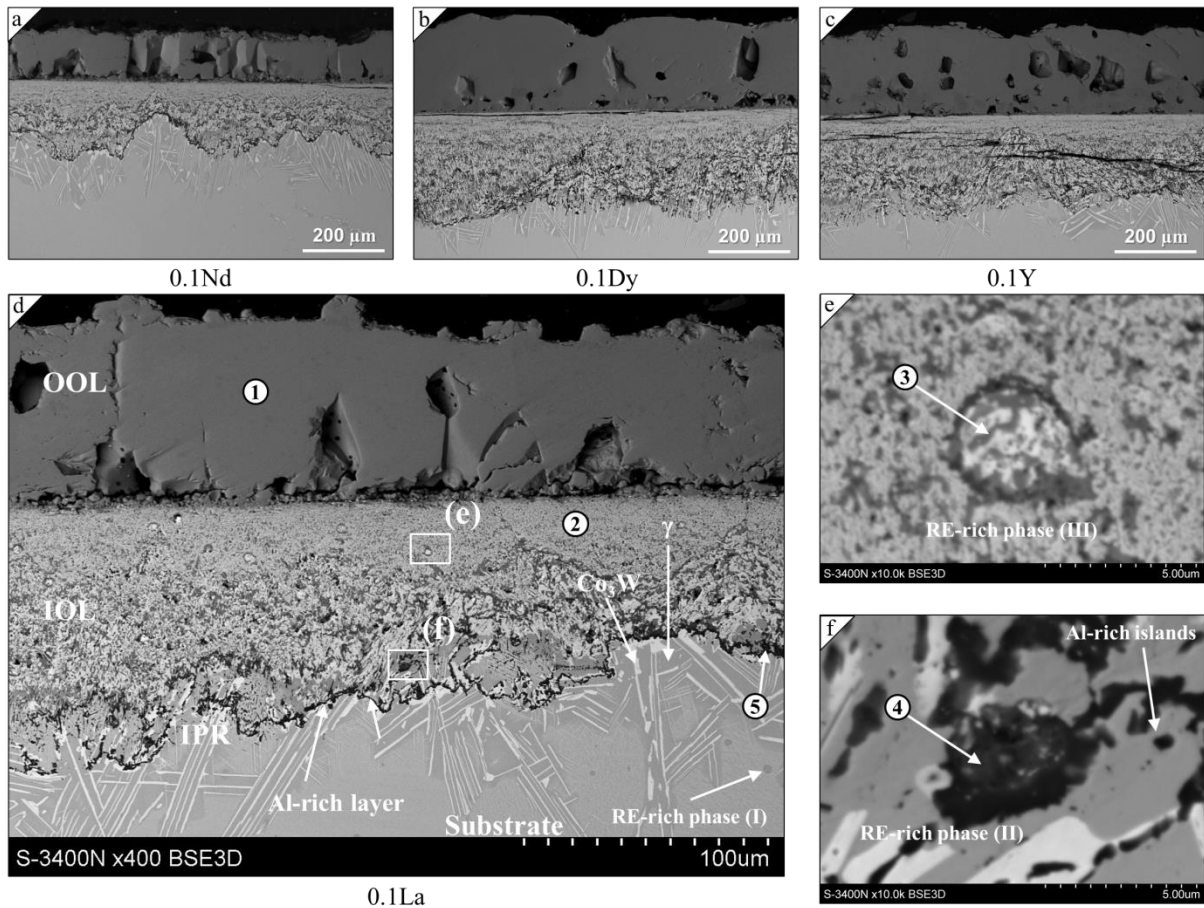


Figure 4.18: The SEM micrographs of the oxide scale formed on the alloys after isothermal oxidation at 900 °C for 500 h; a) 0.1Nd; b) 0.1Dy; c) 0.1Y; d-f).

Table 4.10: Chemical composition (EDS) in micro areas corresponding to EDS points in Figure 4.18.

Point	O-K	Al-K	Co-K	La-L	W-M
1	+	-	100	-	-
2	+	12.4	67.6	-	20.0
3	+	5	66.1	15.3	13.6
4	+	74.2	21	1.2	3.6
5	+	82.6	13.2	-	4.2

Apart from the thicknesses of the  $\gamma'$ -free zone and the morphology and amount of formed Al-rich oxides, the presence of RE-rich phases and oxides is the main difference between the oxide scales formed on RE-doped alloys and those formed on the base alloy. The analysis of these phases requires more advanced techniques than SEM, such as STEM and SAED. Although not all alloys were analyzed in this way, phase and chemical composition analyses were successfully performed on the alloy containing 0.5 at% yttrium (rather than 0.1 at%). The results of such study were analyzed and published in the journal Corrosion Science [151].

It is worth using these results in this dissertation due to the almost identical morphology of the oxidized RE-phase between alloys containing 0.1 and 0.5 at% RE. For the purpose of advanced analysis of the oxide scale formed at 900 °C on the Co-9Al-9W-0.5Y alloy, three lamellae were prepared. The first lamella was acquired from the area morphologically corresponding to RE-rich phase III (Figure 4.18e), while the second lamella was obtained from the region corresponding to RE-rich phase II (Figure 4.18f). The third lamella was obtained from the region where the RE-rich phase was internally oxidized, as illustrated in Figure 4.17i.

Figure 4.19a shows the STEM micrograph of the lamellae corresponding to RE-rich phase III, but acquired from the Co-9Al-9W-0.5Y alloy. The micrograph displays a portion of the IOL with a Y-rich oxide area (“d”) visible. The red arrows in the micrographs correspond to areas where SAED was performed, and green arrows indicate EDS measurements in micro areas. Chemical composition measurements are listed in Table 4.11, and the phase analysis of the diffraction patterns is presented in Figure 4.20. The results of phase and chemical composition analysis showed that the Y-rich areas (Figure 4.19d) were composed of  $Y_2WO_6$ , CoO, and  $CoAl_2O_4$  phases. CoO,  $CoAl_2O_4$ , and  $CoWO_4$  phases were present in other areas of the IOL (Figures 4.19b and 4.19c). EDS analysis indicated significant variations in the Co:Al ratio in the  $CoAl_2O_4$  micro areas, which requires further discussion. The substitution of Al in  $Co_3O_4$  results in the formation of the  $CoAl_2O_4$  spinel. Despite variations in the Al content, the spinels displayed the same lattice type (Fd-3m, space group no. 227). The lattice parameter “a” for  $Co_3O_4$ ,  $Co_2AlO_4$ , and  $CoAl_2O_4$  oxides was measured to be 8.036, 8.067, and 8.092 Å, respectively [158]. Consequently, the differences observed in the SAED analysis (Figure 4.20) were minimal. To be precise, the identified Co-Al spinels could be described as  $Co_{3-x}Al_xO_4$ . No Y was found in the IOL out of RE-rich oxide (Figure 4.19c). This element was detected only in the area “d”.

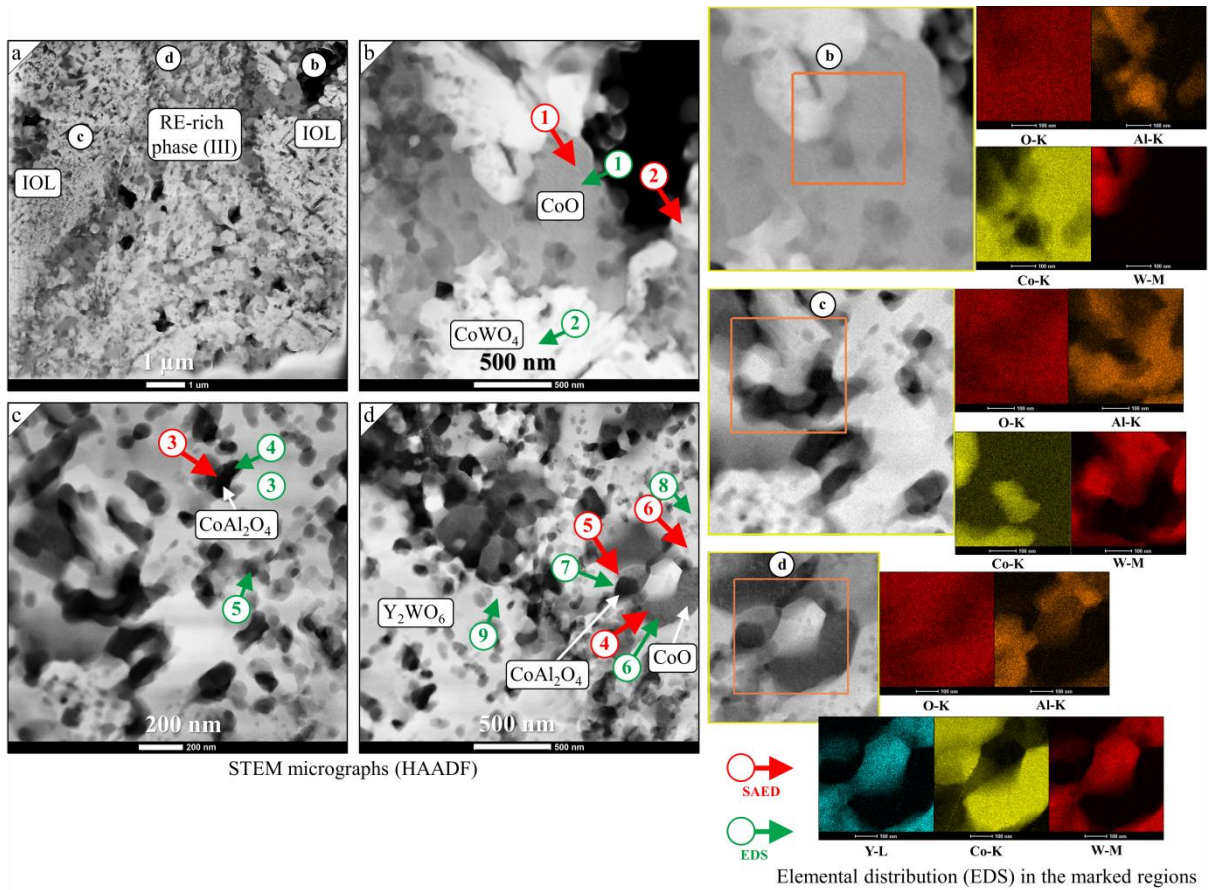


Figure 4.19: Microstructure of oxides formed in the IOL of Co-9Al-9W-0.5Y, including HAADF micrographs and elemental distribution (EDS) mapping in the marked regions.

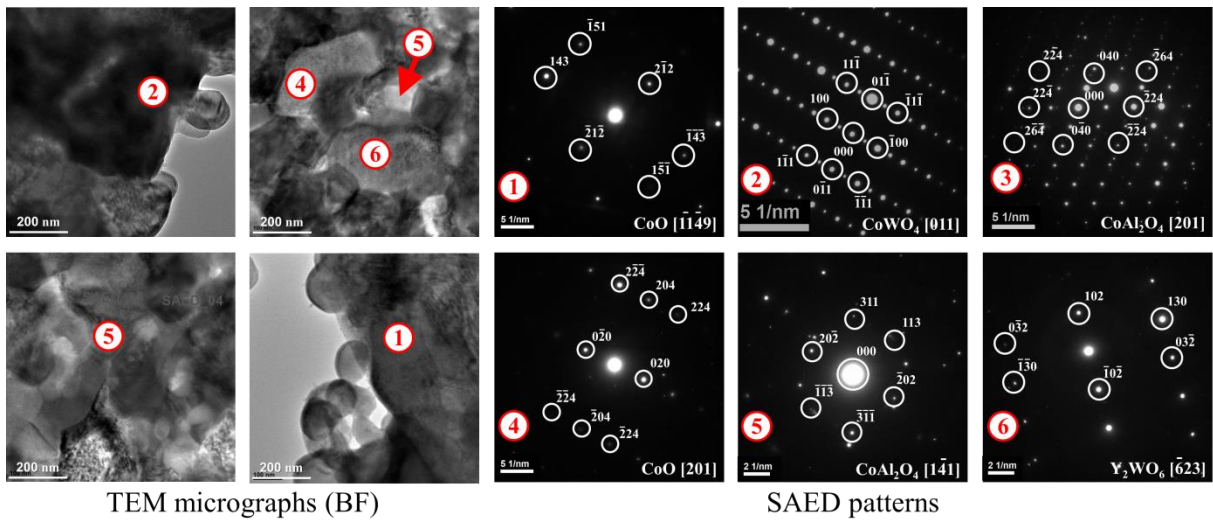


Figure 4.20: TEM (BF) micrographs and SAED patterns corresponding to areas marked in Figure 4.19.

Table 4.11: Chemical composition (EDS) in micro areas corresponding to EDS points in Figure 4.19.

Point	Atom %				
	O-K	Al-K	Co-K	Y-K	W-L
1	58.06	–	41.93	–	–
2	55.68	–	23.1	–	21.21
3	76.97	–	14.68	–	8.33
4	62.22	24.08	13.54	–	0.14
5	65.14	12.85	15.09	–	6.9
6	52.05	0.3	47.49	–	0.15
7	55.83	11.26	32.79	–	0.1
8	57.13	7.13	2.72	23.31	9.68
9	71.07	1.75	0.64	16.67	9.85

The STEM micrograph of the lamella acquired from the area similar to RE-rich phase II is presented in Figure 4.21a, which displays the Y-rich oxidized area (Figure 4.21b) within the IPR (Figure 4.21c). Table 4.12 shows the results of the chemical composition measurements of the micro areas, and Figure 4.22 presents the phase analysis based on the obtained diffraction patterns. In the zone containing Y (Figure 4.21b), the image displays different characteristic regions with white areas (EDS point no. 4), gray areas with various levels of gray (EDS points no. 1, 2), and dark areas (EDS points no. 3, 6) visible through color contrast. Two crystalline phases are distinguishable, namely  $Y_2O_3$  (gray area) and  $Co_3W$  (bright color area). Polycrystalline patterns (SAED point no. 3) were observed in other regions (dark areas). Regarding the element distribution, the bright areas were found to be composed of only Co and W, whereas the gray areas contained O and Y, or O, Y, and Al. The dark areas contained mostly O, Al, and small amounts of Y. The remaining internal oxidation zone (c) was composed of Co-9Al-9W and included  $\gamma-Co_{ss}$ ,  $Al_2O_3$ , and  $Co_3W$  phases. Taking into consideration the morphology and chemical composition, the Y-rich area is believed to be composed of  $Co_3W$  and a mixture of  $Al_2O_3$  and  $Y_2O_3$ . No Y-aluminates were detected, whereas the SAED pattern (3) implies presence of a mixture of alumina and yttria. Taking into account the similarity of the black areas (EDS point no. 6) with  $Al_2O_3$  (EDS point no. 9), these areas could be  $Al_2O_3$ , whereas no pattern allowing for identification was acquired.

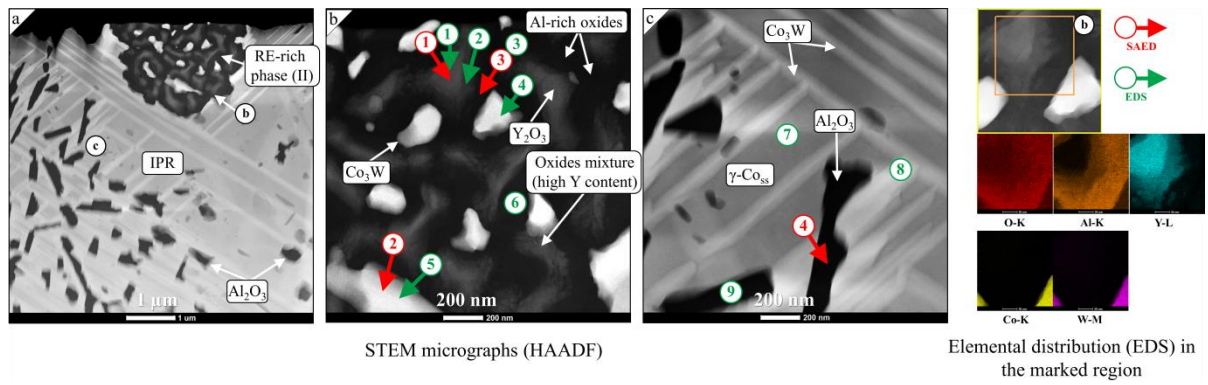


Figure 4.21: Microstructure of oxides formed in the IPR of Co-9Al-9 W-0.5Y, including HAADF micrographs and elemental distribution (EDS) mapping in the marked regions.

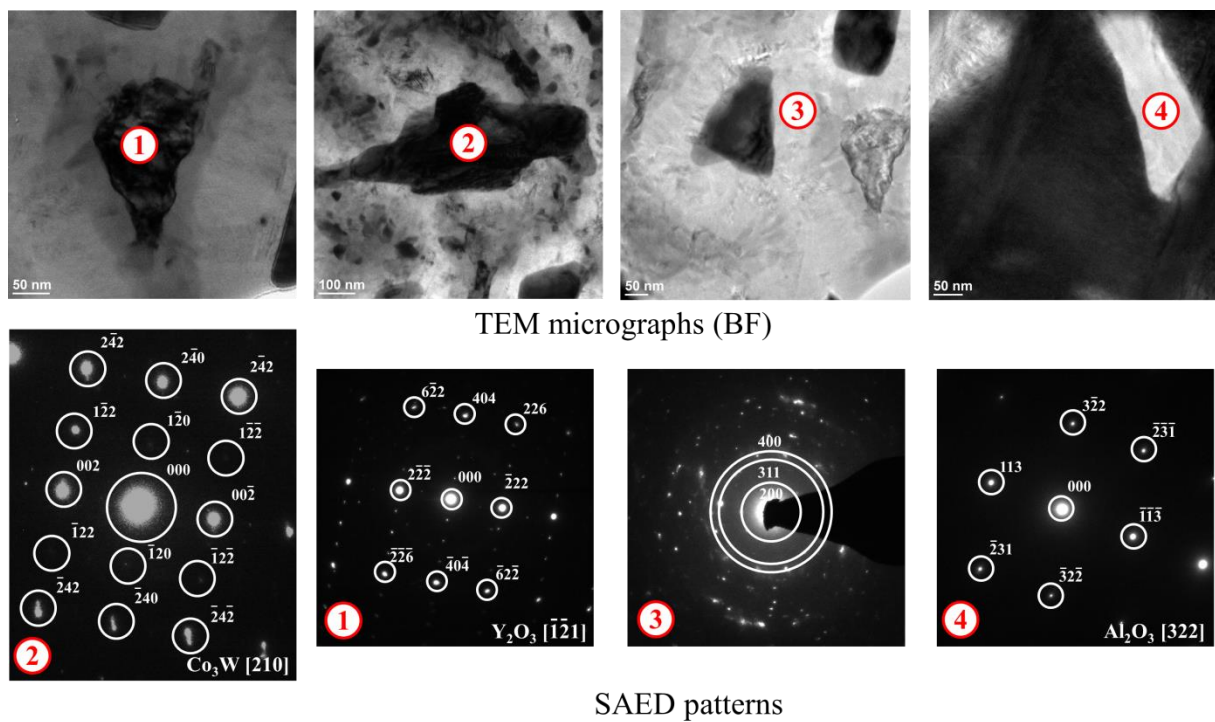


Figure 4.22: TEM (BF) micrographs and SAED patterns corresponding to areas marked in Figure 4.21.

Table 4.12: Chemical composition (EDS) in micro areas corresponding to EDS points in Figure 4.21.

Point	Atom %				
	O-K	Al-K	Co-K	Y-K	W-L
1	65.71	–	–	34.29	–
2	61.03	18.74	–	20.21	–
3	69.92	28.6	–	1.46	–
4	–	–	80.77	–	19.22
5	–	–	82.44	–	17.55
6	68.62	30.41	–	0.96	–
7	–	–	90.55	–	9.44
8	–	–	80.11	–	19.88
9	66.52	33.47	–	–	–

The STEM micrograph of the microstructure of the lamella corresponding to internally oxidized RE-rich phase I is presented in Figure 4.23b. Table 4.13 exhibits the chemical composition measurements of the micro areas, while the phase analysis based on the obtained diffraction patterns is demonstrated in Figure 4.24. The micrograph (Figure 4.23b) displays an elongated precipitate surrounded by dark areas (point no. 1) with  $\gamma$ - $\gamma'$  zone outside the discussed phases. The dark areas were mainly composed of O and Y, as observed from the element distribution, which is consistent with the phase analysis showing the presence of  $Y_2O_3$ . However, localized Al enrichment was detected near these phases. The elongated precipitate (Figure 4.23c) was identified as  $\gamma$ - $Co_{ss}$  based on the SAED results (SAED point no. 2), while the other phase constituent (SAED point no. 3) was  $\gamma'$ - $Co_3(Al, W)$ .

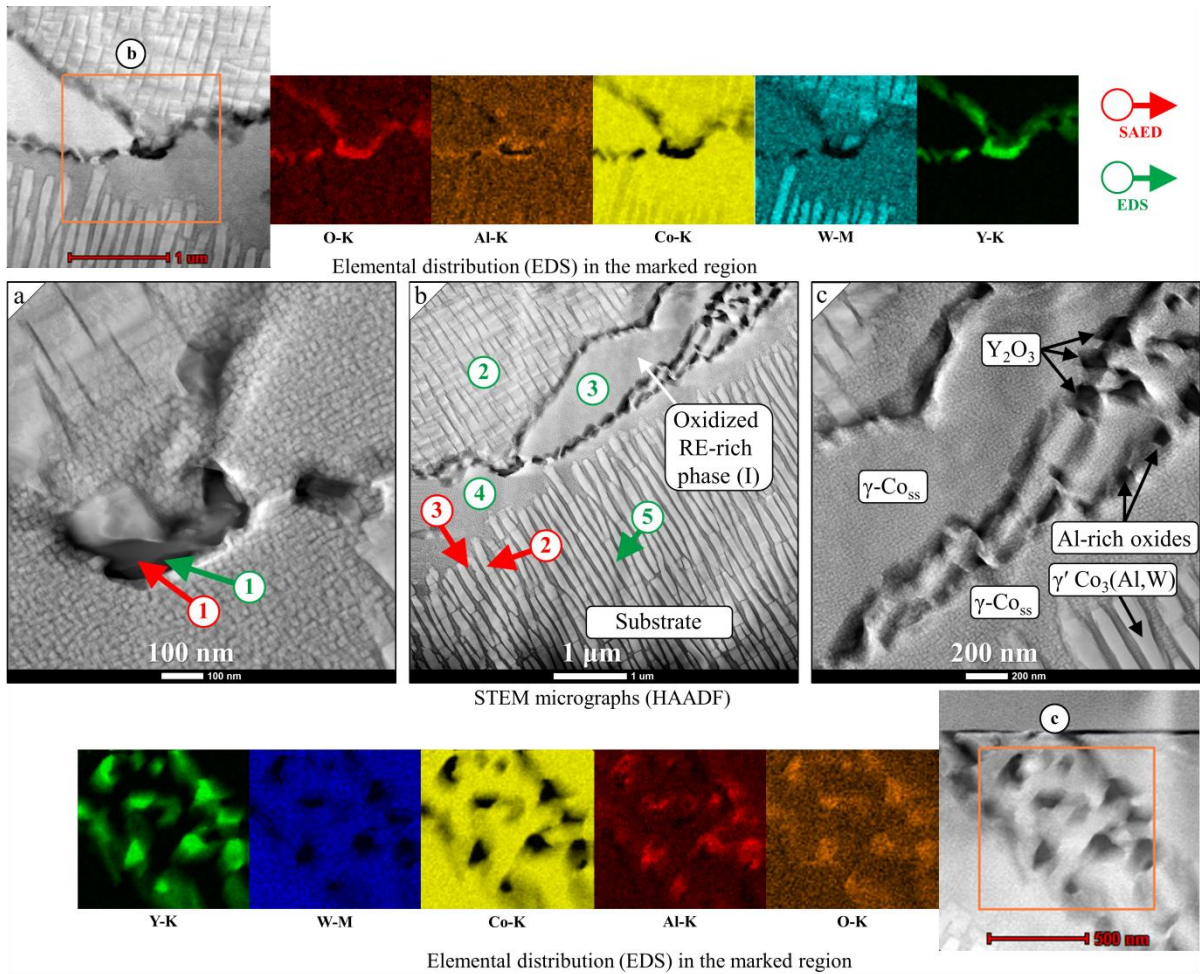


Figure 4.23: Microstructure of oxides formed internally in a substrate of Co-9Al-9 W-0.5Y, including HAADF micrographs and elemental distribution (EDS) mapping in the marked regions.

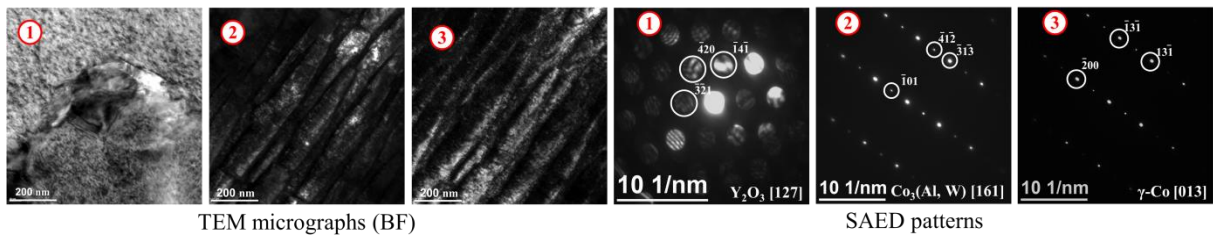


Figure 4.24: TEM (BF) micrographs and SAED patterns corresponding to areas marked in Figure 4.23

Table 4.13: Chemical composition (EDS) in micro areas corresponding EDS points in Figure 4.23.

Point	Atom %				
	O-K	Al-K	Co-K	Y-K	W-L
1	14.11	–	1.91	83.97	–
2	–	3.27	87.74	–	8.97
3	–	2.28	91.67	–	6.03
4	–	3.43	91.61	–	4.95
5	–	4.68	84.8	–	10.5

In the publication [151], the early stages of scale formation during oxidation of the Co-Al-W-Y alloy were studied. Similar observations were made for the 0RE and 0.1Nd alloys. The SEM micrographs presenting oxide scales formed on the alloys at 900 °C for 1, 3, 5, 25, 100, 300, and 500 h are shown in Figure 4.25. It is clear that the outer oxide layer (OOL) and inner oxide layer (IOL) are formed in the beginning of the oxidation (1 h) in both the 0RE and 0.1Nd alloys. The oxide growth of the alloys seems to be similar up to 100 h. After longer exposure, the IRP in the 0.1Nd alloy is wider compared to that of 0RE, and more coagulated Al<sub>2</sub>O<sub>3</sub> segments can be observed. In all oxidation experiments, severe oxide spallation in the lower part of the IOL occurred in the 0RE alloy after 500 h of oxidation (Figure 4.25). After 500 h of oxidation at 900 °C, only IPR of the 0RE alloy can be observed. It contains small amount of segments of Al oxides and discrete oxide precipitations. The early oxidation stages revealed oxide intrusion caused by internal oxidation of the Nd-rich phases via grain boundaries. Such oxide intrusions were rich in Al.

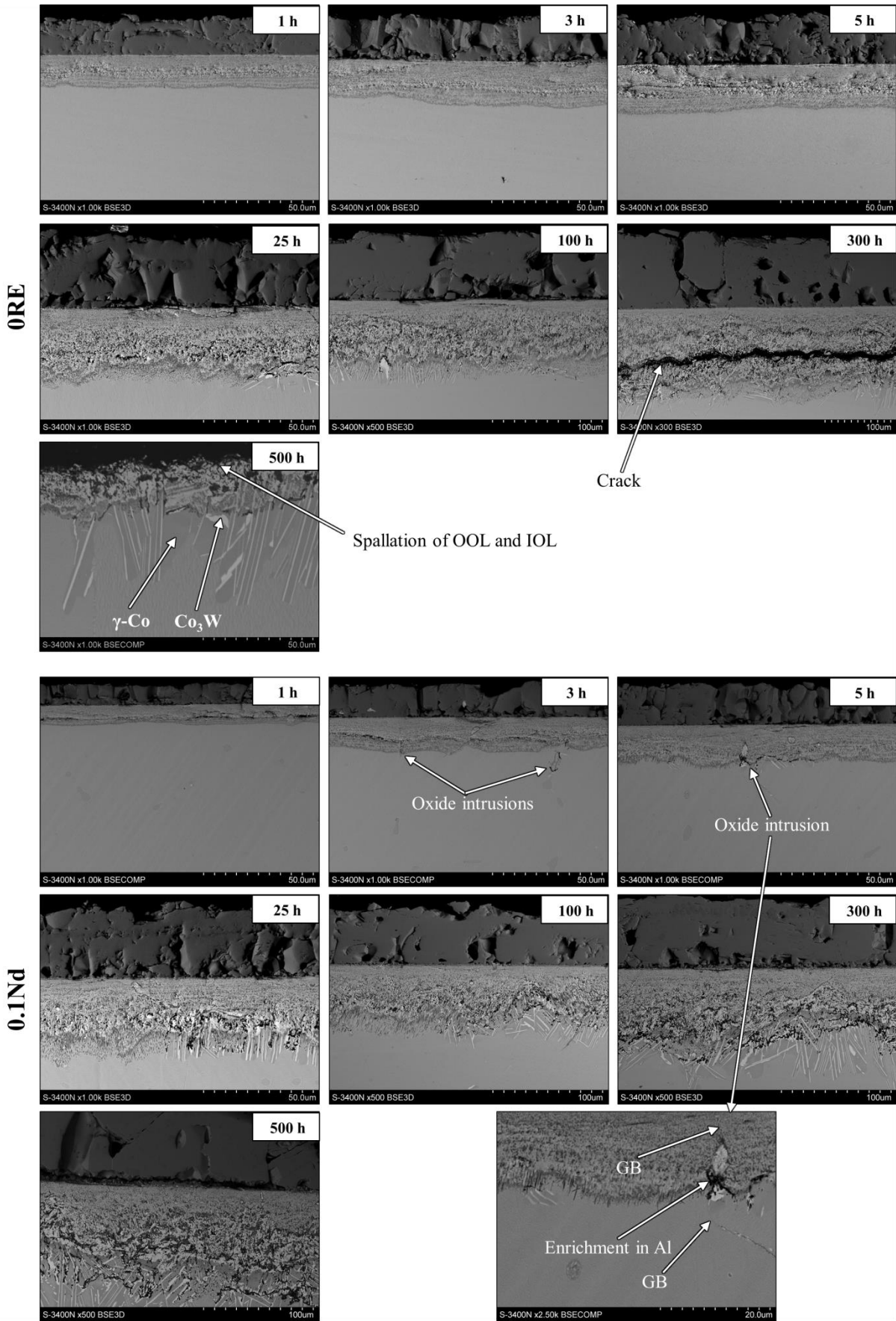
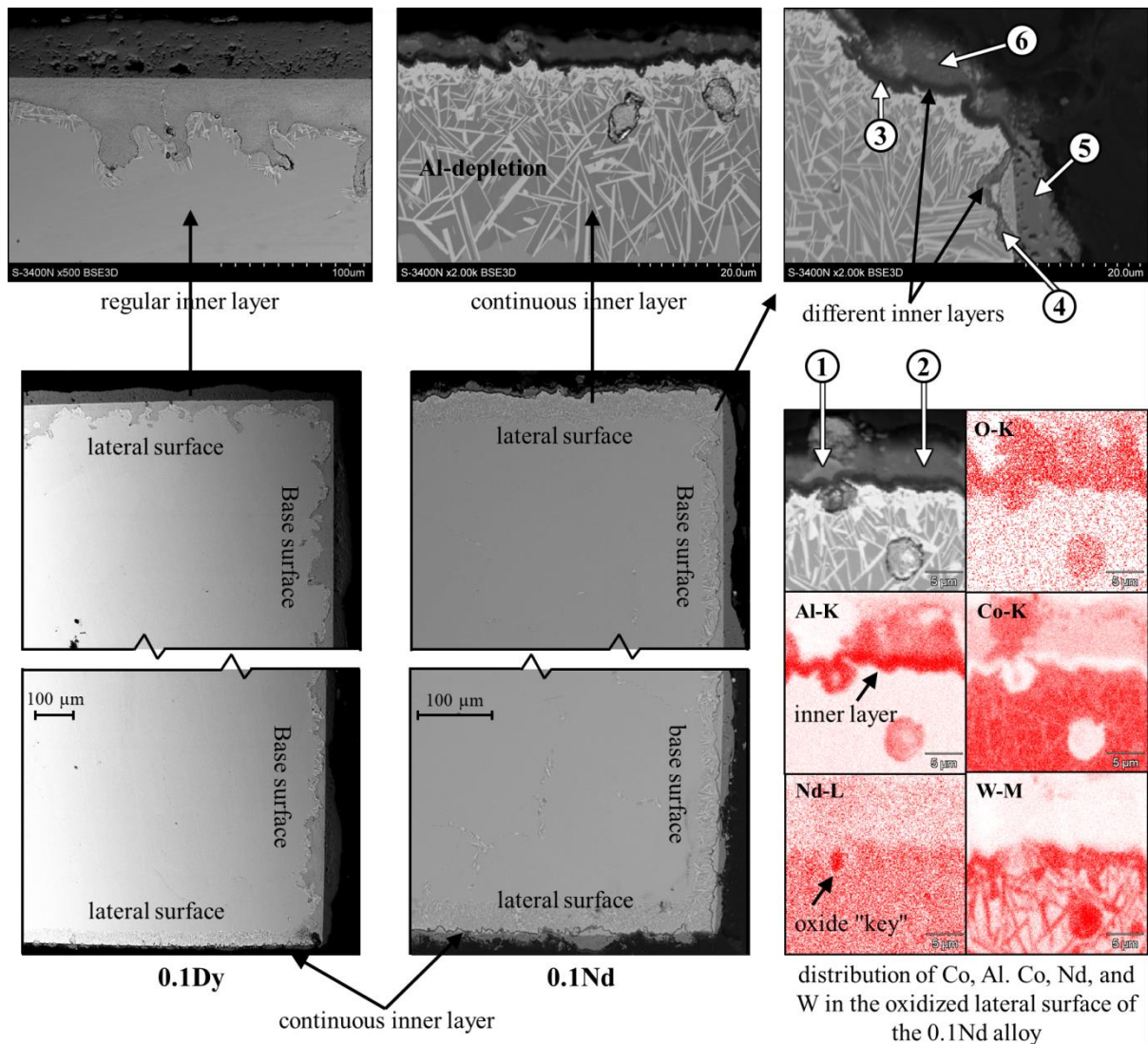


Figure 4.25: SEM micrographs presenting oxide scale formed on the ORE and 0.1Nd alloys after 1, 3, 5, 25, 100, 300, and 500 h of oxidation at 900 °C.

Although non-protective oxide scales were formed during the oxidation of the Co-based alloys, there were some exceptions. Observations of cross-sectional images of the alloys oxidized at 800 °C for 500 h showed interesting anomalies. On the lateral surfaces of some samples containing RE, the formation of a continuous inner, Al-rich layer was noticed (see Figure 4.26). The oxide scales in these areas were composed of an outer, mixed oxide zone and an inner oxide zone rich in Al. The outer zone in such areas is composed of Co oxides (point no. 1) and complex oxides, presumably Co-Al spinels (point no. 2). The inner layer located beneath seems to contain a considerable amount of Al<sub>2</sub>O<sub>3</sub> (point no. 3). The chemical composition in micro-areas marked in Figure 26 is shown in Table 4.14. Figure 26 also shows that at the corner, a transition from the scale formed on the lateral surface to that on the base surface can be observed. The inner layers formed on different surfaces are characterized by noticeably different chemical compositions (points no. 3 and 4), which is even more distinct for the outer layers (points no. 5 and no. 6). Below the inner oxide layer in the lateral part of the sample, the thick  $\gamma'$ -depleted zone composed of  $\gamma$ -Co and Co<sub>3</sub>W needles may be noticed. Such area is a result of substantial Al-depletion and is substantially thicker compared to the outer layer. Very low thickness of the outer layer may suggest that the inner layer formed on the lateral surface of the sample is a diffusion barrier.

It is important to highlight that the phenomenon observed was not consistently reproducible in all cases. For instance, in the case of the 0.1Dy alloy, a thin protective oxide layer was observed at one location, while at another location, the oxide scale appeared similar to that of the base surface. Furthermore, it should be noted that not all RE-containing samples, including some Nd-doped ones, exhibited the formation of such regular oxide layers on their lateral surfaces. Thus, while these observations provide a potential avenue for further research, they do not constitute conclusive proof of the effectiveness of reactive elements in promoting protective oxide scale formation. Moreover, the average thickness of such scale and the  $\gamma$ /Co<sub>3</sub>W zone was ca. 50  $\mu\text{m}$ , which is not substantially lower compared to the average oxide scale in the base surface (about 60  $\mu\text{m}$ ). Although the observed oxide scale is thin, the  $\gamma$ /Co<sub>3</sub>W zone below is very thick due to Al-consumption. The morphology of the  $\gamma'$ -depleted zone in Co-Al-W alloys is unfavourable in view of the alloy's performance and should not be excessively deep. The  $\gamma$ /Co<sub>3</sub>W zone may be eliminated if the Co-Al-W alloy is alloyed with Ni [103].



SEM micrographs of the 0.1Dy and 0.1Nd alloys oxidized at 800 °C for 500 h

Figure 4.26: SEM micrographs of base and lateral surfaces of the 0.1Dy and 0.1Nd after 100 h of oxidation at 800 °C. Lateral surfaces reveal formation of continuous inner layer, especially in the case of the 0.1Nd alloy; the distribution of O, Al, Co, Nd and W (EDS) in such oxide layer is presented.

Table 4.14: Chemical composition (EDS) in micro areas corresponding to EDS points in Figure 4.26.

Point	Atom %				
	O-K	Al-K	Co-K	Nd-L	W-M
1	+	0.2	99.8	-	-
2	+	70	29.9	-	0.1
3	+	80.5	16.4	0.2	2.9
4	+	81.8	3.2	-	15
5	+	-	100	-	-
6	+	72.5	27.5	-	-

The results obtained from the microstructural scale analysis are consistent with those from the isothermal oxidation experiments, and can provide additional insights for interpreting the data from cyclic oxidation as well. The isothermal oxidation studies showed the appearance of the oxide scale after 1 h of oxidation (short-term cycle) and 25 h (long-term cycle) as well as the evolution of scale thickness. While the oxide scales formed during the cyclic oxidation studies were not specifically analyzed, oxide scale microstructure up to the first occurrence of scale spallation resembles that observed during isothermal oxidation. As a result, there is room for further analysis of the oxide scales in this regard.

Based on the oxidation kinetics and the observed oxide scales, all the investigated alloys exhibited comparable oxide scale growth mechanism. However, there were some small differences related to the presence of RE in the alloys, particularly in the case of the 0.1La and 0.1Nd alloys. Therefore, the relationship between oxidation kinetics and oxide scale formation will be discussed further in the subsequent section.

## 5. Discussion

### 5.1 Microstructure and thermal analysis of alloys

The microstructure and phase composition of an alloy are important in understanding its oxidation behavior. Thus, microstructural evaluation is an important part of the thesis. Although the microstructural aspects of Co-Al-W alloys are well described in the literature, before the preparation of the dissertation, there were no almost no studies on the microstructure of Co-Al-W alloys doped with La, Nd, Dy, or Y. The only works on RE-doped  $\gamma$ - $\gamma'$  Co-based superalloys that one can refer to are [76, 89, 90, 144-151]. It is worth to put the obtained results in the literatural context.

A comprehensive investigation into the effects of RE on the microstructure of Co-Al-W alloys would be highly beneficial and add significant value to the current state of the art. In the studies included in the dissertation, RE were introduced to the melt in the form of pure metals. The nominal content (0.1 at%) was high enough to detect their presence in the alloy. In as-cast state, local concentration of RE was found in interdendritic spaces. Such microsegregation behavior is not suprising, since the solubility of RE in Co is negligible. Du and Lü [157] calculated that the maximum solubility of Y in  $\alpha$ -Co is approximately 0.1 at% at 1300 °C, but this value decreases significantly at lower temperatures (to around 0.001 at% 900 °C). The solid solubility of Nd in fcc-Co is extremely small, estimated to be 0.03 at.% at 1000 °C [159]. Similarly, Dy and La are also expected to have very low solubility in Co. Therefore, it is possible that the RE present in the alloys may take the form of intermetallic phases or non-metallic inclusions if the alloys become contaminated. Although some non-metallic inclusions such as oxides or sulfides (as shown in Figure 5.1) were observed, the majority of RE in the alloys was present in the form of Co-RE intermetallic phases. Besides RE, Al was also found to be segregating to interdendritic spaces. This is a common observation in Co-Al-W alloys obtained by the VIM technique [152]. As shown in Figure 5.1, the areas of Co-RE phases are chemically non-homogeneous and depleted in W. Given the importance of  $\gamma'$ -containing alloys for potential applications, particular attention was paid to the microstructure of as-aged specimens.

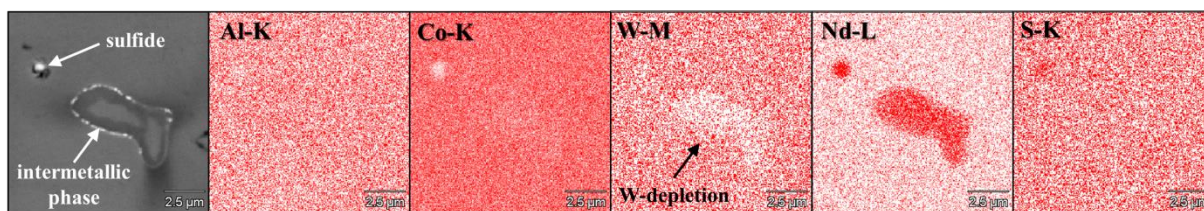


Figure 5.1: Distribution of Al, Co, W, Nd, and S in an interdendritic area of the as-cast 0.1Nd alloy.

The solution heat treatment of the alloys was conducted at 1200 °C for 16 h. The microstructure after such heat treatment was similar to that of after aging, whereas no  $\gamma'$  was detected. The RE-rich phases exhibited a uniform distribution across the alloys, primarily located at grain boundaries, similar to the as-aged state. The solution heat treatment led to the homogenization of chemical composition throughout the ingot, both at macro- and micro-areas, and resulted in the supersaturation of  $\gamma$ -Co. This supersaturation caused a decrease in hardness compared to the as-cast state. Upon aging, the microstructure resembled that of Co-9Al-9W, indicating that, apart from grain boundary precipitations, the presence of RE did not significantly impact the phase composition of Co-Al-W alloys.

Two methods, XRD and EBSD, were utilized to examine the structure of RE-rich phases. XRD analysis of the alloys containing 0.1 at% of RE did not reveal any peaks corresponding to the RE-rich phases. However, in a specific publication [151], the Co-Al-W alloy containing 0.5 at% Y was analyzed. The XRD analysis did not provide conclusive evidence, but the EBSD analysis showed the presence of two phases:  $Y_2Co_{15}Al_2$  (P63/mmc) and  $YCo_5$  (P6/mmm). The results of the EBSD analysis for the alloy containing 0.5 at% Y were similar to those of the alloy containing 0.1% (as shown in Table 4.4). The presence of the second phase was confirmed by SAED, although the results only refer to a localized phase. SAED analysis was also performed for the Co-Al-W-Ce alloy, indicating presence of the  $Ce_2Co_{15}Al_2$  phase, which is an extension of the binary  $Ce_2Co_{17}$  phase. The  $Ce_2Co_{17}$  phase was detected via XRD analysis of the Co-9Al-9W-0.5Ce alloy. In the Ce-containing alloys, EBSD analysis was also conducted, revealing the presence of the  $CeCo_4Al$  phase (P6/mmm). Distinguishing between the  $RECo_5$  and  $RE_2Co_{17}$  phases is challenging using XRD and EBSD methods, particularly when their content in the alloy is very low. Additionally, limited literature data are available to reference in this regard. ThermoCalc modeling can accurately simulate the behavior of only certain RE elements, such as Y and Ce. However, the accuracy of such analysis in multicomponent alloys is debatable. While the information provided in the data on binary Co-RE systems [154-157] can be helpful, it can also be misleading. This is because the

presence of other elements, such as Al, can alter the structure of RE-rich phases and their melting temperatures, making the interpretation of the data more complex. Table 5.1 illustrates the differences observed in various RE-rich phases with and without the addition of Al. The presence of as little as ca. 5 at% of Al in the  $\text{Ce}_2\text{Co}_{17}$  phase (resulting in  $\text{Ce}_2\text{Co}_{16}\text{Al}$ ) can result in a structural change, and increasing Al content can further increase the lattice parameters. Similar observations can be made for the  $\text{Nd}_2\text{Co}_{17-x}\text{Al}_x$  and  $\text{Y}_2\text{Co}_{17-x}\text{Al}_x$  phases. Based on XRD data, it is expected that similar phenomena occur in Dy-rich phases as well. In the case of the  $\text{LaCo}_{13-x}\text{Al}_x$  phases, the increase in Al content from  $x=0$  to  $x=2.7$  leads to the increase in the lattice parameter “a” [Å], while the  $\text{LaCo}_{10}\text{Al}_3$  phase has a different structure. The XRD patterns and relevant literature data were used for EBSD analysis. Unfortunately, no data on ternary RE-Co-W phases could be found.

Table 5.1: Structure type and lattice constants of different RE–Co and RE–Co–Al phases.

Composition	Structure type	a [Å]	c [Å]	Reference
$\alpha\text{Ce}_2\text{Co}_{17}$	P63/mmc	8.38	8.13	[160]
$\text{Ce}_2\text{Co}_{16}\text{Al}$	R-3m	8.402	8.164	[160]
$\text{Ce}_3\text{Co}_{14}\text{Al}_3$	R-3m	8.462	12.328	[160]
$\text{Y}_2\text{Co}_{17}$	P63/mmc	8.345	8.139	[161]
$\text{Y}_2\text{Co}_{17}\text{Al}_2$	P63/mmc	8.396	8.185	[162]
$\text{LaCo}_{13}$	Fm-3c	11.345	-	[163]
$\text{LaCo}_{10.3}\text{Al}_{2.7}$	Fm-3c	11.473	-	[163]
$\text{LaCo}_{10}\text{Al}_3$	I4/mcm	8.0851	11.6248	[163]
$\text{Nd}_2\text{Co}_{17}$	R-3m	8.416	12.221	[164]
$\text{Nd}_2\text{Co}_{13}\text{Al}_4$	R-3m	8.5488	12.4065	[165]

The EBSD method provided valuable insights into the phase composition of the RE-rich phases. However, since this technique should be used only supplementary, a more precise determination of the structure of the La, Nd, and Dy-rich phases would require in-depth analysis using advanced techniques such as SAED. Currently, it is not essential to determine the exact structure type (e.g., P63/mmc or P6/mmm) as the influence of RE-rich phase structure on the oxidation behavior of the alloys is not well understood. Similarly, the relationship between intermetallic RE-rich phases and oxidation is not extensively studied in the case of Ni-based superalloys, although some studies are available for reference [166, 167].

It is reasonable to observe the presence of phases with stoichiometry of  $\text{RE}_5\text{M}_{17}$  or  $\text{RE}_2\text{M}_{17}$  in alloys that contain very low amounts of RE, considering the existence of phases with the lowest RE content [154-157, 168]. However, in the Co-La system, the phase with the lowest La content has the stoichiometry  $\text{LaCo}_{13}$  [169]. These phases typically contain Al, Co, and

potentially very low amounts of W, leading to their description as  $REM_5$ ,  $RE_2M_{17}$ , or  $REM_{13}$  (where M = Co, Al, W). The formation of RE-M intermetallic phases is also observed in Ni-based alloys. In multicomponent Ni-based alloys, the  $Ni_5Y$  phase (P6/mmm) is often formed, which may contain other elements such as Co or Al [170, 171]. Certain studies reported the formation of  $Ni_{17}Y_2$  (P63/mmc) in addition to  $Ni_5Y$  in Ni-based alloys [172, 173]. The presence of the hexagonal crystal structure in  $Ni_5Y$  precipitates can result in brittleness, leading to premature failure due to crack initiation and propagation along grain boundaries. Consequently, this can reduce the ductility of the material. While several authors have noted the positive influence of Y on the mechanical properties of Ni-based superalloys, an excessive amount of this element can have detrimental effects [171, 173, 174]. Similar effects can be expected with the doping of other elements such as La, Nd, and Dy.

It can be assumed that the introduction of rare earth elements (La, Nd, Dy, Y) into Co-based alloys would result in the formation of intermetallic phases (cubic or hexagonal type of lattice) that are not coherent with the  $\gamma$ - $\gamma'$ . Literature data on Y-doped Ni-based alloys suggest that such phases may have a detrimental effect on the creep resistance of the alloys. Therefore, it is plausible that an excessive amount of RE-M phases could potentially decrease the mechanical properties of the new Co-based superalloys. Although different authors have reported improvements in mechanical properties through RE doping, this aspect requires careful attention and further investigation to optimize the dopant concentrations and alloy compositions for desired mechanical performance.

In the alloys based on the Co-Al-W system, RE (La, Nd, Dy, Y) may react with impurities to form stable non-metallic phases such as oxides and sulfides. On the other hand, RE that do not form non-metallic phases tend to form intermetallic phases with Co and other elements in the alloy. These intermetallic phases may have various stoichiometries, but they are often referred to as  $RE_2M_{17}$ ,  $REM_{13}$ , or  $REM_5$  phases. The microstructure evolution of RE-doped alloys, from the as-cast state to the as-aged state, is schematically presented in Figure 5.2.

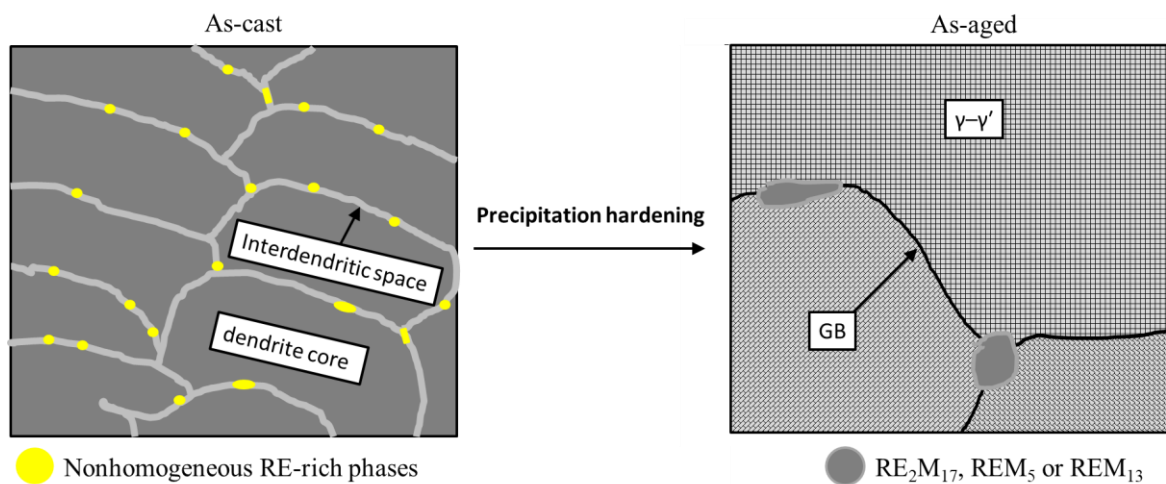


Figure 5.2: Schematic presenting the as-cast and as-aged microstructures of Co-Al-W alloys containing RE.

In addition to oxidation resistance and mechanical properties, the presence of Co-RE precipitates can also impact the thermal behavior of the alloys. The DSC experiments have shown endothermic effects, which could be associated with the incipient melting of the RE-rich phases. The connection between these endothermic effects and the presence of RE-rich phases has been further supported by the CALPHAD method. This suggests that the RE-rich phases can contribute to the overall thermal response of the alloy and may undergo melting or phase transformations at specific temperatures. Understanding these thermal effects is important for characterizing the behavior of RE-doped Co-based alloys under different thermal conditions.

Thermal effects similar to those described above were also observed in alloys containing Ce, as reported in a publication [150]. In this case, the alloys Co-9Al-9W-0.1Ce and Co-9Al-9W-0.5Ce (at%) exhibited the melting effect at approximately 1150 °C during heating. A similar effect, but with a higher intensity, was observed in the binary Co-Ce alloy, which exhibited two melting peaks. One peak corresponded to the melting of the binary  $Ce_2Co_{17}$  phase, while the second peak was related to the melting of fcc-Co. The reversible peak, corresponding to the crystallization of the  $Ce_2Co_{17}$  phase ( $Liquid + fcc-Co \rightarrow Ce_2Co_{17}$ ), occurred at 1202 °C, while the crystallization temperature of fcc-Co ( $Liquid \rightarrow fcc-Co$ ) was 1416 °C. These values were similar to the equilibrium temperatures for the corresponding binary Co-Ce alloys, which were approximately 1212 °C and 1410 °C, respectively [175]. These observations indicate that the presence of Ce can significantly influence the thermal behavior and phase transformations in Co-based alloys. Similar thermal effects have been observed in quaternary Co-Al-W-Ce alloys, indicating the melting and crystallization of  $\gamma$ -Co

and  $\text{Ce}_2\text{M}_{17}$  phases. These characteristic peaks observed in the DSC plots provide insight into the thermal behavior of Ce-containing alloys. Based on these findings, one can infer that analogous thermal effects may occur in other alloys containing elements such as La, Nd, Dy, and Y. These observations suggest that the presence of RE in Co-based alloys can influence their thermal properties and phase transformations.

The analyzed RE-doped alloys exhibit a characteristic feature wherein the incipient melting, which can be considered as solidus temperature, occurs at lower temperatures compared to the RE-Co phases in binary alloys with low RE content. Furthermore, this temperature is significantly lower than the solidus temperature of the alloy without RE. The decrease in incipient melting temperature of the Y-rich phase was found to increase substantially with increasing Al content, while only a slight increase was observed with an increase in W content. This observation suggests that not only the structure of the RE-M phases is sensitive to the alloy's chemical composition, but also their thermal behavior. The solidification sequence of the multicomponent RE-rich Co-based alloys may be analogous to that of binary alloys ( $\text{L} \rightarrow \gamma\text{-Co}_{\text{ss}} + \text{L} \rightarrow \gamma\text{-Co}_{\text{ss}} + \text{RE-M}$  phases), although further confirmation is required.

Detecting the incipient melting effect becomes challenging when the concentration of RE in an alloy is as low as 0.1 at%. However, in the analyzed alloys, the identification of this effect was made possible due to the high sensitivity of the multi-HTC DSC device. It is important to note that even when the concentration of RE-rich intermetallic phases is very low in the alloy, localized melting of phases located at grain boundaries can have a catastrophic impact on the alloy's behavior under high-temperature creep conditions. Therefore, special attention is required in the design of multicomponent Co-based alloys containing RE, considering the potential consequences of local melting on their overall performance.

## 5.2 High temperature oxidation behavior of alloys

The oxidation behavior of the analyzed alloys, both with and without RE, was a significant focus of the thesis. The oxidation studies were conducted under isothermal and cyclic conditions at temperatures of 700, 800, and 900 °C. At 700 °C, the differences in oxidation behavior among the alloys were relatively small. The oxide growth, measured by the mass gain per unit area, followed a parabolic law for all cases.

Although the base ORE alloy exhibited the highest oxidation rate, it is noteworthy that the value of  $k_p$  for the ORE alloy at 700 °C was only approximately 44% higher than that of the 0.1La alloy, which showed the lowest growth of oxide scale. It is important to mention that the  $k_p$  values listed in Table 4.7 were calculated using multiple samples (three samples for each oxidation time at certain temperature). Examination of the corresponding plots and error bars (Figure 4.8) indicates that the differences between the alloys were slight, which is consistent with the thickness measurements of the oxide scales obtained after 500 h of oxidation at 700 °C (Table 4.9).

At 800 °C, the alloys also displayed a parabolic oxide growth, except for the 0.1La and 0.1Nd alloys, which showed some deviation from parabolic behavior. This was reflected in the linear correlation coefficient (R), which was approximately 0.9 for the 0.1La alloy and 0.92 for the 0.1Nd alloy. In the initial 100 h of oxidation at 800 °C, the oxidation rate was comparable for all alloys. However, after 300 and 500 h of oxidation, the base alloy exhibited higher oxide scale growth compared to the RE-doped alloys. Similar observations were made for samples subjected to oxidation at 900 °C. The oxidation behavior followed a parabolic trend, and the base alloy displayed higher oxide scale growth compared to the RE-doped alloys after extended oxidation times.

The observed differences in oxidation rates between the ORE alloy and the RE-doped alloys become more pronounced at higher temperatures, such as 900 °C and 1000 °C. At 700 °C, the differences in oxidation rates are negligible, while at 800 °C, they are relatively small. This trend is reflected in the activation energy of oxidation, as shown in Figure 4.9 for the ORE and 0.1Nd alloys. A similar behavior was observed in Ni-15Al and Ni-15Al-2Si alloys [176], where the Si-containing alloy exhibited a lower activation energy compared to the Ni-15Al alloy. In the case of the Si-alloyed alloy, the presence of silicon promotes the formation of  $\text{Al}_2\text{O}_3$ , resulting in a lower oxidation rate at higher temperatures (800-1200 °C) compared to the Ni-15Al alloy. Similarly, the RE-doped alloys in this study show improved oxidation

resistance compared to the 0RE alloy at elevated temperatures, indicating that the presence of RE elements influences the oxidation behavior of the alloys.

The isothermal oxidation resistance of the RE-doped alloys, especially the 0.1La and 0.1Nd alloys, was indeed higher compared to the 0RE alloy. However, it was observed that none of the alloys exhibited a continuous protective layer that could effectively block further oxide scale growth. Instead, discontinuous layers of Al-rich oxides were observed at temperatures of 700 °C and 800 °C, while at 900 °C, discontinuous layers and coarse precipitate segments of Al oxides were observed.

At temperatures of 700 °C and 800 °C, the oxide scale formed on the 0RE alloy exhibited presence of OOL, IOL, and a very thin Al-rich oxide layer, occurring only locally at 700 °C. In addition, a  $\gamma'$ -depleted zone composed of  $\gamma$  and  $\text{Co}_3\text{W}$  was observed. At 900 °C, the oxide scale consisted of OOL, IOL, and  $\gamma'$ -free zone containing  $\gamma$ ,  $\text{Co}_3\text{W}$ , dispersed small  $\text{Al}_2\text{O}_3$  islands, and coarse precipitates of  $\text{Al}_2\text{O}_3$ . This oxide scale morphology is typical for Co-Al-W alloys [96]. When considering the oxide scale formation during isothermal oxidation of RE-doped alloys, there are similarities observed compared to the RE-free alloy. Except of RE-rich oxides, the main difference is connected with inner oxide layers rich in Al. The example micrographs presenting inner oxide layers (marked by white arrows) formed on the 0.1La alloys at 700, 800, and 900 °C are depicted in Figure 5.3. At 700 °C, a very thin and irregular layer rich in Al can be found on the surface of the alloys (Figure 5.3a). Below this layer, a  $\gamma'$ -depleted zone can be observed. This Al-rich layer occurred only locally in the 0RE alloy (Figure 4.16a). At 800 °C, the inner oxide layer formed on the alloys was similar to that observed in the 0RE alloy. However, in some areas, a thicker layer was locally observed (Figure 5.3b). The oxide scale formed on the RE-doped alloys, particularly the 0.1La and 0.1Nd alloys, exhibited  $\gamma'$ -free zone. Within this region, a discontinuous layer of Al-rich oxide (Figure 5.3c), presumably  $\text{Al}_2\text{O}_3$ , was observed, along with alumina discrete precipitates (a) and coarse segments (b). The thickness of the Al oxide layer was approximately 1  $\mu\text{m}$ .

The growth of  $\text{Al}_2\text{O}_3$  as a diffusion barrier parallel to the surface is known to have a significant impact on oxidation kinetics [95]. In the case of the RE-doped alloys, areas characterized by the growth of alumina in the IPR were observed. However, no formation of alumina layers was observed in the 0RE alloy, even locally (Figure 4.25).

The increase in the volume fraction of  $\text{Al}_2\text{O}_3$  segments in the IPR may be sensitive to the chemical composition, particularly the W content [95]. However, the amount of W does not vary considerably between the 0RE and RE-containing alloys. It can be considered that since the RE-rich phases are almost W-free, the relative content of W in the  $\gamma$ - $\gamma'$  phase could be

higher. However, considering the small amount of RE in the alloy, this effect seems to be slight in magnitude.

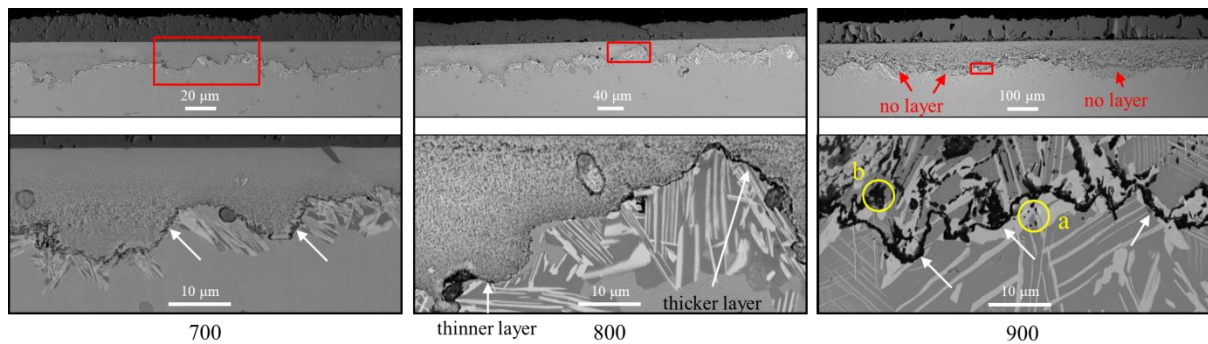


Figure 5.3: SEM micographs showing microstructure of oxide scales formed on the 0.1La alloy after 500 h of oxidation at 700, 800, and 900 °C.

Indeed, the higher fraction of Al oxides observed in the RE-doped alloys and formation of Al-rich layers could be one of the reasons explaining their improved isothermal oxidation resistance. It is important to note that the formation of more favorable inner oxide layers was primarily observed after long oxidation periods (300, 500 h), whereas for shorter durations (up to 100 h), the microstructures of the oxide scales were comparable (Figure 4.25). This is consistent with the comparable values of  $\Delta m/A$  for the base alloy and RE-doped alloys during the initial stages of oxidation at different temperatures. However, it is worth noting that even after long-term oxidation, the Al-rich layers grown were not sufficient to provide complete protection against oxidation. These layers were either discontinuous or not thick enough to effectively prevent further oxidation of the underlying material.

The occurrence of more developed IOLs in the RE-doped alloys is consistent with observed thickness of the  $\gamma'$ -free zones. The increased thickness of the  $\gamma'$ -depleted zones is connected to the oxidation of Al and the consequent depletion of the  $\gamma'$ - $\text{Co}_3(\text{Al}, \text{W})$  phase in this element. Similar microstructures and oxide layer thicknesses were observed in B-doped alloys, as reported in the literature [72]. For example, in B-doped alloys, such as the 0.12B alloy, the thickness of the  $\gamma/\text{Co}_3\text{W}$  zone can be equal to or even greater than the thickness of the IOL at 800 °C. The Al present in the former  $\gamma'$  phase is consumed to form a continuous inner  $\text{Al}_2\text{O}_3$  layer. Additionally, the formation of a discontinuous alumina layer at 900 °C, similar to that observed for the 0.1La alloy (Figure 5.3c), was noticed. It is worth noting that no continuous alumina layer was observed after oxidation at 800 °C for single-crystal B-doped alloys. This difference was attributed to decreased grain boundary diffusion in the single-crystal alloy, as concluded by the authors [78].

Both B and rare RE are known to exhibit a grain boundary pinning effect, which can facilitate grain boundary diffusion in heat-treated alloys compared to dopant-free alloys where grain boundary migration may occur. This phenomenon may, to some extent, contribute to the improved formation of alumina in RE-doped or B-doped Co-Al-W alloys. However, it should be noted that the differences in grain size among the alloys were not significant, as all alloys exhibited large grains, as can be seen in the macrographs of the 0RE, 0.1La, and 0.1Nd alloys after 1 h of oxidation at 900 °C (Figure 5.4).

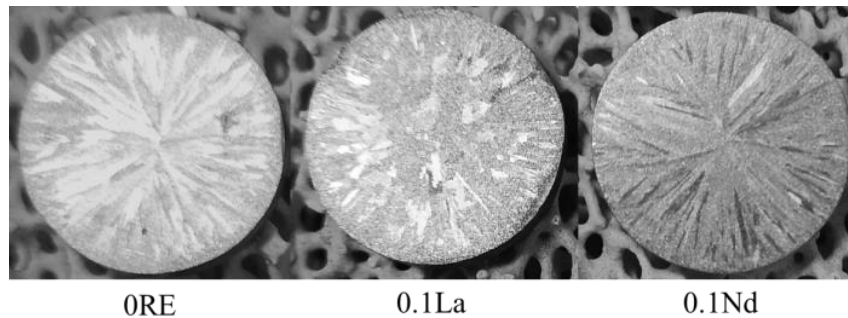


Figure 5.4: Macrographs showing the samples after 1 h oxidation at 900 °C.

Indeed, the pinning effect of rare earth elements (RE) could potentially influence the dislocation or subgrain boundary densities in the alloy. This, in turn, could facilitate a higher flux of protective scale-forming elements (e.g., Cr) from the substrate to the surface, enhancing the formation of a protective oxide scale. However, it is important to note that the specific role of RE on dislocation or subgrain boundary densities was not studied in the context of the mentioned thesis.

For the RE-doped alloys, the grain boundaries may be affected also in other way. GBs are sites for heterogeneous nucleation and act as short-circuit or rapid diffusion paths in the oxidation process [177]. The presence of RE, particularly when they are overdoped, can accelerate such phenomenon. The elements such as Y may form oxides considerably below the oxidation front. Frequently, in these regions where oxidation occurs, Al also undergoes oxidation, which can be attributed to the facilitated transport of oxidants through grain boundaries due to the presence of RE elements. This phenomenon was observed in Co-Al-W-Y alloys, where the Y-rich phases exhibited oxidation below the oxidation front [151]. The internally oxidized areas were rich in  $Y_2O_3$  and Al oxides. In undoped Co-Al-W alloys, Al oxides typically form only within the IOZ or just below it. However, the investigation described in reference [151] demonstrated that the presence of Y in Co-Al-W-based alloys promotes the internal oxidation of both Y and Al. Such phenomenon may contribute to the increased content of  $Al_2O_3$  precipitates in the internal oxidation zone. Furthermore, the

investigation conducted after 1 min of oxidation demonstrated a preferential oxidation of the Y-rich areas. Similar internal oxidation behavior was also observed in alloys containing La, Ce, Nd (as shown in Figure 5.5), and Dy. Figure 5.5 clearly illustrates an example of internal oxidation of Nd-rich phases situated at grain boundaries after 1 h of exposure at 900 °C. The phase located just below the oxidation front (c) was completely oxidized and contained oxides with a high concentration of Nd and Al. The oxidation of another phase, located approximately 50 μm below the oxidation front, can be noticed (a). Notably, such behavior was not observed in the case of the 0RE alloy.

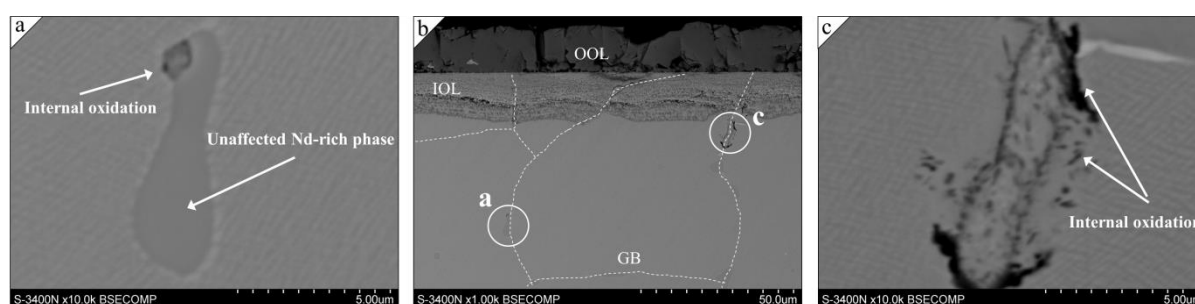


Figure 5.5: SEM micrographs of the oxide scale formed on the 0.1Nd alloy after 3 h of oxidation at 900 °C.

In addition to facilitating the inward transport of oxidation species, the oxidation of RE at grain boundaries may also contribute to the enhancement of oxide scale adhesion, leading to improved cyclic oxidation resistance when Co-Al-W alloy is doped with RE. This effect is particularly significant at 900 °C. At this temperature, cracks that occur during cooling typically manifest at the boundary between IOL and IPR or in the lower part of IOL (as depicted in Figure 4.25). In the case of the 0RE alloy, such oxide peeling can result in the spallation of almost the entire oxide scale in a single cooling cycle (Figure 5.6).

In this region, the presence of RE-rich oxides is frequently observed. The formation of oxide keys was clearly visible in Co-based superalloys containing 0.5 at% of Y, as well as in alloys containing 0.1 at% of RE (Figure 4.18c). In the case of Y-containing alloys (Figure 4.21), the oxide keys in the IPR consist of a mixture of  $Y_2O_3$  and possibly  $Al_2O_3$ . In the literature, several authors have reported the formation of yttrium aluminates [166, 170]. However, in the Y-doped Co-Al-W alloys investigated in this study, such phases were not observed. It cannot be excluded that such phases may form under different conditions or at higher temperatures.

While the formation of oxide keys can be seen as a factor that potentially enhances scale adherence, it is important to note that the keying mechanism is predominantly associated with alumina- and chromia-forming alloys. These alloys typically form uniform scales composed

of  $M_2O_3$  oxides, whereas the internal oxide layer (IOL) of Co-based alloys is multiphase in nature. Hence, it is reasonable to exercise caution when solely attributing the enhancement of the cyclic oxidation behavior of Co-Al-W alloys to this particular mechanism.



Figure 5.6: Macrographs showing the ORE sample after severe oxide spallation during long-term cyclic oxidation at 900 °C.

Another potential contributing factor to the observed improvement in cyclic oxidation behavior is the neutralization of sulfur, which is known to be a key factor in enhancing scale adhesion in alumina-forming alloys. However, assessing the influence of sulfur neutralization is challenging and was not considered in the conducted studies. Additionally, there is a lack of reports on the sulfur effect on the oxidation behavior of new Co-based superalloys. Another factor that could be considered, but requires further investigation, is the annihilation of vacancies by the presence of RE.

An additional possible explanation for the observed improvement is the lower oxidation rate of the RE-doped alloys. Thicker oxide scales are generally more prone to spallation [178]. However, it cannot be the sole reason for the improved behavior. The ORE alloy experienced significant oxide spallation at 900 °C, even during short-term cycles, indicating that oxide spallation occurred not only due to the high thickness of the oxide scale. Therefore, conducting cyclic oxidation tests using both long-term and short-term variants was a reasonable approach to examine the underlying factors.

However, it is important to note that cyclic oxidation resistance and isothermal oxidation resistance are interconnected and cannot be considered separately, as they both depend on the composition of the oxide scale to some extent. A detailed analysis of oxide scale evolution at 900 °C was conducted for the Co-Al-W alloy doped with 0.5 at% Y [151]. Similar studies on Co-Al-W-RE alloys, including the 0.1Y alloy and other RE-doped alloys containing 0.1 at% RE, showed comparable formation of oxide scale. A schematic representation of this process is presented in Figure 5.7.

The first stage (1) under consideration is the initial state of the alloy prior to oxidation, or the region below the internal oxidation front (IOF). This region, unaffected by oxidation, primarily consists of the  $\gamma$ - $\gamma'$  phase and the associated RE-rich phase. As the oxidation process initiates, the Y component in the RE-rich phase, and subsequently the Al component, undergoes internal oxidation (2). This stage also applies to regions that remain below the IOF during oxidation and, due to the presence of RE and internal oxidation, are susceptible to oxidation facilitated by the inward transport of oxidants through grain boundaries. The initiation of internal oxidation can be depicted by Figure 5.5a.

In the subsequent step (3), the oxidation process within the RE-rich phase is completed. Such regions can be observed in Figure 4.23 (0.5Y) or Figure 5.5c (0.1Nd). In the case of the 0.5Y alloy, the Y-rich phase undergoes partial oxidation and consists of the Al-depleted  $\gamma$  phase, Al-rich oxides (presumably  $\text{Al}_2\text{O}_3$ ), and  $\text{Y}_2\text{O}_3$ . It is expected that the phase composition in other RE-containing alloys would be similar, with the presence of other  $\text{M}_2\text{O}_3$  oxides ( $\text{M} = \text{La}, \text{Nd}, \text{Dy}$ ). Similar behavior has been reported for Ni-Al-Y alloys, where the reactive component undergoes a reaction with  $\text{O}^{2-}$ . At the interface of  $\text{Ni}_5\text{Y}/\gamma\text{-Ni}$ , oxides rich in aluminum (Al-rich oxides) are formed. Within the  $\text{Ni}_5\text{Y}$  phase, oxides with a high concentration of Al ( $\text{Al}_2\text{O}_3$ ) and Y ( $\text{Y}_2\text{O}_3$ ) are predominantly formed due to the strong affinity of oxygen to yttrium and aluminum [166, 167].

Above the IOF, the second oxidation front (SOF), which can be assigned to growth of the IOL (Figure 2.10) can be observed. The next stage (4) describes when the area or RE-rich oxide is entirely within the IOF, just below the SOF. Due to the internal oxidation of Al and its depletion, the original  $\gamma$ - $\gamma'$  microstructure underwent degradation, resulting in a combination of  $\gamma\text{-Co}_{\text{ss}}$  and needle-like  $\text{Co}_3\text{W}$  phases. Al underwent oxidation, forming islands of  $\text{Al}_2\text{O}_3$  within the former  $\gamma$ - $\gamma'$  region, and contributed to the presence of more  $\text{Al}_2\text{O}_3$  within the RE-rich area. The formation of  $\text{Co}_3\text{W}$  may be linked to the depletion of Al and Co during the oxidation process. Consequently, the discussed region consisted of  $\text{Co}_3\text{W}$  and a mixture of  $\text{Y}_2\text{O}_3$  and  $\text{Al}_2\text{O}_3$ . The corresponding area may be found in the case of alloy containing 0.5 at% Y (Figure 4.21). It is probable that similar phenomenon can occur in the case of alloys containing La, Nd (Figure 4.18f) and Dy. However, the detailed microstructural studies would be necessary to confirm it. The subsequent stages depict the microstructure of the relevant RE-rich phase in the model, which, following the advancement of the oxidation fronts, is partially located (5) and completely located (6) within the IOL. Such a stage (6) is visible in Figure 4.19. The model Y-rich region consists of  $\text{CoO}$ , Co-Al spinels, and  $\text{Y}_2\text{WO}_6$ . This phase composition implies that oxidation of  $\text{Co}_3\text{W}$  occurred, followed by solid-state

reactions that resulted in the formation of the region containing  $Y_2WO_6$  and the aforementioned oxides.  $Al_2O_3$  was not detected in the IOL, and instead, Al formed more complex oxides, such as spinels. Co-Al spinels were observed throughout the entire IOL, even in regions with a high concentration of Y. The presence of  $CoWO_4$  spinel was identified in the IOL, but not within the Y-rich area. The absence of  $CoWO_4$  in the Y-related oxide regions can be attributed to the presence of  $Y_2WO_6$ . The phase composition of the Y-rich area differed from both the IPR and IOL layers.

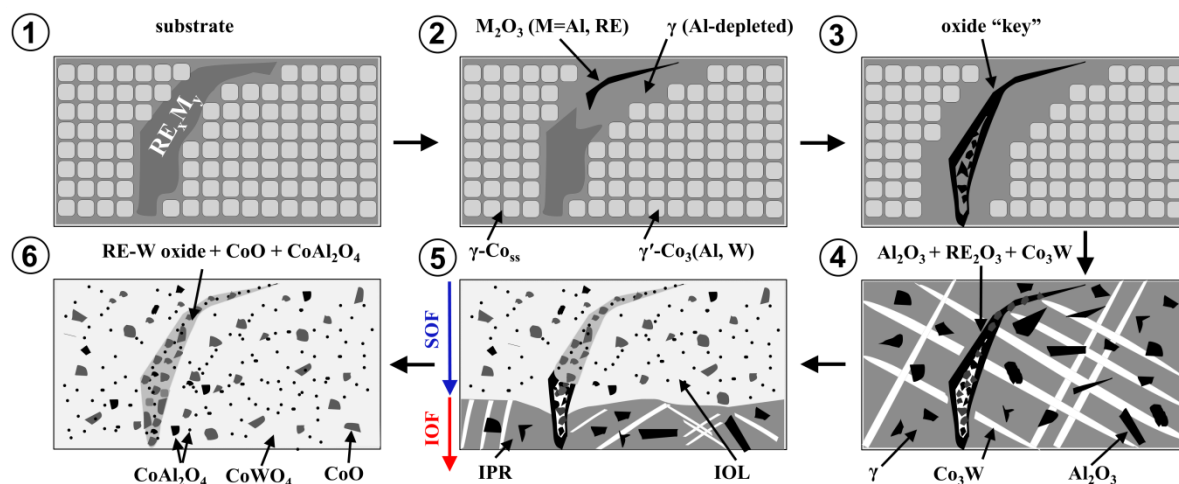


Figure 5.7: Schematic of the possible oxide scale formation in area of RE-rich phases.

The presence of  $RE_2WO_6$  oxide in the IOL was confirmed for the Y-containing alloy. However, for other alloys, the formation of RE-W tungstates is likely, as these elements (La, Nd, Dy) have the ability to form such phases, such as  $La_2WO_6$  [179]. An example of a possible La-W tungstate can be observed in Figure 4.18e. The BSE contrast in this zone is different from that of the surrounding IOL, which was also observed in the case of the Y-containing alloy [151]. However, this assumption is based on similarities with the detailed study of the Co-Al-W-Y alloy. To confirm the formation of RE-W tungstates other than  $Y_2WO_6$ , a detailed microstructural analysis is necessary. Stage (6) represents the final step in the oxide scale evolution in relation to Y-rich areas, as further oxidation does not lead to any significant changes. A similar oxidation behavior can be observed at 800 and 700 °C, where a very thin and discontinuous layer forms below the IOL instead of a relatively thick and discontinuous layer, as well as  $Al_2O_3$  segments and discrete precipitations. Figure 4.17f illustrates a RE-rich oxide area that bears resemblance to the formation of RE-W tungstates observed at 900 °C (represented as stage (6) in Figure 5.7). The areas depicted in Figure 4.17g and Figure 4.17i may correspond to stages (4) and (3) respectively, as shown in Figure 5.7. It

is possible that a similar evolution of the RE-rich phases to RE-rich oxides occurs at temperatures lower than 900 °C, although some differences may arise, particularly at 700 °C.

The impact of Re-W tungstates and  $Y_2O_3$  on the oxidation rate should be taken into account. There is almost no information on formation of  $Y_2WO_6$  and other RE-W tungstates within the oxide layers of the high temperature alloys. Wang et al. studied the effect of  $Y_2O_3$  addition on oxidation behavior of the binderless tungsten carbide [180].  $Y_2O_3$  and  $WO_3$  readily undergo oxidation, resulting in the formation of a highly stable  $Y_2WO_6$  phase with a larger ionic radius. This stable phase effectively hinders the inward diffusion of  $O^{2-}$  and the outward diffusion of  $W^{4+}$ . However, taking into consideration low content of RE-W tungstate within the IOL, the impact of these phases on the oxidation mechanism and kinetics seem to be low. The formation of tungstates with different stoichiometry is to consider. There are reports on  $Y_2W_3O_{12}$  tungstates formed during oxidation of W-Cr-Y alloys [181].

The positive effect of RE on the oxidation resistance of Co was reported even in the case of the binary alloy [142, 143, 182]. Co-Y does not naturally form a protective oxide layer. However, the addition of Y can enhance the oxidation resistance. Zeng et al. have reported that the activity of Co in the Y-rich phase ( $Y_2Co_{17}$ ) is significantly lower compared to  $\alpha$ -Co. Furthermore, internal oxidation of  $Y_2Co_{17}$  leads to the formation of  $Y_2O_3$ . The presence of yttrium oxide can hinder the diffusion of cobalt outwards. This is due to the prevalence of oxygen defects in  $Y_2O_3$ , resulting in faster oxygen diffusion compared to cation diffusion.

All alloys exhibited substantial internal oxidation of RE. Although oxide intrusions may be beneficial for oxide scale adherence, it is worth to note that deep internal oxidation is not beneficial in view of the long-term exposure of the material to operating conditions. Taking into consideration the obtained results, it can be assumed that RE cause the following structural effect in oxidation of the new Co-based superalloys:

- growth of thinner oxide scales compared to the RE-free alloy;
- enhancement of Al oxidation in the IOZ, resulting in formation of layers and coarse segments of Al-rich oxides, particularly at 900 °C;
- formation of thicker  $\gamma'$ -depleted zones as a result of the increased oxidation of Al;
- internal oxidation of RE and Al in the  $\gamma'$ -free layer and substantially below this zone;
- growth of oxide keys as a result of internal oxidation;
- formation of RE-W tungstates in the IOL.

### 5.3 The obtained results in view of the current state of the art

The conducted studies have provided valuable information that can contribute to the understanding of new Co-based superalloys. Many of the findings are novel and expand upon the current state of the art, although some observations may contradict previous reports. Until now, apart from two studies [150, 151], there has been limited information regarding the formation and characteristics of RE-M phases in new Co-based superalloys. Other authors have mainly reported an increase in RE content at grain boundaries [144-146, 148] or the formation of nano-oxides [147]. The presence of oxides in the as-aged alloys was not observed in any of the 0.1RE series alloys. However, it is highly likely that localized oxide formation, similar to the observed sulfides, may occur.

Based on the available literature, there is a lack of publications that specifically describe the oxidation behavior of Nd-doped Co-based superalloys. Additionally, there have been no reports addressing the formation of RE-W tungstates in the oxide scales of these superalloys. Furthermore, a noteworthy aspect that has emerged is the incipient melting effect observed in RE-doped alloys, which appears to be predictable but is also influenced by an alloy's composition. These findings underscore the need for further research to comprehensively understand and investigate these aspects in the context of Co-based superalloys.

The research conducted on the RE-effect on the oxidation behavior of the new Co-based alloys was highly comprehensive and extensive, as the entire thesis was dedicated to this specific topic. It is worth noting that there is a limited number of studies that provide detailed insights into the influence of RE on the oxidation behavior of alloys that do not belong to the alumina- or chromia-forming groups. Therefore, the obtained results are of particular interest. The oxide scales observed in the RE-doped alloys exhibited notable differences compared to those reported by Wang et al. [89]. Additionally, the oxidation kinetics, characterized by linear growth, differed between the base alloy and the RE-doped alloys studied in this research, where a parabolic growth behavior was observed. Furthermore, it is noteworthy that the Co-9Al-10W alloy exhibited a significant mass gain ( $\Delta m/A$ ) of approximately 150 mgcm<sup>-2</sup> after 400 h of oxidation at 900 °C, which is remarkably high under such conditions [89]. However, it is important to note that no such high increase was observed for the 0RE alloy, even after oxidation at 1000 °C. It appears that the authors of the study used only one sample for measuring the oxidation kinetics of the alloy at a specific temperature, even in cases where oxide spallation occurred. Such a measurement technique is considered unacceptable and may lead to the formation of atypical oxide scales that are not representative of the oxidation

behavior of the RE-doped alloys under appropriate conditions. Therefore, caution should be exercised when interpreting and comparing these results to ensure their relevance and validity in the context of the study.

The authors of the study suggested that the entire IOL is enriched with RE, similar to the findings of Klein et al. [76]. However, further detailed studies have shown that this enrichment effect does not occur in the case of Co-Al-W alloys doped with RE. Instead, RE elements do not migrate during oxidation but undergo internal oxidation. Moreover, within the IOL, they locally form RE-W tungstates, which are not observed in other parts of the layer. This indicates negligible diffusion of RE within the scale during oxidation. While  $Y_2O_3$  has an affinity to react with  $WO_3$ , the distribution of Y within the IOL may be even, but due to limited diffusion, it only forms  $Y_2WO_6$  locally. These observations suggest that the behavior of RE elements in Co-Al-W alloys differs from the suggested dynamic segregation mechanism described by Pint [128].

Zhong et al. reported enhanced formation of alumina beneath the IOL but did not observe any RE-containing oxides, even in alloys containing 0.2% Ce. They found that increasing RE content improved the isothermal oxidation resistance, which contradicts the findings of Wang et al. [89, 90], where the impact of RE on oxidation kinetics was negligible. Apart from measurement practices, the lack of RE impact on the oxidation resistance of the alloy may be attributed to the content of elements in the alloys. Manufacturing alloys with very small amounts of RE is challenging due to their high affinity for oxygen and the small volume of the added metal. During alloy production, it is easy for the RE element to be lost in the slag or oxidized, resulting in a lack of RE or reduced RE content in the final alloy. Therefore, it is essential to provide evidence of the existence of RE in the alloy to accurately assess its effect on the alloy's properties or its absence.

Although many aspects connected with doping of new alloys with RE are to still be explained, the author has high hopes that the results obtained from this extensive study will prove to be beneficial for future researchers in their pursuit of developing new Co-based alloys.

## 6. Summary and outlook

The objective of the dissertation was to investigate the effect of various RE on the high temperature oxidation behavior of new  $\gamma$ - $\gamma'$  Co-based superalloys derived from the Co-Al-W system. The investigations were extended to analysis of microstructure and thermal behavior of the Co-Al-W alloys. The motivation for conducting these studies was to enhance the current understanding and knowledge on this particular subject matter. The literature review revealed missing data to fulfill.

Therefore, the different RE-doped Co-Al-W-based alloys were developed. The experiments included characterization of microstructure after casting and after heat treatment, DSC analysis and investigation on isothermal and cyclic oxidation of the alloys at elevated temperatures. At the end, the oxide scale formed on different alloys and oxidation conditions were analyzed. The studies revealed impact of RE on the as-cast and as-aged microstructure, as well as on the resistance of new Co-based superalloys to isothermal and cyclic oxidation at 700-900 °C. DSC analysis revealed the potential harmful effects of RE on the maximum operating temperature of the alloys. The planned research goals were achieved.

It is clear that the addition of RE cannot sufficiently improve the oxidation resistance of Co-9Al-9W alloy, or even promote the formation of a continuous inner Al<sub>2</sub>O<sub>3</sub> layer that is formed during oxidation of B-doped Co-Al-W alloys [30]. Further studies on the doping of reactive elements should be performed on multicomponent alloys that can form a continuous Al<sub>2</sub>O<sub>3</sub> layer at temperatures up to 1000 °C. Such alloy compositions are now available, and for these alloys, the RE effect could be similar to that of multicomponent Ni-Al-based alloys. Due to the low solubility of RE in Co, it is probable that multicomponent alloys will also have RE-rich intermetallic phases at grain boundaries, which, besides affecting the oxidation properties, may also influence other characteristics of the alloys. Therefore, more studies are required to examine the modification of melting temperature due to RE-doping, especially the mechanical properties at elevated temperatures. Some studies have shown that elements such as Ce or Nd may enhance high temperature strength, whereas RE often cause a decrease in creep properties of superalloys, particularly when added in excessive amounts to an alloy.

## 7. Conclusions

The results contained in the dissertation may improve the understanding of the RE effect on microstructure and properties of the Co-Al-W alloys and provide some outlook for another attempts of introducing these elements to more complex Co-based alloys. Therefore, it is worth to draw the main conclusions resulting from the thesis:

- The addition of RE such as La, Nd, Dy, and Y may improve the isothermal oxidation resistance of Co-Al-W alloys, but the degree of improvement is limited due to the absence of protective alumina oxide scales at high temperatures. Presence of protective oxides layers was noticed only locally.
- The presence of RE in the alloys results in wider internal oxidation zones compared to the Co-9Al-9W alloy, without any considerable alteration in the oxidation mechanism. The oxidation mechanism is different than in alumina-forming alloys. The oxide scale of all the investigated alloys grows by both outward and inward transport, leading to the formation of an outer oxide layer and an internal oxidation zone containing a wide inner oxide layer.
- It is possible that the improved oxidation resistance observed at 900 °C can be connected with the formation of more developed internal precipitation regions in the RE-containing alloys compared to the reference alloy, followed by enhanced oxidation of Al.
- The RE-doped alloys exhibit improved resistance to high temperature cyclic oxidation. This feature may be caused by lower oxidation rate and formation of internally oxidized RE-oxides, which may improve scale adherence similarly to RE oxides in superalloys by -keying mechanism.
- During the oxidation of the RE-doped Co-Al-W alloys, no evidence of the reactive element effect described in the literature was observed. There was no segregation of the RE, but RE oxides were only formed as a result of internal oxidation or by a solid-state reaction in the oxide scale. The presence of RE-rich phases at grain boundaries in the RE-doped alloys may facilitate the transport of oxidants through the grain boundaries.
- The elements such as La, Nd, Dy, and Y can react with sulfur to form stable RE-sulfides, which can limit the activity of sulfur in the Co-Al-W alloys. This, in turn, can contribute to the oxidation properties of the alloys.
- The Co-Al-W alloys doped with RE form intermetallic phases that are not coherent with  $\gamma$ -Co and  $\gamma'$ -Co<sub>3</sub>(Al, W). These phases are predominantly situated at grain boundaries. The

tendencies to RE dissolution in  $\gamma$  or  $\gamma'$  phases were not observed. The dissolution of alloying elements such as Al, Ni, and possibly other in RE-Co phases

- The addition of RE can significantly lower the solidus temperature of the alloys, with the extent of this change being dependent on the alloy's overall composition. There is a lack of available information on the impact of RE doping in Co-based alloys in this regard, especially in  $\gamma$ - $\gamma'$  Co-based superalloys.
- Introducing RE to new Co-based superalloys has the potential to offer various advantages, but additional research is necessary due to the presented disadvantages or because there may be weaknesses that have not been yet identified.

## References

- [1] C. T. Sims: Superalloys: Genesis and Character. Superalloys II, edited by C.T. Sims, N. S. Stoloff, and W. C. Hagel (Ed.), John Wiley & Sons (1987), 3.
- [2] Mouritz: Introduction to Aerospace Materials, Cambridge, Woodhead Publishing (2012).
- [3] R.C. Reed: Superalloys - Fundamentals and Applications, Cambridge, Cambridge University Press (2006).
- [4] B. Geddes, H. Leon, X. Huang: Superalloys - Alloying and Performance, Materials Park, OH, ASM International (2010).
- [5] A. Kracke: Superalloys, the Most Successful Alloy System of Modern Times—Past, Present and Future, in: 7<sup>th</sup> International Symposium on Superalloy 718 and Derivatives, 2010, 13-50.
- [6] Y. M. Wang-Koh: Understanding the yield behaviour of L1<sub>2</sub>-ordered alloys, Materials Science and Technology, 33 (2017), 934-943.
- [7] D. Caillard: Yield-stress anomalies and high-temperature mechanical properties of intermetallics and disordered alloys, Materials Science and Engineering A, 319-321 (2001), 74-83.
- [8] D. Coutsouradis, A. Davin, M. Lamberigts: Cobalt-based superalloys for applications in gas turbines, Materials Science and Engineering, 88 (1987), 11-19.
- [9] D. L. Klarstrom: Wrought cobalt-base superalloys, Journal of Materials Engineering and Performance, 2 (1993), 523-530.
- [10] A. M. Beltran, C. T. Sims, N. T. Wagenheim: The High Temperature Properties of Mar-M Alloy 509, JOM, 21 (1969), 39-47.
- [11] E. Haynes: 1905. Metal Alloy. US patent, US873746A.
- [12] G. K. McKee, J. Watson-Farrar: Replacement of arthritic hips by the McKee-Farrar prosthesis, The Journal of Bone and Joint Surgery. British Volume, 48 (1966), 245-259.
- [13] J. R. Davis: ASM Specialty Handbook: Nickel, Cobalt, and Their Alloys, Materials Park, OH, ASM International (2000).

- [14] W. H. Jiang, H. R. Guan, Z. Q. Hu: Effects of heat treatment on microstructures and mechanical properties of a directionally solidified cobalt-base superalloy, *Materials Science and Engineering: A*, 271 (1999), 101-108.
- [15] S. K. Makineni, A. Sharma, P. Pandey, K. Chattopadhyay: An overview on Co-base alloys for high temperature applications. *Encyclopedia of Materials: Metals and Alloys*, F.G. Caballero (Ed.), Elsevier, 323-334.
- [16] J. Sato, T. Omori, K. Oikawa, I. Ohnuma, R. Kainuma, K. Ishida: Cobalt-base high-temperature alloys, *Science*, 312 (2006), 90-91.
- [17] S. K. Makineni, A. Samanta, T. Rojhirunsakool, T. Alam, B. Nithin, A. K. Singh, R. Banerjee, K. Chattopadhyay: A new class of high strength high temperature cobalt based  $\gamma$ - $\gamma'$  Co-Mo-Al alloys stabilized with Ta addition, *Acta Materialia*, 97 (2015), 29-40.
- [18] C. S. Lee: Precipitation-hardening Characteristics of Ternary Cobalt - Aluminum - X Alloys (Ph.D. thesis), The University of Arizona (1971).
- [19] T. Omori, Y. Sutou, K. Oikawa, R. Kainuma, K. Ishida: Shape memory and magnetic properties of Co-Al ferromagnetic shape memory alloys, *Materials Science and Engineering: A*, 438-440 (2006), 1045-1049.
- [20] R. W. Fountain, W. D. Forgeng: Phase relations and precipitation in Cobalt-Titanium alloys, *Transactions of the American Institute of Mining and Metallurgical Engineers*, 215 (1959), 998-1008.
- [21] M. Korchynsky, R. W. Fountain: Precipitation phenomena in cobalt-tantalum alloys, *Transactions of the Metallurgical Society of AIME*, 215 (1959), 1033-1043.
- [22] R. D. Dragsdorf, W. D. Foreing: The intermetallic phases in the cobalt-tantalum system, *Acta Crystallographica*, 15 (1962), 531-536.
- [23] J. Dutkiewicz, G. Kostorz: Structure of martensite in Co-W alloys, *Materials Science and Engineering: A*, 132 (1991), 267-272.
- [24] A. Suzuki, G. C. DeNolf, T. M. Pollock: Flow stress anomalies in  $\gamma/\gamma'$  two-phase Co-Al-W-base alloys, *Scripta Materialia*, 56 (2007), 385-388.
- [25] A. Suzuki, T. M. Pollock: High-temperature strength and deformation of  $\gamma/\gamma'$  two-phase Co-Al-W-base alloys, *Acta Materialia*, 56 (2008), 1288-1297.

- [26] A. Mottura, A. Janotti, T. M. Pollock: Alloying effects in the  $\gamma'$  phase of Co-based superalloys, in: *Superalloys 2012: 12<sup>th</sup> International Symposium on Superalloys*, 2012, 685-693.
- [27] C. Jiang: First-principles study of  $\text{Co}_3(\text{Al}, \text{W})$  alloys using special quasi-random structures, *Scripta Materialia*, 59 (2008), 1075–1078.
- [28] S. Kobayashi, Y. Tsukamoto, T. Takasugi, H. Chinen, T. Omori, K. Ishida, S. Zaefferer: Determination of phase equilibria in the Co-rich Co–Al–W ternary system with a diffusion-couple technique, *Intermetallics*, 17 (2009), 1085-1089.
- [29] E. A. Lass, M. E. Williams, C. E. Campbell, K.-W. Moon, U. R. Kattner:  $\gamma'$  Phase Stability and Phase Equilibrium in Ternary Co-Al-W at 900 °C, *Journal of Phase Equilibria and Diffusion*, 35 (2014), 711-723.
- [30] S. Kobayashi, Y. Tsukamoto, T. Takasugi: Phase equilibria in the Co-rich Co-Al-W-Ti quaternary system, *Intermetallics*, 19 (2011), 1908-1912.
- [31] S. Kobayashi, Y. Tsukamoto, T. Takasugi: The effects of alloying elements (Ta, Hf) on the thermodynamic stability of  $\gamma'$ - $\text{Co}_3(\text{Al}, \text{W})$  phase, *Intermetallics*, 31 (2012), 94-98.
- [32] H. Harada, H. Murakami: Design of Ni-Base Superalloys. *Computational Materials Design*, T. Saito (Ed.), Springer (1999), 39-67.
- [33] P. Caron: High  $\gamma'$  solvus new generation nickel-based superalloys for single crystal turbine blade applications, in: *Superalloys 2000 : proceedings of the 9<sup>th</sup> International Symposium on Superalloys*, 2000, 737–746.
- [34] H. Mughrabi: The importance of sign and magnitude of  $\gamma/\gamma'$  lattice misfit in superalloys- with special reference to the new  $\gamma'$ -hardened cobalt-base superalloys, *Acta Materialia*, 81 (2014), 21-29.
- [35] C. Wang, M. A. Ali, S. Gao, J. V. Goerler, I. Steinbach: Combined phase-field crystal plasticity simulation of P-and N-type rafting in Co-based superalloys, *Acta Materialia*, 175 (2019), 21-34.
- [36] T. M. Pollock, J. Dibbern, M. Tsunekane, J. Zhu, A. Suzuki: New Co-based  $\gamma$ – $\gamma'$  high-temperature alloys, *JOM*, 62 (2010), 58-63.

- [37] A. Bauer, S. Neumeier, F. Pyczak, M. Goken: Microstructure and creep strength of different  $\gamma/\gamma'$ -strengthened Co-base superalloy variants, *Scripta Materialia*, 63 (2010), 1197–1200.
- [38] Y. Chen, C. Wang, J. Ruan, T. Omori, R. Kainuma, K. Ishida, X. Liu: High-strength Co-Al-V-base superalloys strengthened by  $\gamma'$ -Co<sub>3</sub> (Al, V) with high solvus temperature, *Acta Materialia*, 170 (2019), 62-74.
- [39] C. Wang, X. Chen, Y. Chen, J. Yu, W. Cai, Z. Chen, X. Yu, Y. Li, Y. Yang, X. Liu: Accelerated design of high  $\gamma'$  solvus temperature and yield strength cobalt-based superalloy based on machine learning and phase diagram, *Frontiers in Materials*, 9 (2022), 1-9.
- [40] S. Neumeier, L. P. Freund, M. Göken: Novel wrought  $\gamma/\gamma'$  cobalt base superalloys with high strength and improved oxidation resistance, *Scripta Materialia*, 109 (2015), 104-107.
- [41] S. Tin, T. M. Pollock: Stabilization of thermosolutal convective instabilities in Ni-based single-crystal superalloys: carbide precipitation and Rayleigh numbers, *Metallurgical and Materials Transactions A*, 34 (2003), 67-82.
- [42] S. Tin, T. M. Pollock, W. Murphy: Stabilization of thermosolutal convective instabilities in Ni-based single-crystal superalloys: carbon additions and freckle formation, *Metallurgical and Materials Transactions A*, 32 (2001), 1743–1753.
- [43] Y. Zhao, Y. Zhang, Y. Zhang, Y. Luo, D. Tang, H. Liu, H. Fu: Deformation behavior and creep properties of Co-Al-W-based superalloys: A review, *Progress in Natural Science: Materials International*, 31 (2021), 641-648.
- [44] F. Xue, H. J. Zhou, Q. Feng: Improved high-temperature microstructural stability and creep property of novel Co-base single-crystal alloys containing Ta and Ti, *JOM*, 66 (2014), 2486-2494.
- [45] M. Knop, P. Mulvey, F. Ismail, A. Radecka, K. M. Rahman, T. C. Lindley, B. A. Shollock, M. C. Hardy, M. P. Moody, T. L. Martin, P. A. J. Bagot, D. Dye: A new polycrystalline Co-Ni superalloy, *JOM*, 66 (2014), 2495–2501.
- [46] A. Suzuki, H. Inui, T. M. Pollock: L1<sub>2</sub>-Strengthened Cobalt-Base Superalloys, *Annual Review of Materials Research*, 45 (2015), 345-368.

- [47] S. K. Makineni, M. P. Singh, K. Chattopadhyay: Low-density, high-temperature Co base superalloys, *Annual Review of Materials Research*, 51 (2021), 187-208.
- [48] A. Sato, Y. L. Chiu, R. C. Reed: Oxidation of nickel-based single-crystal superalloys for industrial gas turbine applications, *Acta Materialia*, 59 (2011), 225-240.
- [49] B. Gleeson: Thermodynamics and Theory of External and Internal Oxidation of Alloys. Shreir's corrosion, *Shreir's Corrosion*, R. A. Cottis, et al. (Ed.), Elsevier (2010), 180-194.
- [50] N. Birks, G. H. Meier, F. S. Pettit: Thermodynamic fundamentals. Introduction to the High-Temperature Oxidation of Metals, 2nd edition, N. Birks et al. (Ed.), Cambridge University Press (2012), 16–38.
- [51] H. J. T. Ellingham, Reducibility of oxides and sulphides in metallurgical processes, *Journal of the Society of Chemical Industry*, 63 (1944), 125-133.
- [52] The Ellingham diagram, teaching and learning packages of University of Cambridge, [https://www.doitpoms.ac.uk/tlplib/ellingham\\_diagrams/ellingham.php](https://www.doitpoms.ac.uk/tlplib/ellingham_diagrams/ellingham.php).
- [53] G. Tamman, Über Anlauffarben von Metallen: *Zeitschrift für anorganische und allgemeine Chemie*, 111 (1920), 78-89.
- [54] N. Pilling, R. J. Bedworth: The Oxidation of Metals at High Temperatures, *Journal of the Institute of Metals*, 29 (1923), 529-591.
- [55] S. Mrowec, A. Stokłosa: Calculations of parabolic rate constants for metal oxidation, *Oxidation of Metals*, 8 (1974), 379-391.
- [56] S. Mrowec, T. Werber: Gas Corrosion of Metals, Katowice, "Silesian" Publishing House (1975), in Polish.
- [57] L. B. Pfeil: The oxidation of iron and steel at high temperatures, *Journal of Iron and Steel Research International*, 119 (1929), 501-547.
- [58] S. Mrowec, T. Walec, T. Werber: Oxidation of cobalt at high temperatures, *Corrosion Science*, 6 (1966), 287-297.
- [59] D. G. Thomas: Interstitial zinc in zinc oxide, *Journal of Physics and Chemistry of Solids*, 3 (1957), 229-237.

- [60] J. A. Haefling, F. A. Schmidt, O. N. Carlson: Air oxidation of yttrium and some yttrium-base alloys, *Journal of the Less Common Metals*, 7 (1964), 433-440.
- [61] D. J. Young: *Oxidation of Pure Metals, High Temperature Oxidation and Corrosion of Metals (Second Edition)*, D. J. Young (Ed.), Elsevier (2016), 85-144.
- [62] K. Hauffe: The mechanism of oxidation of metals and alloys at high temperatures, *Progress in Metal Physics*, 4 (1953), 71-104.
- [63] S. Mrowec: On the mechanism of high temperature oxidation of metals and alloys. *Corrosion Science*, 7 (1967), 563-578.
- [64] F. H. Stott, G. C. Wood, M. G. Hobby: A Comparison of the Oxidation Behavior of Fe-Cr-Al, Ni-Cr-Al, and Co-Cr-Al Alloys, *Oxidation of Metals*, 3 (1971), 103-113.
- [65] Y. Niu, X. J. Zhang, Y. Wu, F. Gesmundo: The third-element effect in the oxidation of Ni-xCr-7Al (x= 0, 5, 10, 15 at.%) alloys in 1 atm O<sub>2</sub> at 900–1000°C, *Corrosion Science*, 48 (2006), 4020-4036.
- [66] C. S. Giggins, F. S. Pettit: Oxidation of Ni-Cr-Al alloys between 1000° and 1200°C, *Journal of The Electrochemical Society*, 118 (1971), 1782-1790.
- [67] B. A. Pint: High Temperature Corrosion of Alumina-forming Iron, Nickel and Cobalt-base Alloys. *Shreir's Corrosion*, R. A. Cottis, et al. (Ed.), Elsevier (2010), 606-645.
- [68] B. Chattopadhyay, G. C. Wood: The transient oxidation of Fe-Cr and Ni-Cr alloys, *Journal of The Electrochemical Society*, 117 (1970), 1163-1171.
- [69] N. Irving, J. Stringer, D. P. Whittle: The high-temperature oxidation resistance of Co-Al alloys, *Oxidation of Metals*, 9 (1975), 427-440.
- [70] Y. T. Xu, T. D. Xia, J. Q. Yan, W. J. Zhao: Effect of alloying elements on oxidation behavior of Co-Al-W alloys at high temperature, *The Chinese Journal of Nonferrous Metals*, 20 (2010), 2168-2177.
- [71] L. Klein, A. Bauer, S. Neumeier, M. Göken, S. Virtanen: High temperature oxidation of  $\gamma/\gamma'$ -strengthened Co-base superalloys, *Corrosion Science*, 53 (2011), 2027-2034.
- [72] L. Klein, Y. Shen, M. S. Killian, S. Virtanen: Effect of B and Cr on the high temperature oxidation behaviour of novel  $\gamma/\gamma'$ -strengthened Co-base superalloys, *Corrosion Science*, 53 (2011), 2713-2720.

- [73] Y. Xu, T. Xia, W. Zhao, X. Wang, J. Yan: Activation energy of oxidation of novel Co-Al-W superalloys at high temperatures, *Rare Metal Materials and Engineering*, 40 (2011), 701-704.
- [74] H.-Y. Yan, V. A. Vorontsov, J. Coakley, N. G. Jones, H. J. Stone, D. Dye: Quaternary Alloying Effects and the Prospects for a New Generation of Co-Base Superalloys, in: 12<sup>th</sup> International Symposium on Superalloys, 2012, 705-714.
- [75] L. Klein, M. S. Killian, S. Virtanen: The effect of nickel and silicon addition on some oxidation properties of novel Co-based high temperature alloys, *Corrosion Science*, 69 (2013), 43-49.
- [76] L. Klein, S. Virtanen: Corrosion properties of novel  $\gamma'$ -strengthened Co-base superalloys, *Corrosion Science*, 66 (2013), 233-241.
- [77] F. Fan, H. Sun, D. Zhao, J. B. Sha: Effect of Mo on the high temperature oxidation behavior of Co-Al-W based alloys, *Materials Science Forum*, 747 (2013), 754-759.
- [78] L. Klein, B. von Bartenwerffer, M. S. Killian, P. Schmuki, S. Virtanen: The effect of grain boundaries on high temperature oxidation of new  $\gamma'$ -strengthened Co-Al-W-B superalloys, *Corrosion Science*, 79 (2014), 29-33.
- [79] L. Klein, A. Zendegani, M. Palumbo, S. G. Fries, S. Virtanen: First approach for thermodynamic modelling of the high temperature oxidation behaviour of ternary  $\gamma'$ -strengthened Co-Al-W superalloys, *Corrosion Science*, 89 (2014), 1-5.
- [80] H.-Y. Yan, V. A. Vorontsov, D. Dye: Alloying effects in polycrystalline  $\gamma'$  strengthened Co-Al-W base alloys, *Intermetallics*, 48 (2014), 44-53.
- [81] H.-Y. Yan, V. A. Vorontsov, D. Dye: Effect of alloying on the oxidation behaviour of Co-Al-W superalloys, *Corrosion Science*, 83 (2014), 382-395.
- [82] M. Weiser, A. Reichmann, M. Albu, S. Virtanen: P. Poelt, In situ investigation of the oxidation of cobalt-base superalloys in the environmental scanning electron microscope, *Advanced Engineering Materials*, 17 (2015), 1158-1167.
- [83] T. Ito, S. Ikeda, K. Tanaka: Improvement in high temperature oxidation resistance of Co-Al-W based superalloys, *Materials Research Society Symposium Proceedings*, 1760 (2014), 222-227.

- [84] F. Zhong, F. Fan, S. Li, J. Sha: High-temperature oxidation behaviour of novel Co-Al-W-Ta-B-(Mo, Hf, Nb) alloys with a coherent  $\gamma/\gamma'$ -dominant microstructure, *Progress in Natural Science: Materials International*, 26 (2016), 600-612.
- [85] C. H. Zenk, S. Neumeier, N. M. Engl, S. G. Fries, O. Dolotko, M. Weiser, S. Virtanen, M. Goken: Intermediate Co/Ni-base model superalloys - Thermophysical properties, creep and oxidation, *Scripta Materialia*, 112 (2016), 83-86.
- [86] C. A. Stewart, R. K. Rhein, A. Suzuki, T. M. Pollock, C. G. Levi: Oxide scale formation in novel  $\gamma/\gamma'$  cobalt-based alloys, in: *Superalloys 2016: Proceedings of the 13<sup>th</sup> International Symposium on Superalloys*, 2016, 991-999.
- [87] C. A. Stewart, A. Suzuki, T. M. Pollock, C. G. Levi: Rapid assessment of oxidation behavior in Co-based  $\gamma/\gamma'$  alloys, *Oxidation of Metals*, 90 (2018), 485-498.
- [88] C. A. Stewart, A. Suzuki, R. K. Rhein, T. M. Pollock: C. G. Levi, Oxidation behavior across composition space relevant to Co-based  $\gamma/\gamma'$  alloys, *Materials Transactions A*, 50 (2019), 5445-5458.
- [89] Q. Wang, Q. Yao, J.-Z. Song, Y. Wang, Y.-H. Zhu, T. Lu, B.-J. Han: Effect of rare earth element on the oxidation behavior of novel  $\gamma/\gamma'$ -strengthened Co-9Al-10W alloys, *Journal of Materials Research*, 32 (2017), 2117-2126.
- [90] Q. Wang, Q. Yao, Y. Wang, Y.-H. Zhu, T. Lu: Research on the oxidation behavior of novel  $\gamma/\gamma'$ -strengthened Co-9Al-10W alloys combined with chromium and rare earth elements, *Journal of Materials Research*, 31 (2016), 3332-3344.
- [91] F. B. Ismail, V. A. Vorontsov, T. C. Lindley, M. C. Hardy, D. Dye, B. A. Shollock: Alloying effects on oxidation mechanisms in polycrystalline Co-Ni base superalloys, *Corrosion Science*, 116 (2017), 44-52.
- [92] A.-C. Yeh, S.-C. Wang, C.-F. Cheng, Y.-J. Chang, S.-C. Chang: Oxidation behaviour of Si-bearing Co-based alloys, *Oxidation of Metals*, 86 (2016), 99-112.
- [93] R. J. Chater, M. Weiser, S. Virtanen: Visualizing ion transport mechanisms through oxide scales grown on mixed nickel-and cobalt-base model alloys at 900 °C using FIB-SIMS techniques, *Journal of Vacuum Science and Technology B: Nanotechnology and Microelectronics*, 36 (2018), 03F116.

- [94] M. Weiser, R. J. Chater, B. A. Shollock, S. Virtanen: Transport mechanisms during the high-temperature oxidation of ternary  $\gamma/\gamma'$  Co-base model alloys, *NPJ Materials Degradation*, 3 (2019), 33.
- [95] M. Weiser, S. Virtanen: Influence of W content on the oxidation behaviour of ternary  $\gamma'$ -strengthened Co-based model alloys between 800 and 900 °C, *Oxidation of Metals*, 92 (2019), 541-560.
- [96] M. Weiser, Y. M. Eggeler, E. Spiecker, S. Virtanen: Early stages of scale formation during oxidation of  $\gamma/\gamma'$  strengthened single crystal ternary Co-base superalloy at 900 °C, *Corrosion Science*, 135 (2018), 78-86.
- [97] S. A. Forsik, A. O. P. Rosas, T. Wang, G. A. Colombo, N. Zhou, S. J. Kernion, M. E. Epler: High-temperature oxidation behavior of a novel Co-base superalloy, *Metallurgical and Materials Transactions A*, 49 (2018), 4058-4069.
- [98] D. Migas, G. Moskal, D. Niemiec: Surface condition of new  $\gamma-\gamma'$  Co-Al-Mo-Nb and Co-Al-W cobalt-based superalloys after oxidation at 800 °C, *Journal of Materials Engineering and Performance*, 27 (2018), 447-456.
- [99] M. Weiser, M. C. Galetz, H. E. Zschau, C. H. Zenk, S. Neumeier, M. Göken, S. Virtanen: Influence of Co to Ni ratio in  $\gamma'$ -strengthened model alloys on oxidation resistance and the efficacy of the halogen effect at 900°C, *Corrosion Science*, 156 (2019), 84-95.
- [100] B. Gao, L. Wang, Y. Liu, X. Song, S. Y. Yang, A. Chiba: High temperature oxidation behaviour of  $\gamma'$ -strengthened Co-based superalloys with different Ni addition, *Corrosion Science*, 157 (2019), 109-115.
- [101] I. Bantounas, B. Gwalani, T. Alam, R. Banerjee, D. Dye: Elemental partitioning, mechanical and oxidation behaviour of two high- $\gamma'$  W-free  $\gamma/\gamma'$  polycrystalline Co/Ni superalloys, *Scripta Materialia*, 163 (2019), 44-50.
- [102] S. M. Das, M. P. Singh, K. Chattopadhyay: Evolution of oxides and their microstructures at 800°C in a  $\gamma-\gamma'$  stabilised Co-Ni-Al-Mo-Ta superalloy, *Corrosion Science*, 155 (2019), 46-54.
- [103] D. Migas, G. Moskal, H. Myalska, T. Mikuszewski: The effect of alloying elements on oxide scale spallation of multicomponent Co-based superalloys, *Corrosion Science*, 192 (2021), 109787.

- [104] C. A. Stewart, S. P. Murray, A. Suzuki, T. M. Pollock, C. G. Levi: Accelerated discovery of oxidation resistant CoNi-base  $\gamma/\gamma'$  alloys with high  $L1_2$  solvus and low density, *Materials & Design*, 189 (2020), 108445.
- [105] S. M. Das, M. P. Singh, K. Chattopadhyay: Effect of Cr addition on the evolution of protective alumina scales and the oxidation properties of a Ta stabilized  $\gamma'$ -strengthened Co-Ni-Al-Mo-Ta-Ti alloy, *Corrosion Science*, 172 (2020), 108683.
- [106] W. Li, L. Li, S. Antonov, F. Lu, Q. Feng: Effects of Cr and Al/W ratio on the microstructural stability, oxidation property and  $\gamma'$  phase nano-hardness of multi-component Co-Ni-base superalloys, *Journal of Alloys and Compounds*, 826 (2020), 154182.
- [107] D. W. Chung, J. P. Toinin, E. A. Lass, D. N. Seidman, D. C. Dunand: Effects of Cr on the properties of multicomponent cobalt-based superalloys with ultra high  $\gamma'$  volume fraction, *Journal of Alloys and Compounds*, 832 (2020), 154790.
- [108] S. P. Hagen, M. Weiser, D. Kubacka, E. Spiecker, S. Virtanen: On the high-temperature oxidation behavior of a Ta-containing quaternary Co-Base model alloy system with  $\gamma/\gamma'$ -microstructure-influence of  $\gamma'$ -volume fraction, surface state, and heating condition on alumina growth, *Oxidation of Metals*, 94 (2020), 477-503.
- [109] Z. Liang, F. Pyczak, A. Stark, Z. Rao, S. Neumeier, M. Göken: Breaking the continuity of the  $Al_2O_3$  oxide scale by additions of Cr in Co-Al-W-based superalloys, *Corrosion Science*, 189 (2021), 109594.
- [110] Z. Liang, M. Göken, U. Lorenz, S. Neumeier, M. Oehring, F. Pyczak, A. Stark, L. Wang: Influence of small amounts of Si and Cr on the high temperature oxidation behavior of novel cobalt base superalloys, *Corrosion Science*, 184 (2021), 109388.
- [111] Z. Chen, N. L. Okamoto, K. Chikugo, H. Inui: On the possibility of simultaneously achieving sufficient oxidation resistance and creep property at high temperatures exceeding 1000 °C in Co-based superalloys, *Journal of Alloys and Compounds*, 858 (2021), 157724.
- [112] M. P. Singh, S. M. Das, O. P. Gosain, K. Chattopadhyay: On the role of Ti aiding the protective barrier layer formation for  $\gamma'(L1_2)$ -strengthened Co-30Ni-10Al-5Cr-2Ta-2/4Ti superalloys, *Corrosion Science*, 194 (2022), 109928.

- [113] S. C. H. Llewelyn, R. J. Chater, N. G. Jones, M. C. Hardy, H. J. Stone: The effect of systematic variation of Ni:Co ratio on the oxidation behaviour of  $\gamma$ - $\gamma'$  Ni-Co-Al-Ti-Cr alloys, *Corrosion Science*, 178 (2021), 109087.
- [114] L. Li, L. Wang, Z. Liang, J. He, J. Qiu, F. Pyczak, M. Song: Effects of Ni and Cr on the high-temperature oxidation behavior and mechanisms of Co- and CoNi-base superalloys, *Materials & Design*, 224 (2022), 111291.
- [115] S. P. Hagen, M. Weiser, B. Abu-Khousa, S. Virtanen: Influence of the Co/Ni ratio and dendritic segregations on the high-temperature oxidation resistance of multinary Co-rich superalloys at 850 °C and 1050 °C, *Metallurgical and Materials Transactions A*, 53 (2022), 1552-1571.
- [116] S. P. Hagen, K. Beck, D. Kubacka, H.-E. Zschau, M. C. Galetz, E. Spiecker, S. Virtanen: Protective alumina scale growth at 900 °C for a Ni- and Cr-free Co-base model alloy with  $\gamma/\gamma'$ -microstructure: synergistic effects by combining shot-peening and halogenation, *Oxidation of Metals*, 97 (2022), 209-226.
- [117] K. Qian, S. Qu, L. Shu, P. Xue, X. Li, B. Chen, K. Liu: Effect of Chromium Content on the Oxidation Behavior of a Ta Stabilized  $\gamma'$ -Strengthened Polycrystalline Co-30Ni-10Al-4W-4Ti-2Ta Alloy, *Materials*, 15 (2022), 5833.
- [118] L. Qin, D. Kubacka, E. Spiecker, R. Drautz, J. Rogal: Atomistic simulations of diffusion in  $\gamma'$ -strengthened Co-based superalloys and its connection to selective alumina formation in early-stage oxidation, *Physical Review Materials*, 7 (2023), 013403.
- [119] L. Li, L. Wang, Z. Liang, J. He, M. Song, Unveiling different oxide scales in a compositionally complex polycrystalline CoNi-base superalloy, *Journal of Alloys and Compounds*, 947 (2023), 169558.
- [120] Y. Li, F. Pyczak, J. Paul, Z. Yao: Oxidation behaviors of Co-Al-W-0.1B superalloys in a long-term isothermal exposure at 900 °C, *Journal of Materials Science & Technology*, 34 (2018), 2212-2217.
- [121] C. Ma, S. Yang, Y. Zhang, K. Wang, H. Fu: Effects of temperature and Ti addition on high-temperature oxidation behaviors of Co-Al-W based superalloys, *Anti-Corrosion Methods and Materials*, 67 (2020), 445-451.

- [122] D. Naumenko, B. A. Pint, W. J. Quadackers: Current thoughts on reactive element effects in alumina-forming systems: in memory of John Stringer, *Oxidation of Metals*, 86 (2016), 1-43.
- [123] W. T. Griffiths and L. B. Pfeil: Improvements in Heat Resistant Alloys. U.K. Patent no. 459848 (1937).
- [124] L. B. Pfeil: Improvements Relating to Heat Resisting Alloys Containing Chromium. U.K. Patent No. 574088 (1945).
- [125] B. A. Pint: Progress in Understanding the Reactive Element Effect Since the Whittle and Stringer Literature Review, in: *Proceedings of John Stringer Symposium on High Temperature Corrosion*, 2003, 9-19.
- [126] B. A. Pint: Limitations on the use of surface doping for improving high-temperature oxidation resistance, *MRS Bulletin*, 19 (1994), 26-30.
- [127] B. A. Pint, J. Leibowitz, J. H. DeVan: The effect of an oxide dispersion on the critical Al content in Fe-Al alloys, *Oxidation of Metals*, 51 (1999), 181-197.
- [128] B. A. Pint: Experimental observations in support of the dynamic-segregation theory to explain the reactive-element effect, *Oxidation of metals*, 45 (1996), 1-37.
- [129] J. L. Smialek: Invited review paper in commemoration of over 50 years of oxidation of metals: alumina scale adhesion mechanisms: a retrospective assessment, *Oxidation of Metals*, 97 (2022), 1-50.
- [130] F. A. Golightly, F. H. Stott, G. C. Wood: The influence of yttrium additions on the oxide-scale adhesion to an iron-chromium-aluminum alloy, *Oxidation of Metals*, 10 (1976), 163-187.
- [131] B. A. Pint: Optimization of reactive-element additions to improve oxidation performance of alumina-forming alloys, *Journal of the American Ceramic Society*, 86 (2003), 686-695.
- [132] I. M. Allam, D. P. Whittle, J. Stringer: The oxidation behavior of CoCrAl systems containing active element additions, *Oxidation of Metals*, 12 (1978), 35-66.
- [133] S. Mrowec, A. Gil, J. Jedliński: The effect of certain reactive elements on the oxidation behaviour of chromia- and aluminaforming alloys, *Materials and Corrosion*, 38 (1987), 563-574.

- [134] J. G. Smeggil, A. J. Shuskus: The oxidation behavior of CoCrAlY, CoCrAl and yttrium-implanted CoCrAl alloys compared and contrasted, *Surface and Coatings Technology*, 32 (1987), 57-68.
- [135] F. Wang, H. Lou, W. Wu: Cyclic oxidation resistance of CoCrAl alloys and their sputtered microcrystalline coatings with and without yttrium, *Vacuum*, 43 (1992), 749-752.
- [136] L. Zhang, S. Ukai, T. Hoshino, S. Hayashi, X. Qu:  $Y_2O_3$  evolution and dispersion refinement in Co-base ODS alloys, *Acta Materialia*, 57 (2009), 3671-3682.
- [137] J. Xiang, X. Xu, L. Bai, Y. Zheng, H. Zhang: Effects of yttrium on cyclic oxidation resistance of Co-10Cr-5Si alloy, *Advanced Materials Research*, 785-786 (2013), 914-917.
- [138] X. H. Zhang, C. Zhang, Y. D. Zhang, S. Salam, H. F. Wang, Z. G. Yang: Effect of yttrium and aluminum additions on isothermal oxidation behavior of Tribaloy T-700 alloys, *Corrosion Science*, 88 (2014), 405-415.
- [139] L. Bai, X. Xu, J. Xiang, Y. Zheng, J. Wang: Effects of Yttrium on Cyclic Oxidation Resistance of Co-10Cr-5Al Alloy at 700 °C, *Applied Mechanics and Materials*, 528 (2014), 844-847.
- [140] H. Yu, S. Ukai, S. Hayashi, N. H. Oono, Effect of Cr and  $Y_2O_3$  on the oxidation behavior of Co-based oxide dispersion strengthened superalloys at 900 °C, *Corrosion Science*, 127 (2017), 147-156.
- [141] H. Yu, S. Ukai, S. Hayashi, N. Oono, Effect of Al content on the high-temperature oxidation of Co-20Cr-(5, 10)Al oxide dispersion strengthened superalloys, *Corrosion Science*, 118 (2017), 49-59.
- [142] W. T. Wu, R. Y. Yan, Y. Niu, F. Gesmundo: The oxidation of a Co-15wt%Y alloy under low oxygen pressures at 600–800 °C, *Corrosion Science*, 39 (1997), 1831-1843.
- [143] C. L. Zeng, F. C. Rizzo, W. T. Wu, M. J. Monteiro: The oxidation of Co-Y binary alloys at 600–800 °C in air, *Corrosion Science*, 41 (1999), 1731-1742.
- [144] J.-Q. Ma, F. Zhong, S.-S. Li, J.-B. Sha: Microstructure and grain boundary morphology evolution of a novel Co-9Al-9W-2Ta-0.02B alloy doped with yttrium, *Rare Metals*, 36 (2017), 951-961.

- [145] Z. Tao, F. Zhong, Y. Yu, J. Sha: Improvement of tensile behaviours of a  $\gamma'$ -Co<sub>3</sub>(Al, W) strengthened polycrystalline Co-9Al-4.5W-4.5Mo-2Ta-0.02B alloy at room-and high-temperatures by doping Ce, *Progress in Natural Science: Materials International*, 29 (2019), 416-424.
- [146] F. Zhong, Z. L. Tao, J. B. Sha: Improvement of isothermal oxidation resistance of a  $\gamma'$ -strengthened Co-Al-W-Mo-Ta-B alloy at 800 °C via doping Ce, *Rare Metals*, 40 (2021), 2065-2075.
- [147] Y. Xu, T. Ma, X. Lv, H. Li, Y. Yang: Effect of rare earth Nd on the microstructure and compression behavior of Co-8.8Al-9.8 W alloy, *Journal of Materials Engineering and Performance*, 32 (2023), 3166–3174.
- [148] Q. Guan, F. Zhong, J. Sha: Effect of Ce addition on hot corrosion behaviours of a cast  $\gamma'$ -strengthened Co-Al-W-Mo-Ta-B alloy at 800 °C, *Progress in Natural Science: Materials International*, 32 (2022), 463-471.
- [149] D. Migas, T. Liptakova, G. Moskal: Effect of rare earth cerium addition on oxidation behavior of Co-Al-W alloys at 800°C, *Archives of Metallurgy and Materials*, 67 (2022), 203-208.
- [150] D. Migas, H. Myalska-Głowacka, B. Chmiela, T. Maciąg, T. Mikuszewski, G. Moskal, K. Matus, M. Godzierz: Microstructural characterization of cerium rich phases in new polycrystalline Co-Al-W-xCe superalloys, *Journal of Materials Research and Technology*, 20 (2022), 1665-1676.
- [151] D. Migas, B. Chmiela, H. Myalska-Głowacka, G. Moskal, K. Matus, R. Swadźba: The effect of yttrium on oxide scale growth on Co-Al-W-based superalloys, *Corrosion Science*, 208 (2022), 110674.
- [152] D. Migas, S. Roskosz, G. Moskal, T. Mikuszewski, P. Gradoń: Effect of cooling rate on microstructure, microporosity, and segregation behavior of Co-Al-W alloys prepared by vacuum induction melting, *JOM*, 74 (2022), 2951-2963.
- [153] T. Mikuszewski, A. Tomaszewska, G. Moskal, D. Migas, B. Witala: The Induction vacuum smelting of Co-Al-W superalloys - optimizing the feedstock based on the alloy's chemical composition, elemental segregation, and slag formation, *Journal of Mining and Metallurgy, Section B: Metallurgy*, 58 (2022), 179-189.

- [154] C. P. Wang, J. Wang, X. J. Liu, I. Ohnuma, R. Kainuma, K. Ishida: Thermodynamic assessment of the Co–La and Mo–La systems, *Journal of Alloys and Compounds*, 453 (2008), 174-179.
- [155] A. Hussain, M.-A. Van Ende, J. Kim, I.-H. Jung: Critical thermodynamic evaluation and optimization of the Co–Nd, Cu–Nd and Nd–Ni systems, *Calphad*, 41 (2013), 26-41.
- [156] C. Wu, L. Yao, Y. Chuang: Reinvestigation of the Dy-Co binary system, *International Journal of Materials Research*, 85 (1994), 104-108.
- [157] Z. Du, D. Lü: Thermodynamic modelling of the Co-Y system, *Journal of Alloys and Compounds*, 373 (2004), 171-178.
- [158] D. Migas, P. Gradoń, H. Myalska, B. Chmiela, T. Maciąg, T. Mikuszewski: Thermal analysis of intermetallic phases formed in Co-Al and Ni-Al based superalloys doped with Y, in: 6th Central and Eastern European Conference on Thermal Analysis and Calorimetry, 2011, 111.
- [159] X. Liu, Z. Du, C. Guo, C. Li: Thermodynamic assessment of the Co-Nd system, *Journal of Alloys and Compounds*, 439 (2007), 97-102.
- [160] B.-G. Shen, J.-Y. Wang, H.-W. Zhang, S.-Y. Zhang, Z.-H. Cheng, B. Liang, W.-S. Zhan, C. Lin: Magnetocrystalline anisotropy of  $\text{Ce}_2\text{Co}_{17-x}\text{Al}_x$  compounds with  $x=0-3$ , *Journal of Applied Physics*, 85 (1999), 4666–4668.
- [161] N. Vityk, W. Suski, R. Gladyshevskii, K. Wochowski, Crystal structure and magnetic properties of the  $\text{Y}_2\text{Co}_{17-x}\text{Ga}_x$  phases, *Journal of Alloys and Compounds*, 442 (2007), 341-344.
- [162] B.-G. Shen, Z.-H. Cheng, S.-Y. Zhang, J.-Y. Wang, B. Liang, H.-W. Zhang, W.-S. Zhan: Magnetic properties of  $\text{R}_2\text{Co}_{15}\text{Al}_2$  compounds with  $\text{R}=\text{Y, Ce, Pr, Nd, Sm, Gd, Tb, Dy, Ho, Er, and Tm}$ , *Journal of Applied Physics*, 85 (1999), 2787–2792.
- [163] Y. Guo, J. Liang, J. Liang, X. Zhang, Y. Zhao, W. Tang, G. Rao: Crystal Structure and Magnetic Properties of  $\text{LaCo}_{13-x}\text{Al}_x$  Compounds, *Physica Status Solidi (A)*, 159 (1997), 297-304.
- [164] B. D. Liu, Y. X. Li, W. X. Li, H. Y. Liu, G. H. Wu, F. M. Yang, F. R. de Boer: Structural and magnetic properties of  $\text{Nd}_2\text{Co}_{17-x}\text{V}_x$  compounds, *Physica B: Condensed Matter*, 319 (2002), 28-34.

- [165] C. H. de Groot, F. R. de Boer, K. H. J. Buschow, Z. Hu, W. B. Yelon: Magnetic properties of  $\text{Nd}_2\text{Co}_{17-x}\text{Al}_x$  compounds studied by magnetic measurements and neutron diffraction, *Journal of Alloys and Compounds*, 233 (1996), 188-191.
- [166] Y. Wu, Y. Li, Y. Xu, M. Kang, J. Wang, B. Sun: Unveiling the mechanism of yttrium-related microstructure inhibiting or promoting high-temperature oxidation based on Ni-Al-Y alloys, *Acta Materialia*, 211 (2021), 116879.
- [167] Y. Wu, Y. Li, Y. Xu, M. Kang, J. Wang, B. Sun: Unveiling the precipitation-induced high-temperature oxidation behavior in a Ni-Al-Y alloy, *Materials Letters*, 297 (2021), 129977.
- [168] Y. Jiang, X. Li, Y. Jiang, S. Huang, X. Shi, C. Mao, L. Zhang, L. Liu, F. Zheng: Experimental investigation of phase relations in Al-Co-Y ternary system, *Calphad*, 56 (2017), 1-9.
- [169] Y. Guo, J. Liang, W. Tang, Y. Zhao, G. Rao: Subsolidus phase relations of the ternary La-Co-Al system, *Journal of Alloys and Compounds*, 239 (1996), 83-87.
- [170] T. J. Nijdam, W. G. Sloof: Effect of reactive element oxide inclusions on the growth kinetics of protective oxide scales, *Acta Materialia*, 55 (2007), 5980-5987.
- [171] T. N. Palleda, S. Banoth, M. Tanaka, H. Murakami, K. Kakehi: The role of yttrium micro-alloying on microstructure evolution and high-temperature mechanical properties of additively manufactured Inconel 718, *Materials & Design*, 225 (2023), 111567.
- [172] X. L. Li, S. M. He, X. T. Zhou, Y. Zou, Z. J. Li, A. G. Li, X. H. Yu: Effects of rare earth yttrium on microstructure and properties of Ni-16Mo-7Cr-4Fe nickel-based superalloy, *Materials Characterization*, 95 (2014): 171-179.
- [173] X. Li, S. He, J. Liang, X. Zhou: High-temperature oxidation behavior and oxide scale structure of yttrium-modified Ni-16Mo-7Cr-4Fe superalloy at 1273 K, *Oxidation of Metals*, 92 (2019), 67-88.
- [174] P. J. Zhou, J. J. Yu, X. F. Sun, H. R. Guan, X. M. He, Z. Q. Hu: Influence of Y on stress rupture property of a Ni-based superalloy, *Materials Science and Engineering: A*, 551 (2012), 236-240.
- [175] X. Su, W. Zhang, Z. Du, A thermodynamic modelling of the Co-Ce system, *Journal of Alloys and Compounds*, 267 (1998), 121-127.

- [176] S. Ma, Q. Ding, X. Wei, Z. Zhang, H. Bei: The effects of alloying elements Cr, Al, and Si on oxidation behaviors of Ni-based superalloys, *Materials*, 15 (2022), 7352.
- [177] D. L. Douglass: A critique of internal oxidation in alloys during the post-wagner era, *Oxidation of Metals*, 44 (1995), 81–111.
- [178] G. Cao, Z. Li, J. Tang, X. Sun, Z. Liu: Oxidation kinetics and spallation Model of Oxide Scale during Cooling Process of Low Carbon Microalloyed Steel, *High Temperature Materials and Processes*, 36 (2017), 927-935.
- [179] M. Yoshimura: High temperature phase relation in the system  $\text{La}_2\text{O}_3\text{-WO}_3$ , *Materials Research Bulletin*, 11 (1976), 151-158.
- [180] W. Jinfang, Z. Dunwen, Z. Liu, T. Zhibiao, L. Xiao, W. Yinan, L. Weiwei, Z. Xiaoqiong: Effect of  $\text{Y}_2\text{O}_3$  Addition on High-Temperature Oxidation of Binderless Tungsten Carbide, *Frontiers in Materials*, 8 (2021), 645612.
- [181] A. Calvo, K. Schlueter, E. Tejado, G. Pintsuk, N. Ordás, I. Iturriza, R. Neu, J. Y. Pastor, C. García-Rosales: Self-passivating tungsten alloys of the system W-Cr-Y for high temperature applications, *International Journal of Refractory Metals and Hard Materials*, 73 (2018), 29-37.
- [182] Y. Niu, Y. S. Li, F. Gesmundo, F. Viani: The oxidation of a Co–15 wt% yttrium alloy in 1 atm  $\text{O}_2$  at 600–800°C, *Intermetallics*, 8 (2000), 293-298.